

2017

Development of Mechanistic Models and Numerical Methods for Corrosion Prediction in Oil Industry

Li, Qiang Jr

Li, Q. J. (2017). Development of Mechanistic Models and Numerical Methods for Corrosion Prediction in Oil Industry (Doctoral thesis, University of Calgary, Calgary, Canada). Retrieved from <https://prism.ucalgary.ca>. doi:10.11575/PRISM/25681

<http://hdl.handle.net/11023/3746>

Downloaded from PRISM Repository, University of Calgary

UNIVERSITY OF CALGARY

Development of Mechanistic Models and Numerical Methods for Corrosion Prediction in
Oil Industry

by

Qiang Li

A THESIS

SUBMITTED TO THE FACULTY OF GRADUATE STUDIES
IN PARTIAL FULFILMENT OF THE REQUIREMENTS FOR THE
DEGREE OF DOCTOR OF PHILOSOPHY

GRADUATE PROGRAM IN MECHANICAL AND MANUFACTURING
ENGINEERING

CALGARY, ALBERTA

APRIL, 2017

© Qiang Li 2017

Abstract

Corrosion is the primary mechanism resulting in facility failures in oil industry, where downhole tubulars, above-ground gathering pipelines and buried transmission pipelines constitute the important facilities. Corrosion modelling is advantageous over experimental studies, and has been essential for industrial corrosion management.

Internal corrosion of pipelines occurs in CO₂-containing single-phase water or oil-water emulsion flow due to dissolved CO₂ in water. Corrosion of X65 pipeline steel under various flow conditions is studied with a home-made flow loop. A semi-empirical model is developed based on computational fluid dynamic (CFD) simulations to predict the corrosion rate of the pipe steel in CO₂-saturated oil-water emulsion flow.

The high-temperature high-pressure conditions encountered in steam-assisted gravity drainage (SAGD)/CO₂ co-injection systems introduce major corrosion concerns to downhole tubulars. A semi-empirical model is developed to predict the tubular corrosion rate under the SAGD/CO₂ co-injection conditions. The corrosion rate is very small when a compact scale is formed.

The CO₂ storage is used worldwide to help reduce CO₂ emission. However, supercritical CO₂ conditions in sites can lead to severe corrosion to steel tubing. To predict corrosion rate of the steel tubing under CO₂ storage conditions, a mechanistic model, which includes a water chemistry sub-model and an electrochemical corrosion sub-model, is developed. The predicted solution pH and corrosion rates are well consistent with the experimental results.

External corrosion is the dominant threat to structural integrity of abandoned pipelines in soils. Studies of corrosion of X52 pipeline steel in a simulated Regina soil solution show that the iron oxidation and oxygen or water reduction are electrochemical anodic and cathodic reactions, respectively, depending on the dissolved oxygen level. Porous corrosion products reduce somewhat the corrosion rate. A mechanistic model enabling prediction of the long-term corrosion rate is developed. Corrosion kinetic parameters used in the model are obtained by fitting the experimentally measured polarization curves with a computer program. The model is validated by comparing the calculated results with experimental data.

Acknowledgements

I would like to express my sincere gratitude to my supervisor, Dr. Frank Cheng for his constant guidance, encouragement, help and support throughout my whole Ph. D. program. His deep love and perception of science, his persistent endeavour for pursuing the truth, and his consistent efforts at achieving perfection have always inspired and helped me carry out this research project.

Thanks are also given to the members in my group, Drs. Luyao Xu, Huibin Xue, Tao Liu, Shiqiang Chen and Da Kuang, and those whose names cannot all be listed here, for their helps and valuable discussions in this work.

The generous financial supports from Natural Science and Engineering Research Council of Canada (NSERC) are highly appreciated, without which this work will not be possible.

Dedication

For

my parents and other family relatives,

and for others who have taught, guided and supported me over the past years.

Table of Contents

Abstract	ii
Acknowledgements	iv
Dedication	v
Table of Contents	vi
List of Tables	x
List of Figures and Illustrations	xii
List of Symbols, Abbreviations and Nomenclature	xvii
CHAPTER ONE: INTRODUCTION	1
1.1 Research background	1
1.2 Objectives	4
1.3 Contents of the thesis	5
CHAPTER TWO: LITERATURE REVIEW	7
2.1 Corrosion as a primary mechanism resulting in facility failures in oil industry	7
2.2 CO ₂ corrosion of above-ground pipelines and downhole tubulars	10
2.2.1 CO ₂ corrosion mechanisms	10
2.2.2 Effect of fluid flow	13
2.2.3 Effects of pressure and temperature	15
2.3 Corrosion of abandoned pipelines in soils	17
2.3.1 Corrosion mechanism	17
2.3.2 Parametric effects	19
2.4 Corrosion prediction models	20
2.4.1 Modelling as an effective methodology for corrosion management	20
2.4.2 Modelling of CO ₂ corrosion of pipelines in fluid flow	22
2.4.3 Modelling of CO ₂ corrosion in CO ₂ storage and high-temperature high- pressure conditions	28
2.4.4 Modelling of steel corrosion in soils	29
2.5 Summary	32
CHAPTER THREE: NON-UNIFORM CORROSION OF STEEL PIPE IN CO ₂ - CONTAINING FLUID FLOW	33
3.1 Introduction	33
3.2 Experimental	34
3.3 Results	38
3.4 Discussion	44
3.5 Summary	46
CHAPTER FOUR: CORROSION OF PIPELINES IN CO ₂ -SATURATED OIL- WATER EMULSION FLOW	48
4.1 Introduction	48
4.2 Methodology	49
4.2.1 Electrode and solution	49
4.2.2 Flow loop system	50

4.2.3 Experimental setup and electrochemical measurements	51
4.3 CFD simulation and model development	51
4.3.1 CFD simulation settings	51
4.3.2 Corrosion model description	53
4.4 Results.....	54
4.4.1 Polarization curve measurements	54
4.4.2 EIS measurements	58
4.4.3 CFD simulation	62
4.5 Discussion.....	63
4.5.1 CO ₂ corrosion of pipelines in oil-free fluid flow.....	63
4.5.2 Corrosion of steel pipe in oil-water emulsions.....	65
4.5.3 Corrosion prediction model and modelling validation.....	68
4.6 Summary.....	70
CHAPTER FIVE: MODELLING AND PREDICTION OF CORROSION OF STEEL TUBULARS IN SAGD/CO ₂ CO-INJECTION AND PRODUCTION SYSTEMS.....	71
5.1 Introduction.....	71
5.2 Solubility of CO ₂ in water	72
5.3 Determination of solution pH	79
5.4 CO ₂ corrosion of steel tubular in water condensate in SAGD/CO ₂ injection system	83
5.5 CO ₂ corrosion of steel tubulars in oil-water emulsion in SAGD/CO ₂ production system	85
5.6 Corrosion of steel tubulars in oil-water-sand multi-phased fluid	86
5.7 Quantitative prediction of corrosion rate of steel tubulars in SAGD/CO ₂ co- injection and production systems.....	87
5.7.1 Corrosion rate of the injection tubular.....	87
5.8 Corrosion rate of the production tubular.....	92
5.8.1 Corrosion rate of the steel in oil-water emulsions.....	92
5.8.2 Corrosion rate of the production tubular in oil-water-sand fluid	98
5.9 Summary.....	99
CHAPTER SIX: MODELLING OF CORROSION OF STEEL TUBING IN CO ₂ STORAGE	101
6.1 Introduction.....	101
6.2 Overview of the model	103
6.3 Water chemistry sub-model.....	104
6.3.1 Chemical reactions and reaction equilibrium constants	104
6.3.2 Solubility of CO ₂ in H ₂ O.....	105
6.3.3 Fugacity coefficient	106
6.3.4 Activity coefficients	107
6.4 Electrochemical model	113
6.4.1 Electrochemical reactions.....	113
6.4.2 Mass transfer model	116

6.4.3 Formation of corrosion scale	118
6.5 Modelling solutions	120
6.5.1 Initial and boundary conditions	120
6.5.2 Numerical methods.....	121
6.6 Water chemistry sub-modelling results and validation.....	122
6.7 Electrochemical sub-modelling results and validation	125
6.7.1 Modelling and validation of corrosion rate of steels	125
6.7.2 Effect of the solution layer thickness on corrosion of the steel.....	126
6.7.3 Effect of temperature on corrosion of the steel	128
6.7.4 Effect of CO ₂ partial pressure on corrosion of the steel	129
6.7.5 Time dependence of corrosion rate	131
6.7.6 Time dependence of porosity of the corrosion scale	132
6.7.7 Distributions of the species concentration in the solution.....	133
6.8 Limitations of the model.....	135
6.9 Summary.....	135
CHAPTER SEVEN: MECHANISM OF CORROSION OF X52 PIPELINE STEEL IN A SIMULATED SOIL SOLUTION	137
7.1 Introduction.....	137
7.2 Experimental.....	138
7.2.1 Material, specimen and solution.....	138
7.2.2 Electrochemical measurements	140
7.2.3 Surface morphology observation and corrosion product composition characterization.....	140
7.3 Results.....	141
7.3.1 Potentiodynamic polarization curve measurements	141
7.3.2 Open circuit potential and linear polarization resistance measurements.....	146
7.3.3 SEM analysis	148
7.3.4 Optical microscope observation	150
7.3.5 XRD patterns	151
7.4 Discussions	152
7.4.1 Corrosion of X52 steel in the simulated soil solution	152
7.4.2 Effect of dissolved oxygen concentration on the corrosion process	153
7.4.3 Effect of solution pH	154
7.4.4 Effect of Cl ⁻ concentration.....	155
7.4.5 Effect of immersion time.....	156
7.5 Summary.....	157
CHAPTER EIGHT: MODELLING OF CORROSION OF PIPELINES IN SOIL SOLUTION.....	159
8.1 Introduction.....	159
8.2 Determination of kinetic parameters.....	160
8.2.1 A brief review of corrosion kinetic parameters used in previous modelling work	160

8.2.2 Determination of the corrosion kinetic parameters by polarization curve measurements.....	161
8.3 Model development	170
8.3.1 Overview of the model	170
8.3.2 Electrochemical reactions.....	171
8.3.3 Controlling equations	173
8.3.4 Formation of corrosion products	173
8.3.5 Initial and boundary conditions	175
8.3.6 Methods for solving the numerical equations	176
8.4 Computational results and modelling validation	176
8.4.1 Modelling and validation of corrosion rate of the steel.....	176
8.4.2 Time dependence of the porosity of corrosion products	178
8.4.3 Distributions of the concentration of corrosive species in the solution.....	180
8.4.4 Effect of dissolved oxygen concentration on corrosion rate of the steel.....	181
8.4.5 Long-term corrosion rate prediction.....	182
8.5 Summary	184
CHAPTER NINE: CONCLUSIONS AND RECOMMENDATIONS	185
9.1 Conclusions.....	185
9.2 Recommendations.....	188
REFERENCES	190
APPENDIX A: EQUILIBRIUM CONSTANTS FOR CHEMICAL REACTIONS.....	202
APPENDIX B: PHYSICAL PROPERTIES OF WATER	204
APPENDIX C: OXYGEN SOLUBILITY IN ELECTROLYTE SOLUTIONS	207

List of Tables

Table 4.1 Electrochemical parameters fitted from the measured impedance data.	64
Table 4.2 Pressure drop gradient determined by CFD modelling for various flow conditions.....	68
Table 5.1 The operating conditions of the SAGD/CO ₂ co-injection tubular.....	87
Table 5.2 The calculated parameters for calculation of the corrosion rate and the corrosion rates of the steel tubular in SAGD/CO ₂ co-injection system.....	92
Table 5.3 Operating conditions of the production tubular in SAGD/CO ₂ co-injection systems.....	93
Table 5.4 Chemical composition of the SAGD-produce water [115].	93
Table 6.1 List of β and C Pitzer parameters.....	109
Table 6.2 The λ term for neutral species relevant to this model.	109
Table 6.3 The ψ term for three-ion interaction relevant to this model.....	110
Table 6.4 The θ_{ij} term for same-charge ion interaction relevant to this model.	113
Table 6.5 Electrochemical parameters of anodic and cathodic reactions included in the model [29, 97, 144, 145].	115
Table 6.6 Molecular diffusion coefficient of species included in the model (298.15 K).	117
Table 7.1 Chemical composition of the simulated Regina soil solution.....	140
Table 7.2 The R_p values of X52 steel in the soil solutions containing various Cl ⁻ concentrations immediately after the OCP is stable and after 30 days of testing in the solution.....	148
Table 8.1 A summary of corrosion kinetic parameters used in corrosion modelling in open publications.	161
Table 8.2 Corrosion kinetic parameters determined from the polarization curve fitting.	169
Table B1 Parameters for Eqs. (B-2) ~ (B-5).....	204
Table B2 Coefficients and exponents of Eq. (B-7) in its dimensionless form	205

Table B3 Values of constants for the dielectric constant of water	206
Table C1 Values of coefficients in Eq. (C-4) for multiple chemicals	208

List of Figures and Illustrations

Figure 2.1 Components of a corrosion cell [14].	8
Figure 2.2 A schematic diagram of the soil environment experienced by the buried pipeline [11].	10
Figure 3.1 Schematic diagram of the electrode assembly.	34
Figure 3.2 Schematic diagram of the experimental set-up of the flow loop system.	36
Figure 3.3 The 3-dimensional structure of the flow field model of the testing unit for CFD simulation.	37
Figure 3.4 Open-circuit potentials measured on the top and bottom electrodes as a function of time.	38
Figure 3.5 Galvanic current (curves) and potential difference (★) measured between the top and the bottom electrodes installed at the testing unit as a function of time.	39
Figure 3.6 EIS measured on the bottom (a) and the top (b) electrodes as a function of time.	41
Figure 3.7 SEM images of the morphology of the electrode surface at different location and testing time: (a) Top – day1, (b) Bottom – day 1, (c) Top –day 2, (d) Bottom – day 2, (e) Top –day 3, (f) Bottom – day 3.	42
Figure 3.8 Contour of flow velocity of the vertical plane of testing cell at a flow velocity 1 m/s.	43
Figure 3.9 Contour of flow velocity of the transverse plane of the testing unit at a flow velocity 1 m/s.	43
Figure 4.1 Schematic diagram of the home-made flow loop system.	50
Figure 4.2 A portion of 3-dimensional meshed structure of the fluid flow in the electrochemical testing unit.	52
Figure 4.3 Potentiodynamic polarization curves of X65 steel in CO ₂ -saturated oil-free solution (a) and oil-water emulsion (b), respectively, at 45 °C at various fluid flow rates.	55

Figure 4.4 Polarization curves of X65 steel in CO ₂ -saturated oil-free base solution and base oil-water emulsion, respectively, at flow velocity of 1 m/s and various temperatures.....	57
Figure 4.5 Polarization curves of X65 steel in CO ₂ -saturated solutions at 45 °C and flow velocity of 1 m/s, but with various oil contents.....	58
Figure 4.6 Nyquist diagrams of X65 steel in CO ₂ -saturated oil-free solution (a) and oil-water emulsion (b), respectively, at 45 °C at various fluid flow rates.....	59
Figure 4.7 Nyquist diagrams of X65 steel in CO ₂ -saturated oil-free solution (a) and oil-water emulsion (b), respectively, at flow velocity of 1 m/s and various temperatures.....	61
Figure 4.8 Nyquist diagrams of X65 steel in CO ₂ -saturated solutions at 45 °C and flow velocity of 1 m/s but with various oil contents.....	61
Figure 4.9 Electrochemical equivalent circuit for impedance data fitting, where R_s is the solution resistance, CPE is the constant phase element, R_p is the charge transfer resistance, R_L is the inductive resistance, and L is the inductance.	62
Figure 4.10 CFD simulated distribution of oil in oil-water emulsion with various oil contents at flow velocity of 1 m/s and 45 °C.	63
Figure 4.11 Corrosion rates of the steel in oil-free and 10% oil-water emulsion as a function of flow velocity (a) and temperature (b), as well as the dependence of corrosion rate on the oil content (c) in oil-water emulsions.	67
Figure 4.12 Comparison of the modelled corrosion rate with that obtained from the experimental testing.....	69
Figure 5.1 The user-interface of the computational code for determination of the solution pH.....	83
Figure 5.2 Solution pH and scaling factor calculated at various CO ₂ partial pressures (Operating pressure 500 kPa, and flow flux 20 m ³ /h).....	95
Figure 5.3 Solution pH and scaling factor calculated at various CO ₂ partial pressures (Operating pressure 2,000 kPa, and flow flux 20 m ³ /h).....	95
Figure 5.4 Maximum and minimum corrosion rate at various CO ₂ partial pressures (Operating pressure 500 kPa and flow flux 20 m ³ /h).....	97
Figure 5.5 Maximum and minimum corrosion rate at various CO ₂ partial pressures (Operating pressure 2,000 kPa and flow flux 20 m ³ /h).....	97
Figure 6.1 Schematic diagram of the physical model in the mechanistic modelling.	104

Figure 6.2. Solution pH calculated from the developed model as a comparison with published data Crolet and Bonis [149], Meysami et al. [150] at 42 °C and various CO ₂ partial pressures.....	122
Figure 6.3 Solution pH obtained from the developed model as a function of NaCl concentration at 25 °C under 1 bar CO ₂	123
Figure 6.4 Modelling pH results are compared with the data from Duan and Li [122] over a wide CO ₂ pressure range at 77 °C.....	124
Figure 6.5 Comparisons of the predicted corrosion rates by the developed model with data from the experimental testing and published literature (Cui et al. [153], Zhang et al. [42], Choi and Nesic [125], Choi et al. [154], Hassani et al. [155] and Hua et al. [156]) under supercritical CO ₂ conditions.....	126
Figure 6.6 Dependence of corrosion rate on the solution layer thickness at 80 °C and 10 bar and 95 bar CO ₂ partial pressures, respectively.	127
Figure 6.7 Calculated solution pH and corrosion rate as a function of temperature in simulated oilfield produced water (CaCl ₂ 15 g/L, NaHCO ₃ 1.1 g/L) at 82.74 bar of CO ₂	128
Figure 6.8 Dependence of corrosion rate of the steel on CO ₂ partial pressure in 25% NaCl solution, as well as comparison with the published data under this condition (Choi et al. [154]).....	130
Figure 6.9 Time dependence of corrosion rate of steels in brine water at 80 °C and 10 bar and 95 bar CO ₂ partial pressures.....	131
Figure 6.10 Time dependence of the scale porosity under the same condition as that of Figure 6.9.....	132
Figure 6.11 Distributions of the concentration of various species in the solution at 80 °C and a) 10 bar, b) 95 bar CO ₂ partial pressure.....	134
Figure 7.1 Optical view of the microstructure of X52 steel.	139
Figure 7.2 Potentiodynamic polarization curves of X52 steel immediately after the OCP becomes stable and after 30 days of immersion in the base soil solution.....	142
Figure 7.3 Potentiodynamic polarization curves of X52 steel in the soil solution with different DO concentrations.....	143
Figure 7.4 Potentiodynamic polarization curves of X52 steel in soil solution with different solution pH values.....	144

Figure 7.5 Potentiodynamic polarization curves of X52 steel in the soil solutions containing various Cl ⁻ concentrations (a) Immediately after the OCP is stable, (b) After 30 days of immersion in the solution.....	145
Figure 7.6 OCP of X52 steel in basic soil solution as a function of time.	146
Figure 7.7 The R_p values fitted from the LPR measurements on X52 steel in the base soil solution.	147
Figure 7.8 SEM images obtained for X52 steel in base soil solution at various immersion times: (a, b) 10 days, (c, d) 20 days, (e, f) 30 days.	149
Figure 7.9 SEM images of X52 steel after 30 days of immersion in the soil solutions containing various Cl ⁻ concentrations: (a) 50 ppm, (b) 500 ppm, (c) 5000 ppm. ...	150
Figure 7.10 Optical images of X52 steel after 30 days of immersion in the soil solutions containing various Cl ⁻ concentrations upon removal of corrosion products: (a) 5 ppm, (b) 50 ppm, (c) 500 ppm, (d) 5000 ppm.	151
Figure 7.11 XRD patterns spectra of the corrosion products on the X52 steel specimen after various times of immersion in the soil solution.....	152
Figure 8.1 Comparison between the modelled polarization curve with experimental data and SYMADEC prediction results included in Flitt et al.'s work [177]......	167
Figure 8.2 Fitting of the modelled curve with the measured polarization curve of X52 steel in the simulated soil solution.	168
Figure 8.3 Deconvolution of the fitted polarization curve to compare the contributions from individual reactions.	169
Figure 8.4 Schematic view of the physical block of the developed model.....	171
Figure 8.5 Comparison of corrosion rates of the steel in the simulated soil solution determined by experimental testing with the modelling results.	177
Figure 8.6 Comparison of the corrosion potential of X52 steel in the simulated soil solution determined by experimental measurements with the modelling results. ..	178
Figure 8.7 Time dependence of the porosity of the corrosion product film.	179
Figure 8.8 Concentration distribution of various species in the solution.	180
Figure 8.9 Dependence of corrosion rate on the dissolved oxygen concentration in the soil solution.....	182

Figure 8.10 Predicted (a) corrosion rate and (b) thickness loss of the steel after a long-term exposure in the soil solution. 183

List of Symbols, Abbreviations and Nomenclature

Symbol	Definition
A	Cross-section area of a tubular
A_M	Margules parameter
a_i	Activity of species i in the liquid phase
$b_{a,j}$	Tafel slope of anodic reaction
$b_{c,j}$	Tafel slope of cathodic reaction
b_{Fe}	Tafel slope of Fe
b_{H_2O}	Tafel slope of H ₂ O
b_{O_2}	Tafel slope of O ₂
CR	Corrosion rate
C_{aq}	Concentration of oxygen in solution
C_b	Bulk concentration of the reactive species
C^{0}_{bicarb}	Initial concentration of bicarbonate ions
C_i	Concentration of species i
C_{O_2}	Oxygen concentrations at the steel surface
$C_{O_2,ref}$	Oxygen concentrations at the air/soil solution interface
C_w	Sand concentration
CPE	Constant phase element
D	Dielectric constant of water
D_j	Molecular diffusion coefficient of species j
D_{O_2}	Molecular diffusion coefficient of O ₂
D_z	Diffusivity of reactive species
d	International diameter of tubular Eq. (2-22)
d_w	Density of the solvent
E	Applied potential in Eqs. (8-2) ~ (8-3)
$E_{arev,j}$	Anodic reversible potential
$E_{crev,j}$	Cathodic reversible potential
E_{corr}	Corrosion potential
E_{rev}	Reversible potential
E_{redox}	Redox potential
$E_{erosion}$	Erosion rate
E_{s-d}	Soil-structure potential
E_{true}	“True” potential
E_w	Determined potential
F	Faraday’s constant
F_{cond}	Effect factor of water condensate on corrosion rate
F_{H_2S}	Effect factor of H ₂ S on corrosion rate
F_{inhib}	Effect factor of inhibitor on corrosion rate
F_{oil}	Effect factor of oil on corrosion rate

$F_{\text{organic acid}}$	Effect factor of organic acid on corrosion rate
F_{scale}	Effect factor of scale on corrosion rate
f_i	Fugacity of gas component i
g	Gravity acceleration rate
h	Height of the fluid
I	Ionic strength
	Current in Eq. (8-8)
i	Total current density
$i_{0,\text{Fe}}$	Exchange current density of Fe
$i_{0,\text{H}_2\text{O}}$	Exchange current density of H ₂ O
i_{0,O_2}	Exchange current density of O ₂
$i_{a,j}^0$	Anodic exchange current density of j
$i_{c,j}^0$	Cathodic exchange current density of j
i_{corr}	Corrosion current density
i_c	Current density of a cathodic reaction
i_{ct}	Component of the charge transfer current density
i_{Fe}	Current density of Fe
$i_{\text{H}_2\text{O}}$	Current densities of H ₂ O
i_j^{exp}	Experimentally measured current density
i_j^{theory}	Theoretical predicted current density
i_L	Limiting current density
i_{lim}	Component of the diffusive limiting current density
i_{O_2}	Current densities of O ₂
K	Reaction equilibrium constant in Eq. (5-2) ~ (5-3)
K^0	Equilibrium constant at the reference pressure
K_{bi}	Equilibrium constant of dissociation of bicarbonate
$K_{\text{b,hy}}$	Backward reaction constant
K_{ca}	Equilibrium constant for dissociation of H ₂ CO ₃
$K_{\text{f,hy}}$	Forward reaction constant
K_{hy}	CO ₂ hydration equilibrium constant
K_{sol}	Equilibrium constant of dissolution of CO ₂ gas in water
K_{spFeCO_3}	Solubility of iron carbonate
$K_{\text{spFe(OH)}_2}$	Solubility of Fe(OH) ₂
K_{wa}	Equilibrium constant for dissociation of water
k	Boltzmann's constant
$k_{\text{b,hy}}$	Backward CO ₂ hydration rate constants
k_{eff}	Effective rate coefficient
$k_{\text{f,hy}}$	Forward CO ₂ hydration rate constants

L	Inductance
$M_{\text{H}_2\text{O}}$	Molecular weight of water
M_{Fe}	Fe molecular weight
M_{FeCO_3}	FeCO ₃ molecular weight
$M_{\text{Fe(OH)}_2}$	Molecular weight of Fe(OH) ₂
m_i	Molality (mol/kg H ₂ O) of species i
m_{salt}	Molality of a salt compound
n	Number of electrons/mole exchanged in a redox reaction
	Total number of data points in Eq. (8-1)
n_j	Number of electrons exchanged per mole of species j
n_a	Total number of anodic reactions
n_c	Total number of cathodic reactions
N_j	Flux of species j
N_0	Avogadro's number
P	Total pressure
	Pit depth in Eq. (2-27) ~ (2-28)
P^0	Reference pressure
P_{CO_2}	Partial pressure of CO ₂
P_{O_2}	Partial pressure of O ₂
P_s	Saturation pressure of water
p	Hydrostatic pressure
Q	Flow flux
R	Universal gas constant
	Film resistance in Eq. (8-8)
Re	Reynolds number
R_{FeCO_3}	Precipitation rate of FeCO ₃
$R_{\text{Fe(OH)}_2}$	Precipitation rate of Fe(OH) ₂
R_j	Source or sink of species j due to chemical reactions
R_L	Inductive resistance
R_p	Charge transfer resistance
R_s	Solution resistance
SSV	Total sum of squared differences
T	Temperature in kelvin
T_c	Temperature in degree Celsius
T_f	Temperature in degree Fahrenheit
T_{ref}	Temperature in kelvin at reference conditions
t	Time
t_0	Pit initiation time
U_{liq}	Fluid flow velocity
U_p	Flow velocity of solid particles
V	Water cut
	Mole volume of the gas phase in Eq. (5-15)

\bar{V}_i	Average partial molar volume of pure component i over the pressure interval P^0 to P
V_{corr}	Corrosion rate
$V_{\text{H}_2\text{O}}$	Volume of water condensate
V_m	Mass transfer rates of the dissolved CO_2
V_r	Maximum kinetic reaction rates of protons
W	Average water fraction in the liquid
W_{break}	Breakpoint of water in oil-water emulsion
x	Spatial coordinate
x_i	Mole fraction of species i in solution
y_i	Mole fraction of component i
$ Z $	Modular value
z_j	Charge number of ion j
<i>Greek</i>	Definition
α	Deviation angle of the tubular relative to the vertical direction
γ_i	Activity coefficient of species i in the liquid phase
ΔH	Activation energy
$\Delta P/L$	Pressure drop gradient
δ	Thickness of the water condensate film
	Thickness of the stagnant layer at the electrode in Eq. (7-1)
ε	Porosity of scale
	Dielectric constant or the relative permittivity of water in Eq. (6-19)
ε_0	Permittivity of free space
ψ	Fugacity coefficient of CO_2 gas
ϕ	Electric potential in the solution
ϕ_i	Fugacity coefficient of component i
σ	Ratio of surface area over the volume of FeCO_3 precipitate
κ	Surface permeability of the scale
μ_j	Mobility of species j
v	Instantaneous velocity
v_p	Minimum average corrosion rate
ρ	Soil resistivity
	Density of the fluid in Eq. (3-2)
ρ_{Fe}	Density of Fe
ρ_{FeCO_3}	Density of FeCO_3
$\rho_{\text{Fe(OH)}_2}$	Density of Fe(OH)_2
τ	Wall shear stress
ν	Stoichiometric number of ions contained in dissolved salt
	Specific volume of water in Eq. (B-6)
Abbreviation	Definition

AER	Alberta Energy Regulator
bb1	Barrel
CCS	Carbon capture and storage
CE	Counter electrode
CFD	Computational fluid dynamics
CP	Cathodic protection
DO	Dissolved oxygen
EOR	Enhanced oil recovery
EOS	Equation of state
EIS	Electrochemical impedance spectroscopy
FAC	Flow-accelerated corrosion
GDP	Gross domestic product
GHG	Greenhouse gas
GRG	Generalized reduced gradient
HIC	Hydrogen induced corrosion
LPR	Linear polarization resistance
MIC	Microbially influenced corrosion
NIST	National Institute of Standard and Technology
NSERC	Natural Science and Engineering Research Council of Canada
OCP	Open-circuit potential
PE	Polyethylene
PTFE	Polytetrafluoroethylene
RDS	Rate-determining step
RE	Reference electrode
RK	Redlich-Kwong
SAGD	Steam-assisted gravity drainage
SCC	Stress corrosion cracking
SCE	Saturated calomel electrode
SEM	Scanning electron microscope
VOF	Volume of fluid
WE	Working electrode
XRD	X-ray diffraction
ZRA	Zero-resistance ammeter

Superscript/Subscript	Definition
<i>a</i>	Anions
<i>c</i>	Cations
<i>f</i>	Film
<i>g</i>	Gas phase
<i>l</i>	Liquid phase

Chapter One: Introduction

1.1 Research background

Corrosion is the gradual degradation of a metal by chemical or electrochemical reactions with the environment. Corrosion can result in metal loss and degrade mechanical properties of the metal [1], thus acting as a vital threat against asset integrity and production assurance, and leading to enormous economic loss. It is estimated that the global cost of corrosion is US\$2.5 trillion, which is about 3.4% of the global Gross Domestic Product (GDP) [2]. Particularly, corrosion has been the primary mechanism causing facility failures in oil industry, which takes more than a half of all the corrosion cost in U.S. industries [3].

In all stages of oil production, from downhole to above-ground equipment and further transportation to processing facilities, corrosion attacks metal components at every stage in the life of oil industry [4-6]. Downhole tubulars, above-ground gathering pipelines and buried transmission pipelines constitute important facilities in oil production and transportation. Corrosion problem of these facilities is severe, not only because of the hostile and corrosive environments they are exposed to, but also because they have a very large proportion of assets in the whole industry. It is estimated that 42.9% of the total annual cost of corrosion in the oil and gas production industry is related to surface pipelines and facilities, with downhole tubing accounting for another 33.7% [7].

By differentiating environments, corrosion can be classified as internal corrosion, which happens inside the pipe/tubing, and external corrosion on the external surface of

facilities. According to an Alberta Energy Regulator (AER)'s report, internal corrosion is the leading cause of pipeline failures, representing 54.8 percent of all releases. External corrosion is the second leading cause of pipeline failures, at 12.7 percent [8].

Internal corrosion happens in most pipelines, especially those in the upstream gathering system. Pipelines carry raw oil fluids that typically contain water of varying chemistry and salinity, along with acid gases, such as CO₂ and H₂S. When CO₂ dissolves in water, carbonic acid is formed and CO₂ corrosion is caused. Corrosion rate of steels in CO₂-containing environments at a given solution pH is even higher than that in strong acids at the same pH [9]. Approximately 28% of all corrosion-related failures in oil industry is attributed to CO₂ corrosion [10].

External corrosion of pipelines occurs when the pipe steel is directly or indirectly exposed to the soil environment. For in-service pipelines, they are always protected from corrosion by coatings and cathodic protection (CP). Corrosion only takes place when both the coating and CP fail. For abandoned pipelines in soils, coatings are usually aged over a long time period of service, and CP may or may not be maintained. Corrosion is expected to occur on the pipeline during abandonment in the soil, causing integrity degradation and structural failure. The structural integrity of abandoned pipelines is important because abandoned pipelines are supposed to support the soil load and live loads above the pipeline for hundreds of years or even longer [11]. Thus, corrosion is the primary threat against the structural integrity of abandoned pipelines.

To understand corrosion phenomenon and processes, and further, to develop proper techniques for effective corrosion control and management, methods and techniques have been developed for these purposes. Generally, experimental testing helps understand

corrosion mechanisms of metals in a certain environment under given conditions. However, experiment-based research is often time-consuming and expensive. More importantly, it is sometimes very difficult, if not impossible, to conduct the tests under controlled environmental conditions to simulate the reality encountered in practice.

Corrosion modelling simulates corrosion processes based on basic physicochemical laws and electrochemical corrosion principles, providing a promising alternative over experimental testing for corrosion evaluation and long-term prediction. Corrosion modelling has been regarded as one of the main methods in materials selection and corrosion allowance determination [12]. In addition, the modelling results can provide guidance for facility maintenance and asset integrity management. In fact, corrosion modelling has been essential in helping industry to make critical decisions to evaluate the performance of metals and predict their reliability in a wide variety of corrosive environments, including those in oil industry [13].

Although the modelling method has been used for corrosion evaluation and prediction in oil industry, significant gaps still exist in either further improvement of the modelling accuracy and reliability or development of new models for corrosion occurring in increasingly severe environments. The former includes the upstream gathering pipelines carrying corrosive oil-water emulsions, and the latter includes corrosion of downhole tubulars in high-temperature high-pressure CO₂-containing environments, supercritical CO₂ storage, abandoned pipelines in soils, etc. To meet the immediate industry needs, and at the same time, improve our understanding to steel corrosion occurring in various harsh corrosive environments, which were not studied or fully understood previously, this research develops a number of mechanistic models, which,

combined with numerical computation, advance our understanding to these corrosion phenomena and provide a reliable methodology for corrosion prediction. It is attempted to contribute to a strong science base in corrosion area, and develop highly feasible solutions for effective corrosion management in oil industry.

1.2 Objectives

The overall objective of this research is to mechanistically model a number of corrosion phenomena occurring under various environments and conditions encountered in oil industry, and to numerically predict the long-term corrosion rates under the given conditions. Progresses will be made in the following areas:

- To improve the understanding of corrosion of pipeline steel in CO₂-saturated single-phase water and oil-water emulsion flow. To develop a model enabling prediction of corrosion rate of the pipeline in oil-water emulsion flow.
- To develop a model to predict corrosion rate of steel tubulars in SAGD/CO₂ co-injection system.
- To develop a mechanistic model to predict corrosion of steel tubing in CO₂ storage.
- To understand the corrosion mechanism of abandoned pipelines in a simulated soil solution, and to develop a mechanistic model to predict the long-term corrosion rate of the steel.

1.3 Contents of the thesis

The thesis contains nine chapters, with Chapter One briefly introduces the research background and objectives of this work.

Chapter Two presents a comprehensive review on the state-of-the-art of oilfield and pipeline corrosion relevant to this research, including: (1) mechanism of CO₂ corrosion of pipelines and the parametric effects; (2) corrosion mechanism of abandoned pipelines in soil environments; and (3) existing models for prediction of CO₂ corrosion and soil corrosion.

Chapters Three to Eight include the research outcomes. Particularly, Chapter Three presents investigation of the non-uniform corrosion of an X65 steel pipe in a CO₂-saturated single-phase water using a home-made flow loop. Chapter Four includes the experimental study of the corrosion of X65 pipeline steel in a CO₂-saturated oil-water emulsion flow. Corrosion mechanism and the parametric effects, i.e., fluid flow velocity, temperature and the oil content in the fluid, on corrosion are discussed. The CFD simulation is used to derive flow parameters, which are used as inputs for the corrosion rate prediction by a developed semi-empirical model. In Chapter Five, the development of a semi-empirical mode to calculate and predict corrosion rates of both injection and production steel tubulars in SAGD/CO₂ co-injection system is present. Chapter Six introduces the development of a mechanistic model, which enables water chemistry calculation and corrosion rate prediction of steel tubing, for CO₂ storage. Chapter Seven studies the corrosion mechanism of abandoned pipelines made of X52 steel in a simulated soil solution and the parametric effects, i.e., the content of dissolved oxygen (DO), solution pH, Cl⁻ concentration and immersion time. Chapter Eight presents a

mechanistic model, which combines both mass transfer of corrosive species in the soil solution and electrochemical reactions at the steel/solution interface, to predict long-term corrosion rate of the steel in the soil solution. A computational program, which is able to derive corrosion kinetic parameters for corrosion rate determination, is developed.

Chapter Nine summaries the main conclusions that are drawn from this research. Recommendations for the future work are also given.

Chapter Two: Literature review

2.1 Corrosion as a primary mechanism resulting in facility failures in oil industry

In oil industry, crude oil is produced from the underground reservoirs. Before it reaches the end users, the oil must be transported and processed. At any stage in the oil industry, oil flows through tubulars, piping and pipelines, all of which should withstand the designed operating conditions, and work safely to prevent oil from leaking. Once oil leaking occurs, the consequence is serious, resulting in contamination of surrounding soils and water, increased safety concern of nearby people and communities, and direct and indirect economic loss to both the company and the society. Failures can happen on the facilities due to a lot of reasons, such as mechanical damage, welding defects, fabrication defects, etc. Particularly, corrosion has been acknowledged as the leading cause, and is responsible for around 33% of all failures encountered in oil industry [10].

The essential condition for corrosion to happen is the formation of a corrosion cell. A basic corrosion cell is comprised of an anode (where an oxidation reaction occurs), a cathode (where the reduction reaction occurs), and a conducting electrolyte [14]. As shown in Figure 2.1, a vulnerable metal can be both the anode and the cathode. The only difference is that the anodic area corrodes while the cathodic area does not. Instead, the cathodic area becomes the place for cathodic reactions, such as the reduction of H^+ and O_2 , to happen. The conducting electrolyte is usually a salt solution. The salinity or resistivity of the solution also affects the corrosion rate.

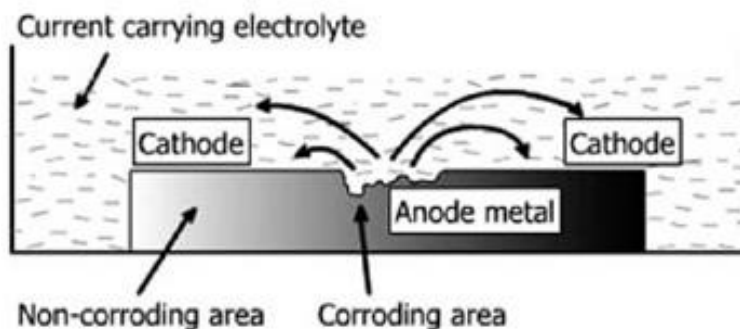


Figure 2.1 Components of a corrosion cell [14].

In the oil industry, almost all facilities and equipment are made of steels, especially carbon steels [7], various corrosive environments and operating conditions in different production sectors have been found to result in a wide variety of corrosion types, including general corrosion, localized corrosion, stress corrosion cracking (SCC), flow-accelerated corrosion (FAC), erosion, erosion-corrosion, hydrogen-induced corrosion (HIC), microbially influenced corrosion (MIC), etc. [15].

With respect to locations where corrosion happens, it can be classified into internal corrosion, which happens at the interior of facilities and/or equipment, and external corrosion at the outer surface of the facilities. The above-ground pipelines in the upstream gathering system carry raw fluids, which are not yet processed, between oil wells and processing facilities. The pipelines usually suffer from severe internal corrosion. The constituents of the carried fluids are very complex. While the majority part could be oil and water, CO_2 also exists at an appreciable content. CO_2 corrosion happens on pipelines when CO_2 gas is dissolved in water to form carbonic acid. Moreover, a mixture of oil and water can make a multiphase flow, in which the fluid flow

affects the corrosion process and corrosion rate, adding to adverse effects from other factors, such as temperature, solution chemistry, etc.

The downhole environment is always highly corrosive, including corrosive gases CO₂ and H₂S, which are produced with oil extraction at high content, brine water and multiple chemical species, etc. [16, 17]. Field data indicated that the corrosion rate of carbon steel downhole tubulars can be up to 10 mm/year or above [18, 19]. With the growing demand for oil and gas in modern society, the oil exploration and production go into even deeper reservoirs [20], where the environments become more hostile and more corrosive, and are under high temperature and high pressure. Furthermore, technologies for enhanced oil recovery (EOR), such as SAGD for heavy crude oil production [21], water injection [22] and gas injection [23, 24], introduce massive amount of water and high-temperature high-pressure gases to the reservoir. All of them result in generation of extremely corrosive environments.

Pipeline abandonment occurs when a pipeline permanently ceases to provide service due to the situation that it reaches its maximum service life or the pipeline is no longer able to provide safe and economical service [25]. For abandoned pipelines that are left in soils, there will not be fluids and high internal pressure inside the pipelines after they are cleaned and processed as required [26]. Internal corrosion shall not be a big issue for them, only if a pipe is totally perforated at some locations after a long time left in the ground and water with corrosive species flows in. However, external corrosion could happen. Abandoned pipelines can be buried in a typical soil environment as shown in Figure 2.2 [11]. The pipeline outer surface is surrounded by soil, and the water content in the soil varies a lot depending on the level of water table and the precipitation. Gases,

such as O_2 and CO_2 , can dissolve in the wet soil and create a corrosive environment. Because the abandoned pipelines are generally aged, they may not have coatings on the outer surface, or have old coatings like coal tar or polyethylene (PE) tape, which have degraded and lost the ability for corrosion protection. When the outer surface of the abandoned pipeline is directly exposed to soil or contacts electrolyte generated from the soil environment, external corrosion will occur.

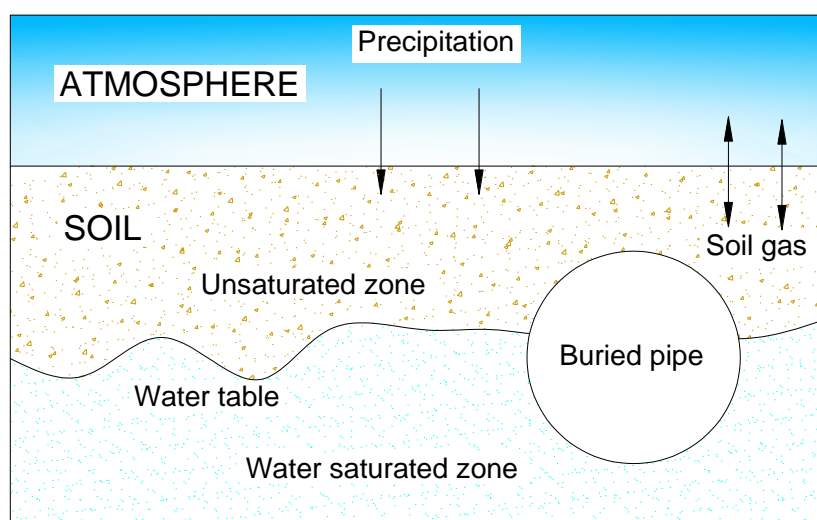


Figure 2.2 A schematic diagram of the soil environment experienced by the buried pipeline [11].

2.2 CO_2 corrosion of above-ground pipelines and downhole tubulars

2.2.1 CO_2 corrosion mechanisms

CO_2 corrosion is the most prevalent corrosion form in oil industry. Since it was recognized in the 1940s, extensive work has been conducted to study the corrosion mechanism and corrosion rate of steels under specific conditions, and the corrosion control techniques [27]. Carbon steel corrosion under CO_2 -containing environments is

very complex, especially in the downhole environments. Attempts to elucidate the corrosion mechanism and the involved electrochemical reactions have never been stopped. A well-established mechanism is critical to develop accurate models for the corrosion prediction and evaluation.

CO₂ corrosion of carbon steels occurs subject to dissolution of gaseous CO₂ in aqueous phase [27], which is common in hydrocarbon production and transportation. Dissolved CO₂ in water generates carbonic acid, which then partially dissociates to form hydrogen ions and other species such as bicarbonate ions and carbonate ions. The relevant chemical reactions include:



The combination of CO₂ with water to form carbonic acid, which is also known as CO₂ hydration, is a slow process. As a result, it becomes the rate-determining step (RDS) in CO₂ corrosion [28]. The overall corrosion reaction of steels in CO₂-containing environments is:



This corrosion reaction can be further described by electrochemical anodic and cathodic reactions. The anodic reaction is primarily the oxidation of iron:



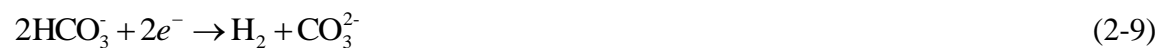
The cathodic reactions in CO₂ solutions are pH dependent. At pH < 4, the dominant reaction is the proton reduction.



When pH is between 4 and 6, and under moderate to high CO₂ pressures ($P_{\text{CO}_2} > 10$ bar), the reduction of carbonic acid is the dominant cathodic reaction.



The reduction of HCO₃⁻ ions is only important in more alkaline solutions where the solution pH is larger than 5.



The reduction of water becomes important when the CO₂ partial pressure is much smaller than 1 bar and pH > 5 [29].



In the presence of organic acids such as acetic acid (HAc), the acid could be reduced to introduce an additional cathodic reaction by [30]:



When the solubility of FeCO₃ is exceeded, corrosion scale, i.e., iron carbonate, can be formed by:



2.2.2 Effect of fluid flow

FAC refers to the corrosion that is remarkably enhanced by fluid flow conditions. In addition, erosion corrosion could happen and lead to more severe metal loss when sand particles are entrained in the fluid.

There have been extensive studies investigating the effect of fluid flow on CO₂ corrosion of pipelines. The majority of the work [31-33] were conducted on steel specimens using autoclave or rotating electrode techniques. These testing methods suffer

from the shortcoming that they are incapable of reproducing the hydrodynamic conditions, such as wall shear stress and fluid flow patterns, which are typical of the pipe flow. As a result, the obtained results are not representative of the reality of pipeline corrosion. Alternative methods, such as flow loops [34, 35], have been developed in laboratory to enable generation of fluid dynamics similar or even identical to that of the actual pipe flow.

The CO₂ corrosion of pipelines under flow conditions occurs under a synergistic effect of electrochemical reactions, mass transfer and wall shear stress [36, 37]. It was suggested [9] that the fluid flow can enhance the transport of species to and away from the steel surface in the absence of protective scales. This idea was further illustrated by a mechanistic model [29], which demonstrated that the thickness of the liquid boundary layer is smaller at higher flow velocities, thus exhibiting a lower resistance to the transport of corrosive species from the bulk solution to the steel surface. It was also suggested that the fluid flow affected the formation and protective property of the surface scale. Zhang and Cheng [38] studied the role of fluid hydrodynamics in FAC of an X65 pipeline steel in CO₂-saturated oilfield formation water. They found that an increasing flow rate and shear stress could thinner or even remove the iron carbonate scale, leading to increased corrosion of the steel.

Oily phase contained in the fluid remarkably affects the corrosion of the steel pipe [39, 40]. Generally, when the interior of a pipe is oil-wetted, i.e., the steel surface is covered by oil, corrosive species existing in aqueous phase are not able to reach the steel to cause corrosion. Thus, the oil can inhibit internal corrosion of pipelines. However, the maintenance of oil-wetting of pipe steel depends on the properties of the oil-water

emulsion and the fluid hydrodynamics, such as the amount of oil relative to that of water, flow velocity, temperature, pipe size, etc. [41].

2.2.3 Effects of pressure and temperature

Zhang et al. [42] studied corrosion of X65 pipeline steel under a low CO₂ partial pressure and supercritical CO₂ conditions. It was suggested that the supercritical CO₂ corrosion was mechanistically identical to CO₂ corrosion occurring at low pressures. The change in CO₂ partial pressure did not affect the chemical and electrochemical reactions occurring during steel corrosion. However, the corrosion rate at supercritical CO₂ conditions was much higher than that at low CO₂ pressures because more CO₂ was dissolved in water and generated a more acidic condition.

Previously, Henry's law was used to calculate the concentration of dissolved CO₂ in water [43]. However, Henry's law constant, which is valid for the low CO₂ pressure conditions, does not apply and gives conservative results for high CO₂ pressure conditions [44].

Lin et al. [45] studied the effect of pressure on CO₂ corrosion of steels. The results showed that an increased CO₂ partial pressure contributed to increasing thickness of the corrosion scale and its grain size. There was a critical pressure at which the thickness and grain size of the scale reached the maximum value.

Generally, temperature affects electrochemical reactions, mass transfer rate and the formation of corrosion product film on the steel surface. Wu et al. [46] investigated corrosion of a carbon steel in a static oilfield produced water saturated with supercritical CO₂. It was showed that the corrosion scale formed at a higher temperature was more

protective than that formed at a lower temperature, which was due to the faster formation of the film at elevated temperatures. The film became more compact and continuous with the elevated temperature. When the iron carbonate scale was formed on the steel surface, corrosion could be reduced by increasing energy barrier for electrochemical charge-transfer reactions, and a blocking effect on the transport of reacting species towards the steel surface [9]. Liu et al. [47] confirmed the protective effect of corrosion scale, and suggested that the corrosion rate of the SAGD produced gas lines was low or moderate even though the produced gas contained H₂S and CO₂, and experienced very high temperatures.

At normal conditions, the dominant scale formed during CO₂ corrosion of steels is made up of FeCO₃. Growth of FeCO₃ is temperature-dependent. The scale is not protective until the temperature is above 50 °C [27]. At elevated temperatures, i.e., 150 °C or above, the corrosion products contain a mixture of FeCO₃ and Fe₃O₄ or exclusively Fe₃O₄. The Fe₃O₄ can be generated by [48]:



Tanupabrungsun [48] proposed that Fe₃O₄ may provide more protection to the steel than FeCO₃, which was attributed to its ability to passivate the steel. However, for the Fe₃O₄ scale generated under high temperature high pressure conditions, there has been limited investigation in terms of its role on steel corrosion.

Temperature also affects the solubility of CO₂ in solutions. Generally, the amount of dissolved CO₂ decreases when temperature is increased [49].

2.3 Corrosion of abandoned pipelines in soils

2.3.1 Corrosion mechanism

Corrosion of abandoned pipelines in soils happens when the pipelines are either directly in contact with the soil or in contact with electrolyte trapped under disbonded coating. The soil environment remarkably affects the corrosion behavior of the abandoned pipeline. Previous studies on corrosion of steels in soils showed that soil corrosion depended on a number of factors, including soil resistivity, dissolved salts, moisture, pH, oxygen concentration, bacteria, etc. [50]. Difference in physical properties and chemical composition of soils from site to site can lead to totally different corrosion behavior and corrosion rates.

In general, the anodic reaction in soil corrosion is the oxidation of iron, as shown in Reaction (2-6). Oxygen is the dominant cathodic depolarizer in aerated soils, and the reduction of dissolved oxygen in water is [51]:



If the soil is at near-neutral pH condition, cathodic reaction may also include the reduction of water (Reaction (2-10)).

The generated Fe^{2+} and OH^- from the electrochemical reactions further react to form corrosion products $\text{Fe}(\text{OH})_2$ on the steel surface, which can reduce the corrosion rate [52]:



The $\text{Fe}(\text{OH})_2$ is not stable, which, when exposed to aerated conditions, will transform to FeOOH , Fe_2O_3 and Fe_3O_4 . The relevant chemical and electrochemical reactions may include [53, 54]:



Although the corrosion products formed on the steel surface are supposed to affect the steel corrosion rate in soils, their protectiveness is still under debate, and has not yet been fully understood [51].

2.3.2 Parametric effects

Gassing condition is one of the most important parameters that affect corrosion of a pipeline in soils. The two common gases, i.e., CO_2 and O_2 , can affect both the corrosion mechanism and corrosion rate. Generation of CO_2 is associated with the rotten plants and/or microbial metabolism in the soil [55]. As mentioned above, when CO_2 dissolves in water, a weak acid, i.e., H_2CO_3 , is formed to decrease the solution pH and enhance the steel corrosion. Different from CO_2 , dissolved oxygen directly participates in the cathodic reaction during corrosion of the steel in soils [53]. It was found that the presence of DO significantly accelerated the corrosion rate [63]. Moreover, the DO concentration affects the composition of corrosion products [65]. Particularly, the presence of oxygen is in favor of the growth of passive film on steel.

Oxygen can be consumed by corrosion reactions and/or plant breathing. Thus, transportation of oxygen from the bulk soil to the steel surface is critical to the corrosion reaction. Any soil properties affecting the oxygen transportation will also affect the corrosion rate of the steel. Soil moisture can affect the oxygen transportation in soils. Gupta et al. [56] suggested a “critical soil moisture content”, above which corrosion of steels was decreased because the oxygen diffusion in the soil solution was slower than that in porous dry soils. Other soil properties, such as soil type and soil particle size, also influence the corrosion by affecting the oxygen content or oxygen diffusion [57].

Soil resistivity affects steel corrosion, and depends on the soil moisture and the contained soluble ions [50]. Usually, a high soil moisture and ionic concentration is associated with a low soil resistivity, leading to a high corrosion rate. Ikechukwu et al. [58] found that the soil resistivity was more important than soil pH to affect the steel

corrosion. Soil resistivity is actually a combined effect of multiple chemical ions, such as Cl^- , all of which affect the corrosion of steel pipes in soils [59, 60].

2.4 Corrosion prediction models

2.4.1 Modelling as an effective methodology for corrosion management

Corrosion is a natural process. To effectively control corrosion problems, it is important to evaluate the corrosion data and predict the residual service life. Experimental testing is essential to determine the corrosion mechanism of a metal in certain environments and the parametric effects on corrosion. However, experimental testing suffers from the shortcoming that it is, sometimes, unable, or at least difficult, to reproduce the reality. Moreover, the modelling can predict corrosion of metals during long-term exposure to environments, which is usually impossible to test by experimental methods.

Prediction models are developed based on either field or experimental data. A well-established corrosion prediction model should be able to describe the direct or indirect (underlying physical-chemistry process) relationship between corrosion rate and the inputs correctly, thus giving correct predictions. The reliability of a corrosion prediction model is strongly dependent on the mechanism and parameters obtained from experimental studies or field data. However, when a model is established, it can be useful to evaluate and predict corrosion under similar conditions and even extrapolate to some other conditions.

Corrosion prediction models have been developed for several decades. Rossum [61] derived an early external corrosion model to predict pitting corrosion rates of ferrous

metals in soils in 1969. De Waard and Milliams [62] proposed the earliest model to predict CO₂ corrosion in 1975. Since then, more models have been developed based on them for CO₂ corrosion prediction [63]. Some oil companies, such as BP [64], developed their own models to predict CO₂ corrosion to guide their operations.

According to numerical methods used to correlate with the corrosion mechanism and processes, the developed models can be grouped into three categories, i.e., empirical models, semi-empirical models and mechanistic models [9].

Empirical models: These models have very little or no theoretical background. Most constants used in them have no physical meaning – they are just best-fit parameters to the available results. When calibrated with a very large and very reliable experimental database, these models can give good interpolation. However, any extrapolation leads to unreliable results. Addition of any new knowledge to these models is rather difficult and often requires recalibration of the whole model. Alternatively, correction factors can be added with a large degree of uncertainty related to their interaction with the existing empirical constants.

Semi-empirical models: These models are only partly based on firm theoretical hypotheses. They are for practical purposes extended to areas where insufficient theoretical knowledge is available. Some of the constants in these models have a clear physical meaning while others are arbitrary best-fit parameters. Calibrated with a sufficiently large and reliable experimental database, these models can enable good interpolation predictions. However, extrapolation can lead to unreliable and sometimes physically unrealistic results. New knowledge can be added with moderate effort by adding correction factors and/or by doing a partial recalibration of the model constants.

Mechanistic models: These models describe the mechanisms of the underlying reactions and have a strong theoretical background. Most constants in this type of models have a clear physical meaning. Many of the constants are easily found in the literature, while some still have to be obtained by comparing the predictions with available experiments. When calibrated with a reliable (and not necessarily large) experimental database, this type of models enable accurate and physically realistic interpolation, and good extrapolation predictions. It is easy to add new knowledge to these models with minor modification of the existing model and without having to recalibrate all the model constants.

Obviously, mechanistic models possess unique advantages over the empirical/semi-empirical models in corrosion prediction. Nevertheless, the complex nature of corrosion processes makes it quite difficult to develop a mechanistic model under all conditions. In oil industry, the accuracy and reliability of a corrosion prediction model are equally important. Moreover, the simplicity of modelling operation and production of straightforward outputs are also pursued [64].

2.4.2 Modelling of CO₂ corrosion of pipelines in fluid flow

Norsok M506 model [65] is an empirical model developed by the Norwegian petroleum industry to predict CO₂ corrosion of pipelines in fluid flow. In this model, the corrosion rate was expressed as a function of temperature, solution pH, wall shear stress and CO₂ fugacity. The effect of flow on corrosion was included through the relationship between the corrosion rate and wall shear stress. However, the calculation of wall shear stress only applied for the water and gas mixture, where oil was not considered.

Kanwar et al. [66] established an empirical model based on their experimental studies of CO₂ corrosion in oil/water fluid flow using a horizontal pipe loop. The corrosion rate was written as:

$$CR = kP_{\text{CO}_2}^c \tau^b \quad (2-20)$$

where CR is the corrosion rate, mm/year; k is a corrosion rate coefficient; P_{CO_2} is the CO₂ partial pressure, MPa; τ is the wall shear stress, N/m²; and c and b are constants.

De Waard et al. [62, 67-72] developed a series of semi-empirical models which were used for CO₂ corrosion prediction in flow conditions. The base equation to calculate CO₂ corrosion rate, V_{corr} (mm/year), was expressed as [70]:

$$\frac{1}{V_{\text{corr}}} = \frac{1}{V_r} + \frac{1}{V_m} \quad (2-21)$$

where V_r is the highest possible reaction rate, mm/year; and V_m is the highest mass transfer rate of corrosive species, mm/year. The following relationships were applied:

$$\log(V_r) = 4.84 - \frac{1119}{T} + 0.58 \log(\psi P_{\text{CO}_2}) - 0.34(\text{pH}_{\text{actual}} - \text{pH}_{\text{CO}_2}) \quad (2-22)$$

$$V_m = 2.7 \frac{U_{\text{liq}}^{0.8}}{d^{0.2}} \psi P_{\text{CO}_2} \quad (2-23)$$

where $\text{pH}_{\text{actual}}$ and pH_{CO_2} are the actual pH of the solution and the pH of pure water dissolved with CO_2 , respectively; U_{liq} is the fluid flow velocity, m/s; and d is the internal diameter of the pipe, m. For different steels, the equation used for calculation of V_r can be different. The effects of protective scale and various species, such as H_2S , oil, organic acids and inhibitors, on corrosion rate were considered with correction factors [68]:

$$\text{Total corrosion rate} = V_{\text{corr}} \times F_{\text{scale}} \times F_{\text{H}_2\text{S}} \times F_{\text{oil}} \times F_{\text{cond}} \times F_{\text{inhib}} \times F_{\text{organicacid}} \quad (2-24)$$

where F_{scale} , $F_{\text{H}_2\text{S}}$, F_{oil} , F_{cond} , F_{inhib} and $F_{\text{organicacid}}$ represent the effect factors of the protective scale, H_2S , oil, water condensate, inhibitors and organic acids, respectively. Many semi-empirical models, such as the Hydrocor developed by Shell, Cassandra implemented by BP, etc. [63], were developed based on this model.

Mechanistic models for CO_2 corrosion prediction can be divided into two groups, i.e., electrochemical models and mass transport based electrochemical models. One typical electrochemical model, i.e., “Point model” [73], was developed based on the model of Grey et al. [74, 75] and extended to predict the corrosion rate of steels caused by CO_2 , H_2S , organic acids and/or O_2 . In the “Point model”, simplified Tafel equations were directly used to derive the current densities of anodic reactions and activation-controlled cathodic reactions. For the current density of an individual cathodic reaction that may be controlled by a combination of activation and diffusion steps, the equation was expressed as [73]:

$$\frac{1}{i_c} = \frac{1}{i_{ct}} + \frac{1}{i_{lim}} \quad (2-25)$$

where i_c is the current density of the cathodic reaction, A/m²; i_{ct} is the component of the charge transfer current density, which is calculated with the simplified Tafel equation, A/m²; and i_{lim} is the component of the diffusive limiting current density, which is a function of mass transfer coefficient and the concentration of the species in the bulk solution, A/m². The “Point model” can predict corrosion rate with simple calculations. However, it did not consider the scale formation and the effect on corrosion processes. The predicted results represented the worst-case scenario for steel corrosion.

The mass transport based electrochemical models considered the identical chemical and electrochemical reactions to the “Point model”, but the methodology was more complicated. The corrosion rate was calculated based on the concentration of reactive species on the metal surface. Transport of the species between the metal and bulk solution and the transport of species through porous corrosion scale were determined with the species conservation equation [76]:

$$\frac{\partial(\varepsilon C_j)}{\partial t} + \frac{\partial(N_j)}{\partial x} = \varepsilon R_j \quad (2-26)$$

where C_j is the concentration of species j , mol/L; N_j is the flux of species j , mol m/(L s); R_j is the source or sink of species j due to chemical reactions, mol/L s; t is time, s; x is spatial coordinate, m; and ε is volume porosity of the scale. The ε changes with time, and

the change rate is a function of the precipitation rate and undermining rate [77]. The flux of species can be described by Nernst-Planck equation, which includes three components, i.e., diffusion, electro-migration and convection:

$$N_j = -\kappa D_j \frac{\partial C_j}{\partial x} - \kappa z_j \mu_j F C_j \frac{\partial \varphi}{\partial x} + \kappa C_j v \quad (2-27)$$

where μ_j is the mobility of species j , kg/(m s), which can be determined by the relationship with diffusion coefficient via Nernst-Einstein equation $D_j = RT_k \mu_j$; κ is surface permeability of the scale, and there is an empirical correlation $\kappa = \varepsilon^{1.5}$ [29]; R is the ideal gas constant, 8.3143 J/mol K; F is Faraday's constant, 96485 C/mol; φ is the electric potential in the solution, V; v is the instantaneous velocity, m/s; and D_j is the molecular diffusion coefficient of species j , m²/s.

Currently, many models are developed based on the methodology of the mass transport based electrochemical model, which enables predictions of both uniform and localized CO₂ corrosion [16, 29, 77-82]. Song et al. [43, 83, 84] developed a series of mechanistic models to predict CO₂ corrosion rate in oil and gas production and transportation systems.

The CO₂ corrosion prediction models mentioned above simplified the calculations by considering single phase fluid flow only. An integrated CO₂ corrosion-multiphase flow model was proposed [85], where a multiphase model was used to simulate the flow pattern in oil/water multiphase flow.

In our group's previous work, Xu and Cheng [86] developed a finite element based model to predict CO₂ corrosion rate in flow conditions. Three interrelated sub-models, i.e., fluid hydrodynamics, mass-transfer and electrochemical corrosion sub-models, were well integrated to reflect the parametric effects, such as flow velocity, CO₂ partial pressure, pH and temperature, on the steel corrosion. The mutual effects of these parameters were included in the corrosion modelling. The fluid hydrodynamic sub-model applied on the fluid carried by the pipeline. It was assumed that CO₂ was dissolved in water to form the CO₂-saturated, incompressible, single-phase fluid. The Navier-Stokes equations and k - ε turbulence model were used to calculate the fluid flow velocity along the pipe, where a sufficiently long pipe segment was selected to obtain a fully developed fluid flow, i.e., the turbulent dynamic viscosity was a constant along the center of the pipe. The mass-transfer sub-model applied on the fluid/steel interface. The Nernst-Planck equation was used to study the convection, diffusion and migration processes of relevant corrosive species and their concentration gradients in the fluid. Since the fluid flow was in a steady state, i.e., a fully developed fluid was assumed, the concentrations of various corrosive species were uniform in the bulk solution except the boundary layer of the fluid. Inside the boundary layer, the species transported from and to the surface of the pipe steel by convection, diffusion and electro-migration. The mass-transfer coefficient of individual species was included in the sub-model. In the electrochemical corrosion sub-model, steel corroded in CO₂-saturated brine water. The dissolution of iron dominated the anodic reaction, and the cathodic reactions included the reduction of hydrogen ions and carbonic acid. The solution pH was set at about 5, i.e., the typical pH value of brine water saturated with CO₂ in the field. The anodic dissolution reaction was charge-transfer

controlled, and the reaction kinetic parameters, such as exchange current densities and Tafel slopes, were temperature and pH dependent. The cathodic reactions were mix-controlled, including both charge-transfer step and mass-transfer step. The anodic and cathodic current densities were written based on different reaction kinetics equations. While this model was able to provide an accurate prediction of uniform CO₂ corrosion rate, the numerical calculations were quite complicated, and it took too much time to calculate the corrosion rate.

2.4.3 Modelling of CO₂ corrosion in CO₂ storage and high-temperature high-pressure conditions

Nowadays, there has been work to mechanistically model the corrosion of steel tubing under high CO₂ pressure conditions, which, however, are not necessarily identical to those encountered in CO₂ storage. For example, Xiang et al. [87] proposed a model to predict the uniform corrosion rate of CO₂ transportation pipelines in supercritical CO₂-SO₂-O₂-H₂O environments. While the model gave a good prediction of the steel corrosion by comparison with the testing results, the corrosive fluid was not representative of that in CO₂ storage. Moreover, CO₂ was treated as a solvent, and SO₂ and O₂ were regarded as the corrosive species. Han et al. [44] developed a coupled electrochemical-geochemical model to predict corrosion of mild steels in high pressure CO₂-saline environments. Although the solution pH was well modelled, the model did not consider the corrosion scale and its effect on corrosion rate, which caused the prediction results relatively conservative.

High temperature is able to increase CO₂ corrosion rate by enhancing reaction kinetics. At the same time, it also promotes the formation of compact corrosion products that reduce the corrosion rate. An elevated temperature can even change the corrosion mechanism by introducing new corrosion products, i.e., Fe₃O₄. All these scenarios make it difficult to model CO₂ corrosion under high temperature or high-temperature high-pressure conditions. So far, there has been few prediction model available in the literature.

Case et al. [88] tried to use an OLI software to study the corrosive activity of produced fluids under SAGD conditions. Both pH profiles and carbon steel corrosion rates were estimated. However, little information available about the OLI software limits the interpretation and further modification of the model.

2.4.4 Modelling of steel corrosion in soils

There are numerous factors affecting pipeline corrosion in soils. Some factors, such as temperature, soil moisture and resistivity, would even vary with time. To develop a model that consider all affecting factors is very difficult. Empirical or semi-empirical models tend to neglect the underlying corrosion processes or take average of the effect of variations over time by establishing a direct relationship between corrosion rate with some important parameters [50].

Combining theoretical analysis and the National Bureau of Standards (NBS) data of different ferrous metals in a variety of soils for varying time periods, Rossum [61] derived an empirical model:

$$P = Kt^n \quad (2-28)$$

where P is the pit depth, K is a constant, t is time, and n is another constant that depends on the aeration state of soils. This model tried to build the direct relationship between the pit depth and time. Constants were used to account for the effect of all other factors. Based on this model, many empirical models have been developed either by modifying the equation format or correcting the constants. For example, Velazquez et al. [89] proposed a pitting corrosion predictive model of buried pipelines as:

$$P = K(t - t_0)^n \quad (2-29)$$

where t_0 is the pit initiation time.

Obviously, Rossum's model and those based on this model fail to account for many factors that have great effects on the soil corrosion. Thus, the applicability of Rossum's model is very limited. A more complex semi-empirical model was then proposed by Alamilla et al. [90], which was able to estimate the localized corrosion damage on buried steels in soils by:

$$v_p = C_0 \exp[-(q_1 \text{pH} + q_2 \rho + q_3 E_{\text{Redox}} + q_4 E_{s-p})] \quad (2-30)$$

where v_p is the minimum average corrosion rate; C_0 is a scale factor; $q_1 - q_4$ are constants related to environments; ρ is the soil resistivity; E_{redox} is the redox potential; and $E_{\text{s-p}}$ is the soil structure potential.

Both empirical and semi-empirical models share the same disadvantage that they are strongly dependent on the available data in the development and modification process. However, database for specific conditions, such as the soil conditions along an abandoned pipeline, is usually not available, making it impossible to develop an accurate model for corrosion evaluation and prediction on the abandoned pipeline. Moreover, different from operating pipelines, abandoned pipelines suffer from structural failures due to corrosion occurring over a certain area, rather than corrosion pits.

To date, there have been a few work published about mechanistic models developed to study pipeline external corrosion. However, all of them focus on corrosion of operating pipelines with external coating and CP applied. Song et al. [52, 84, 91, 92] developed a series of models to study corrosion of pipeline steels under different modes of coating disbondment, gas environments containing O_2 or CO_2 or both, and CP conditions. These models cannot be used on abandoned pipelines. One of the reasons is that most of them are developed with data obtained in a NS4 solution, i.e., the simulated electrolyte trapped under disbonded polyethylene tape coating [55] where the CP is shielded, rather than typical soil solutions. Furthermore, those models do not consider the effect of corrosion product film on the further corrosion process.

2.5 Summary

Corrosion emerges as the primary mechanism resulting in facility failures in oil industry. Development of accurate and reliable models to predict long-term corrosion rates of steels becomes an important methodology for corrosion management. However, most existing corrosion models are empirical ones, lacking theoretical background. In addition, models used for typical corrosive environments such as SAGD/CO₂ co-injection systems, CO₂ storage and abandoned pipelines in soils are either not available, or the existing models suffer from apparent limitations and need further improvements. All of them constitute the gaps to be addressed for enhanced asset integrity management in oil industry.

Chapter Three: Non-uniform corrosion of steel pipe in CO₂-containing fluid flow *

3.1 Introduction

CO₂ corrosion of carbon steel pipes can be affected by a wide variety of factors, such as CO₂ partial pressure, temperature, pH, flow velocity, water chemistry, and pipe size and inclination [9, 27, 31, 38, 93-95]. Particularly, fluid hydrodynamics plays an important role in pipeline internal corrosion. While the rotating electrode techniques and jet impingement apparatus have been used to study CO₂ corrosion in flow conditions [96], a flow loop is able to produce fluid hydrodynamic conditions that are better representative of those encountered in the pipeline.

When a flow loop was used for internal corrosion studies, there has been limited work to investigate the uniformity of corrosion occurring inside the pipe, i.e., whether the steel electrodes installed at the top and the bottom of the same cross section of a pipe experience an identical corrosion. Generally, corrosion of a pipe at its top and bottom sections can be affected by many factors, such as flow condition, scale formation, etc. To date, there has not been relevant work conducted to characterize the corrosion uniformity of a flow pipe.

This work was to investigate corrosion of X65 steel specimens, which were installed at the top and the bottom of a flow pipe, respectively, in a CO₂-saturated single-phase brine water through a home-designed flow loop system. Electrochemical measurements, including open-circuit potential (OCP), electrochemical impedance spectroscopy (EIS)

* This work has been published as: Q. Li, Y.F. Cheng, Non-uniform corrosion of steel pipe in CO₂-containing fluid flow, *Materials Performance*, 55 (2016) 58-62.

and galvanic potential and current, morphological characterization and CFD simulation were combined for the purpose.

3.2 Experimental

Specimens used in this work were cut from a sheet of X65 pipeline steel, with a chemical composition (wt. %): C 0.04, Si 0.2, Mn 1.5, P 0.011, S 0.003, Mo 0.02, and Fe the balance. The specimens were machined into cylindrical shape, with a diameter of 10 mm, and welded to a copper wire on one end. The cylindrical surface of the specimen was sealed with a polytetrafluoroethylene (PTFE) tape, leaving an exposed surface area of 78.5 mm². The electrode assembly is shown in Figure 3.1. The working face of the electrode was ground sequentially up to 1000 grit silicon carbide paper, rinsed with distilled water and degreased in acetone, and then dried with a blow dryer.

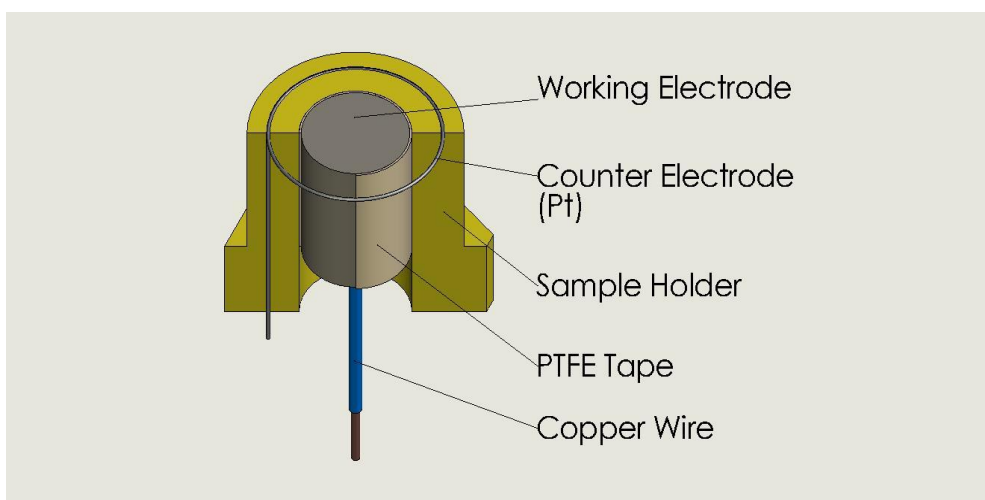


Figure 3.1 Schematic diagram of the electrode assembly.

The test solution contained 1 wt. % NaCl + 0.1 wt. % NaHCO₃ to simulate the brine water in gathering pipelines. By saturating with CO₂ gas (99.95%), the pH of the solution was brought to ~5.8.

The schematic diagram of the home-designed, lab-scaled flow loop is shown in Figure 3.2. It consisted of a centrifugal pump, reservoir, heating element, thermocouple combined with a temperature controller, cooling assembly, a supersonic flow meter, a reference electrode (RE) (saturated calomel electrode, SCE), a testing unit where two steel specimens were installed by thread at both the top and the bottom of the unit, i.e., electrode assemblies I and II, respectively, and the connecting pipe and fittings. The solution was supplied from the 4 L reservoir and circulated through the loop driven by the centrifugal pump. The flow velocity was 1 m/s. The flow velocity was measured with the supersonic flow meter. The inner diameter of the cylindrical connecting pipe was 17 mm, the testing unit has a square cross-section and its dimension was 17 mm × 17 mm. The length of the testing unit was 400 mm. The solution was heated to the testing temperature (60 ± 1 °C), and circulated in the bypass pipe path. After the electrode assemblies were installed in the testing unit, the solution flowed to the loop system. CO₂ bubbling was maintained throughout the testing.

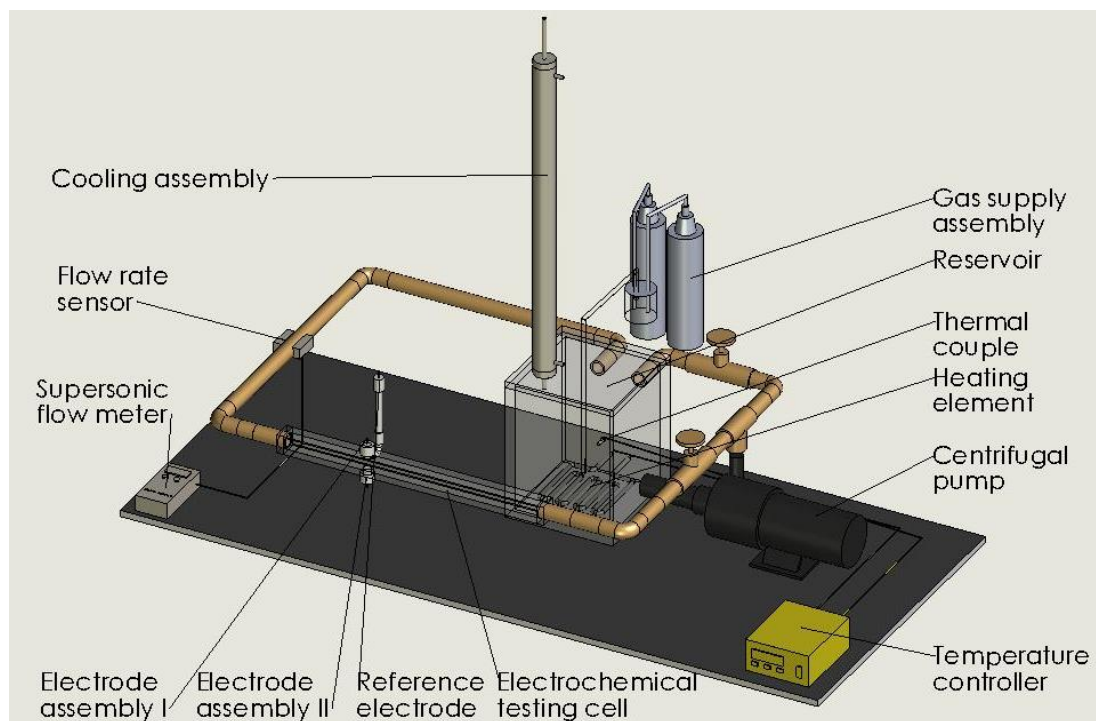


Figure 3.2 Schematic diagram of the experimental set-up of the flow loop system.

Electrochemical corrosion measurements were performed with a Gamry Reference 600 system on the three-electrode cell, where a platinum wire was used as counter electrode (CE), the SCE as RE, and the steel specimen as working electrode (WE). A steady state OCP was achieved prior to electrochemical measurements. The EIS was measured with a sinusoidal potential disturbance of 10 mV in the frequency range from 100 kHz to 0.01 or 0.05 Hz. To ensure the reproducibility of the results, each test was repeated three or more times. The galvanic potential and current between the two steel electrode assemblies as shown in Figure 3.1 were measured through a zero-resistance ammeter (ZRA). After corrosion testing, the electrodes were removed from the testing unit and immersed into deionized water to clean out soluble salts. The electrodes were

then dipped into acetone for further cleaning, dried and stored in a desiccator. The morphology of the electrode was characterized with a scanning electron microscope (SEM).

The CFD simulation was performed using a commercial software package of ANSYS 14.0 (Meshing with ICEM CFD 14.0, and simulation calculation with Fluent 14.0). Figure 3.3 shows the 3-D structure of the flow field model created according to the dimension of the testing cell installed in the flow loop. A straight, cylindrical pipe was set at both the inlet and outlet ends. The fluid was assumed as incompressible. The fluid density and viscosity was set as 983.3 kg/m^3 and $0.467 \times 10^{-3} \text{ kg/m s}$, respectively, at the operating temperature of $60 \text{ }^\circ\text{C}$. The fluid flow was in the turbulent range, and a standard $k-\varepsilon$ turbulent model was used. It was assumed that the fluid flow direction was perpendicular to the cross-sectional face of the pipe.

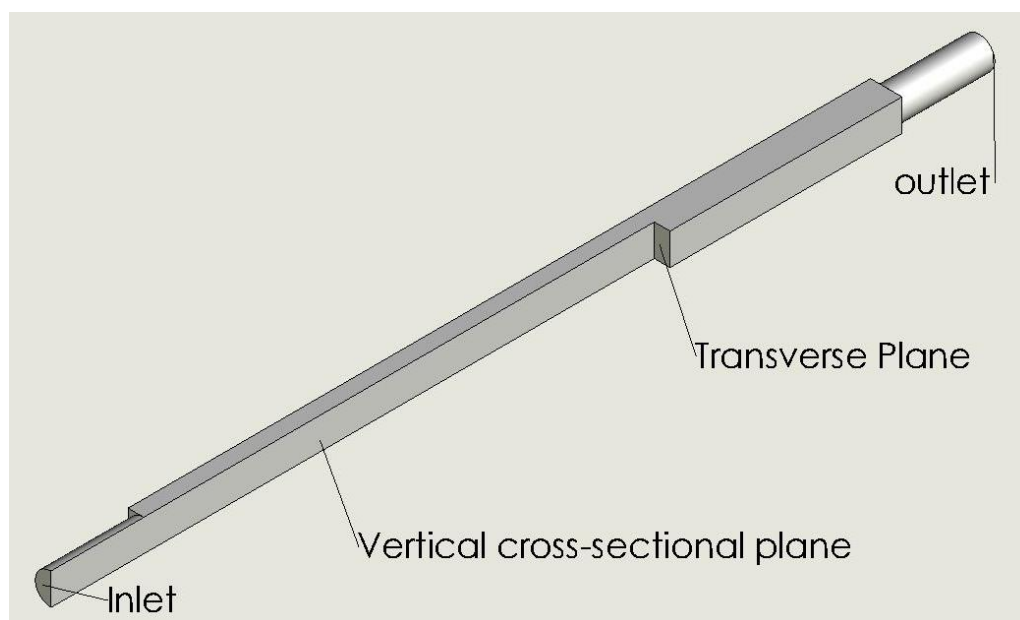


Figure 3.3 The 3-dimensional structure of the flow field model of the testing unit for CFD simulation.

3.3 Results

Figure 3.4 shows the OCP measured on the steel electrodes installed at the top and bottom of the testing unit in the solution at a flow velocity of 1 m/s. It is shown that the OCP is shifted positively with time. Moreover, the bottom electrode is always associated with the more negative OCP than that of the top one.

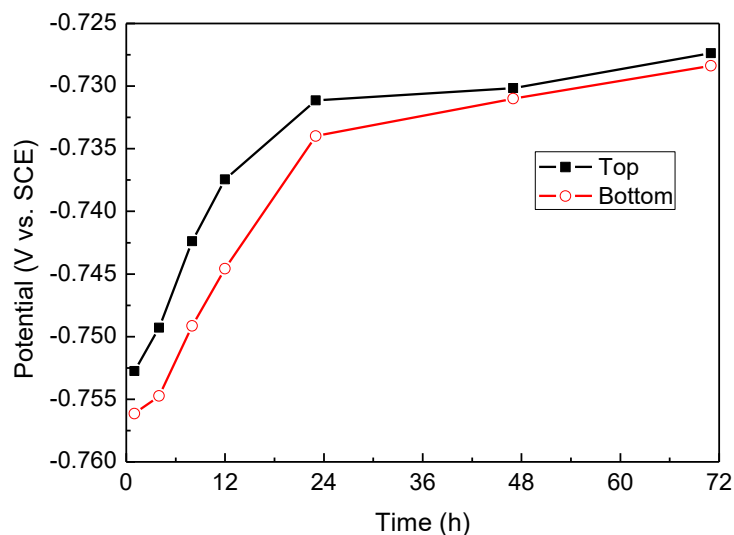


Figure 3.4 Open-circuit potentials measured on the top and bottom electrodes as a function of time.

Figure 3.5 shows the galvanic current and potential measured between the top and the bottom electrodes installed in the testing unit under the same testing condition as that in Figure 3.4. The bottom and the left axes show the galvanic current change over 3600 s period for each testing time. The top and right axes show the galvanic potential at different testing time. The potential difference refers to the potential of the bottom

electrode minus that of the top electrode. Thus, a negative potential difference means that the potential of the bottom electrode is smaller than that of the top one. Negative galvanic currents observed mean that electrons flow from the bottom electrode to the top one. The galvanic potential results indicate that the bottom electrode is more anodic and active than the top one. Furthermore, as the time increases, the galvanic potential and current decrease.

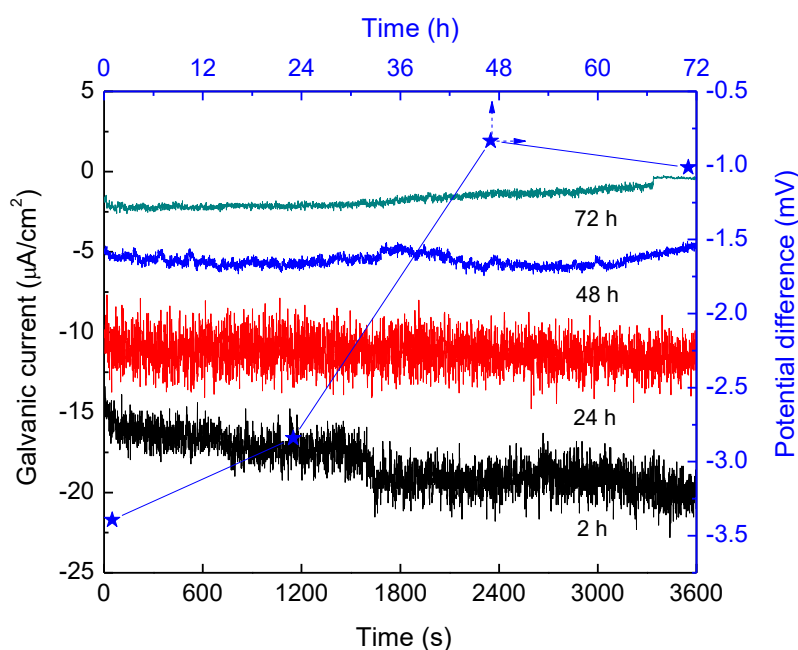


Figure 3.5 Galvanic current (curves) and potential difference (★) measured between the top and the bottom electrodes installed at the testing unit as a function of time.

Figure 3.6 shows the EIS measured on both electrodes under the same condition as that in Figure 3.4. It is shown that, for both electrodes, the impedance is featured with a semicircle over the whole frequency range, indicating that they have an identical corrosion mechanism. At individual times, the impedance semicircle measured on the top

electrode is larger than that measured on the bottom electrode. Since the size of the semicircle is proportional to the charge-transfer resistance, the top electrode has a larger charge-transfer resistance, and thus experiences a smaller corrosion rate, than the electrode at the bottom of the testing unit.

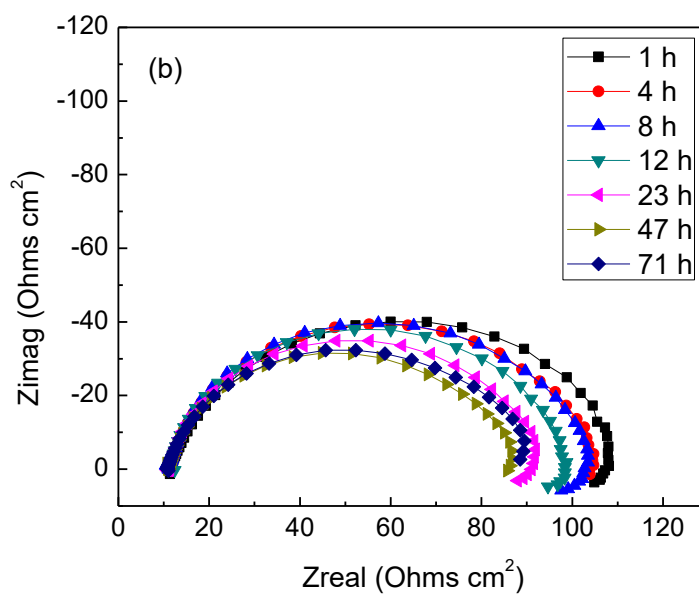
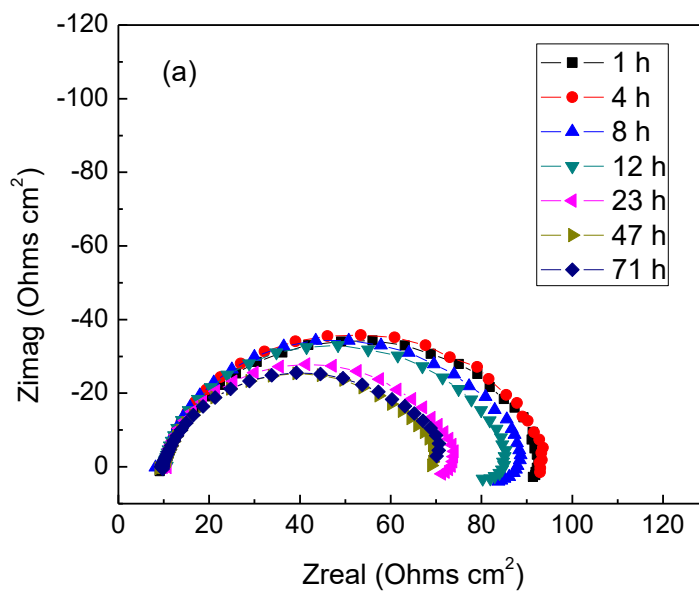
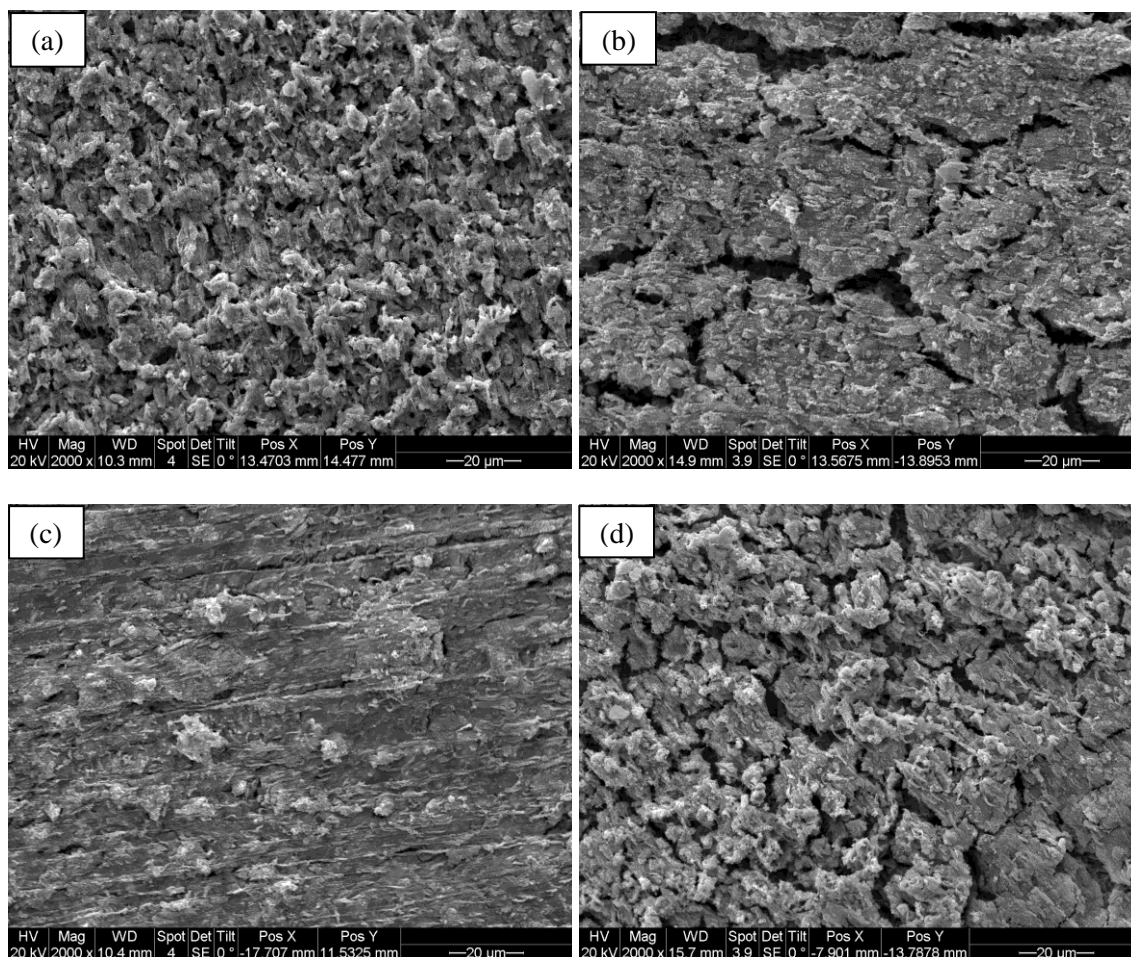


Figure 3.6 EIS measured on the bottom (a) and the top (b) electrodes as a function of time.

Figure 3.7 shows the surface morphologies of the steel electrodes installed at the top and the bottom of the testing unit as a function of time. It is seen that, generally, at individual testing times, the corrosion scales formed on the bottom electrode contain cracks, while the scales formed on the top electrode is relatively less porous. Moreover, as the time is increased, the scale formed on both electrodes become more continuous compared to those formed initially.



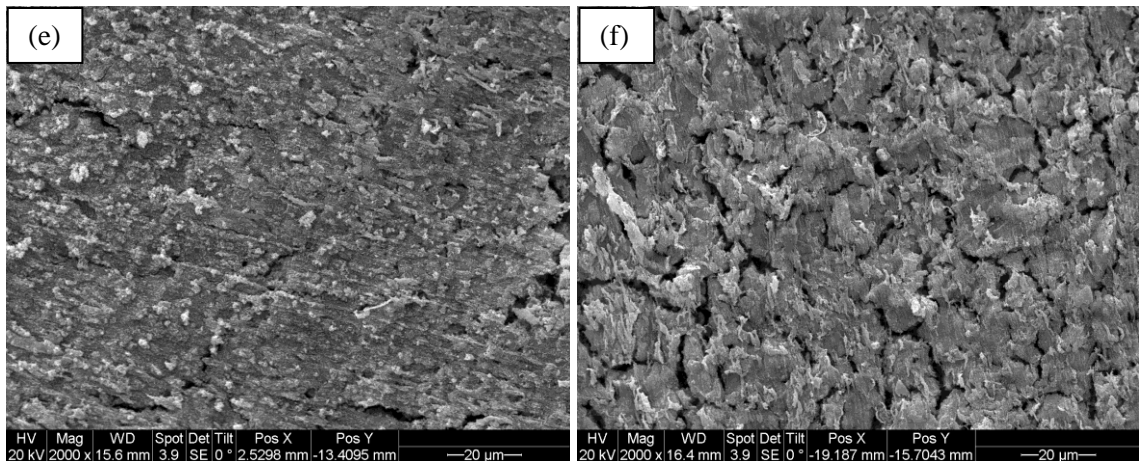


Figure 3.7 SEM images of the morphology of the electrode surface at different location and testing time: (a) Top – day1, (b) Bottom – day 1, (c) Top –day 2, (d) Bottom – day 2, (e) Top –day 3, (f) Bottom – day 3.

Figure 3.8 shows the contour of the fluid flow velocity in the testing unit at the inlet velocity of 1 m/s. It is seen that, upon fluid flowing from the cylindrical inlet to the testing unit or from the testing unit to the cylindrical outlet, a fluid disturbance occurs at the transition. However, at locations far away from the transitions, the flow regime in the testing unit is steady and continuous. Figure 3.9 shows the contour of flow velocity of the transverse plane of the testing unit where the two electrodes are located. It is seen that the distribution of the flow velocity is central symmetrical.

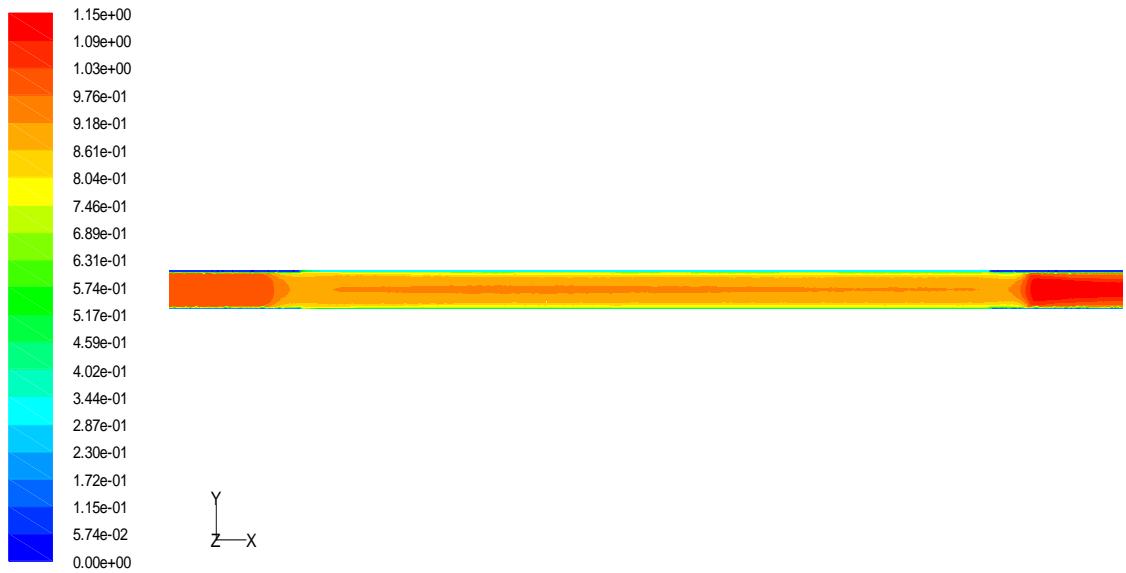


Figure 3.8 Contour of flow velocity of the vertical plane of testing cell at a flow velocity 1 m/s.

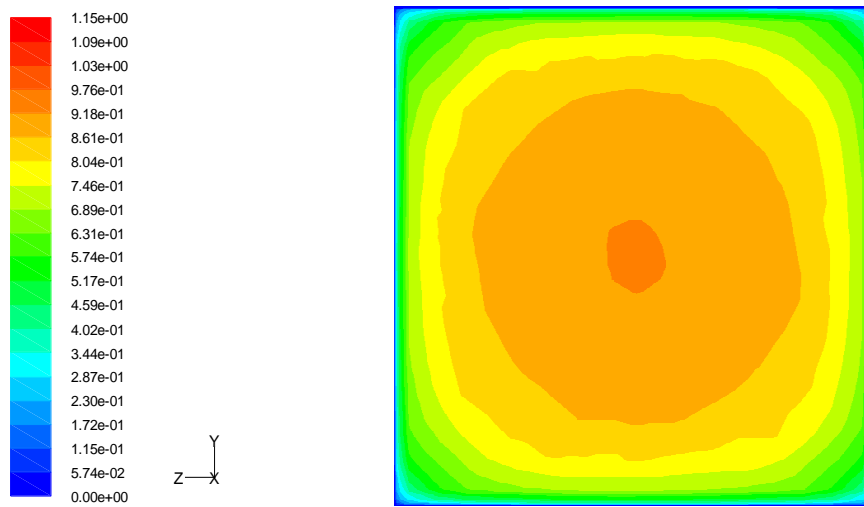


Figure 3.9 Contour of flow velocity of the transverse plane of the testing unit at a flow velocity 1 m/s.

3.4 Discussion

The CO₂ corrosion of steel pipe in the solution with pH is 5.8 is featured with the dominant cathodic reactions: reduction of carbonic acid (Eq. (2-8)), reduction of bicarbonate ions (Eq. (2-9)) and reduction of water (Eq. (2-10)) [97]. The anodic reaction is the dissolution of iron (Eq. (2-6)).

As proposed previously [95], the iron dissolution is followed by formation of FeCO₃ scale in CO₂ environments, either chemically (Eq. (2-12)) or electrochemically:



The formed scale is able to slow down corrosion of the steel by acting as a blocking layer [9]. The precipitation of the FeCO₃ scale depends on many factors, one of which is the concentration of ferrous ions in the solution. When the [Fe²⁺] in the solution is too small to meet the required solubility for FeCO₃ scale to form, the steel electrode is not sufficiently protected.

Fluid flow plays a critical role in integrity of the iron carbonate scale formed on the steel surface. It has been acknowledged that fluid flow is able to thin and damage the surface film [38]. The morphological observation of the scale in Figure 3.7 demonstrates that the scale is not sufficiently compact and contains cracks. Thus, the formed scale under the testing condition is not protective. As seen in EIS measurements in Figure 3.6, the impedance semicircle reduces in size with time, indicating the increased corrosion rate of steel electrode under fluid flow.

The OCP measurements indicate that the steel electrodes installed at the top and the bottom of the testing unit in flow pipe have certain potential differences (Figure 3.4), indicating that the electrodes have different electrochemical activities. This is further demonstrated by the galvanic potential and current measurements in Figure 3.5. Both galvanic potential and current measurements show that the bottom electrode is more active than the top one. Thus, the pipe bottom would experience enhanced corrosion compared to the top, as indicated by the impedance measurement results in Figure 3.6.

The non-uniform corrosion activity between the top and bottom of the flow pipe can be attributed to the different structures of iron carbonate scale formed on the pipe surfaces. It is seen from Figure 3.7 that the scale formed at the pipe bottom contains more and wider cracks, and are more porous than that formed at the top of the pipe. As a result, the bottom part of the pipe is more electrochemically active than the top part which is covered by a relatively more continuous scale.

This work shows that the fluid dynamics does not contribute to the corrosion non-uniformity. The CFD simulation shows that the top and the bottom of the flow pipe experience an identical flow condition in the single-phase fluid flow. Thus, the structural difference of the scale formed at the top and bottom of the pipe is not due to the fluid dynamic factor.

The hydrostatic pressure in the flow pipe might play a role in affecting the scale formation. Under fluid flow, the dynamic pressure on both top and bottom electrodes is identical. However, the hydrostatic pressure exerted on them can be different, where the electrode at the bottom is under pressure from the fluid while the electrode at the top is

not. According to Eq. (3-2) [98], the hydrostatic pressure on the bottom electrode is 163.8 Pa larger than that on the top electrode.

$$p = \rho gh \quad (3-2)$$

where p is the hydrostatic pressure (Pa), ρ is the density of the fluid (983.3 kg/m³), g is the gravity acceleration rate (9.8 N/kg), and h is the height of water, i.e., the height of the testing unit in the pipe (17 mm).

It has been accepted [99-101] that the hydrostatic pressure can affect corrosion of metals. Sun et al. [99] investigated the corrosion behavior of a high-strength low-alloy steel in 3.5% NaCl solution under hydrostatic pressures. It was found that a high pressure accelerated the corrosion process remarkably. Beccaria et al. [100, 101] found that the susceptibility to pitting of aluminium and nickel can be increased with increasing hydrostatic pressure. The effect of hydrostatic pressure on the integrity of corrosion scale is being studied in the authors' lab. The detailed mechanism of how hydrostatic pressure affects the corrosion rate and corrosion scale will be reported in the further work.

3.5 Summary

The steel electrodes installed at the top and the bottom of a flow pipe possess different corrosion activities in CO₂-containing environments. The steel electrode at the pipe bottom is more active than the one installed at the pipe top. Thus, the flow pipe experiences a non-uniform corrosion between its top and bottom parts in a single-phase fluid flow.

While fluid flow could degrade the integrity of iron carbonate scale formed on the steel surface, the fluid dynamics does not contribute to the corrosion non-uniformity. The electrodes installed at the top and bottom of the pipe experience identical fluid conditions and mechanics. The larger corrosion activity of the bottom electrode can be attributed to the higher hydrostatic pressure compared to the top electrode.

Chapter Four: Corrosion of pipelines in CO₂-saturated oil-water emulsion flow *

4.1 Introduction

For internal corrosion of pipelines made of carbon steels in upstream oil gathering systems, the presence of oily phase in the fluid remarkably affects the flow regime [41, 71], thus making the corrosion more complex. Maintenance of the pipe steel by oil-wetting, which can inhibit corrosion of the steel, depends on a number of factors, such as the ratio of the amount of oil to that of water, flow velocity, temperature, pipe size, pipe inclination, etc. [41]. The corrosion behavior of pipelines in CO₂-containing oil-water emulsion flow has so far not been fully understood.

A flow loop is able to produce fluid hydrodynamic conditions that are representative of those encountered in pipelines, such as wall shear stress and fluid flow patterns. By virtue of CFD simulation, the flow loop provides an ideal alternative to investigate the fluid flow in pipelines and its effect on steel corrosion [102].

In this work, the corrosion of an X65 pipeline steel in CO₂-saturated oil-free solutions and oil-water emulsions was investigated using a home-made pipe flow system. Electrochemical measurements, including EIS and potentiodynamic polarization curves, were conducted to determine the corrosion mechanism and rates under various conditions. Parametric effects, such as flow velocity, temperature and the content of oil in the fluid, were determined. The CFD simulation was performed to understand the distribution of oil in the fluid and to derive relevant parameters, which were used by a

* This work has been published as: Q. Li, H. Hu, Y.F. Cheng, Corrosion of pipelines in CO₂-saturated oil-water emulsion flow studied by electrochemical measurements and computational fluid dynamics modeling, *Journal of Petroleum Science and Engineering*, 147 (2016) 408-415.

semi-empirical model to predict CO₂ corrosion rate of the pipeline in oil-water emulsions.

4.2 Methodology

4.2.1 Electrode and solution

Specimens used in this work were cut from a sheet of X65 pipeline steel, with a chemical composition (wt. %): C 0.04%, Si 0.2%, Mn 1.5%, P 0.011%, S 0.003%, Mo 0.02% and Fe the balance. The specimens were machined into cylindrical shape, with a diameter of 1.000 cm and the working surface area of 0.785 cm². The specimens were welded to a copper wire, and sealed into a sample holder with epoxy resin. The working face was ground consequentially up to 1,000 grit silicon carbide paper, rinsed with distilled water, degreased in acetone, and then dried with a blow dryer.

The test solution was made of analytical grade reagents and deionized water. The chemical composition of the base solution was 1 wt. % NaCl solution. Varied contents of heavy paraffin oil, with a density of 0.830 g/cm³, were added to prepare oil-water emulsions with the aid of trace amount of a surfactant. The viscosity of the oil at 35 °C, 45 °C, 60 °C and 75 °C were 59.0 cSt, 30.2 cSt, 21.8 cSt and 14.3 cSt, respectively. The base emulsion contained 10 wt. % oil. High-purity CO₂ (99.95%) was purged into the solution and emulsion continuously. The pH values of the base oil-free solution and oil-containing emulsion at 45 °C were 4.00 and 4.09, respectively.

4.2.2 Flow loop system

A home-made flow loop system, as shown in Figure 4.1, was used in this work. It consisted of a centrifugal pump, a reservoir, a heating unit, a thermocouple combined with a temperature controller, a cooling assembly, a supersonic flow meter combined with a sensor, an electrochemical testing cell where a WE, a CE and a RE were installed, pipes and two valves. The test solution/emulsion was contained in a 4 L reservoir, and circulated through the pipe driven by the centrifugal pump. The fluid flow velocity was controlled by adjusting valves, and measured at the cylindrical pipe with the supersonic flow meter. The inner diameter of the pipe was 17 mm, and the cross dimension of the electrochemical testing cell was 17 mm × 17 mm, and the length of the cell was 400 mm.

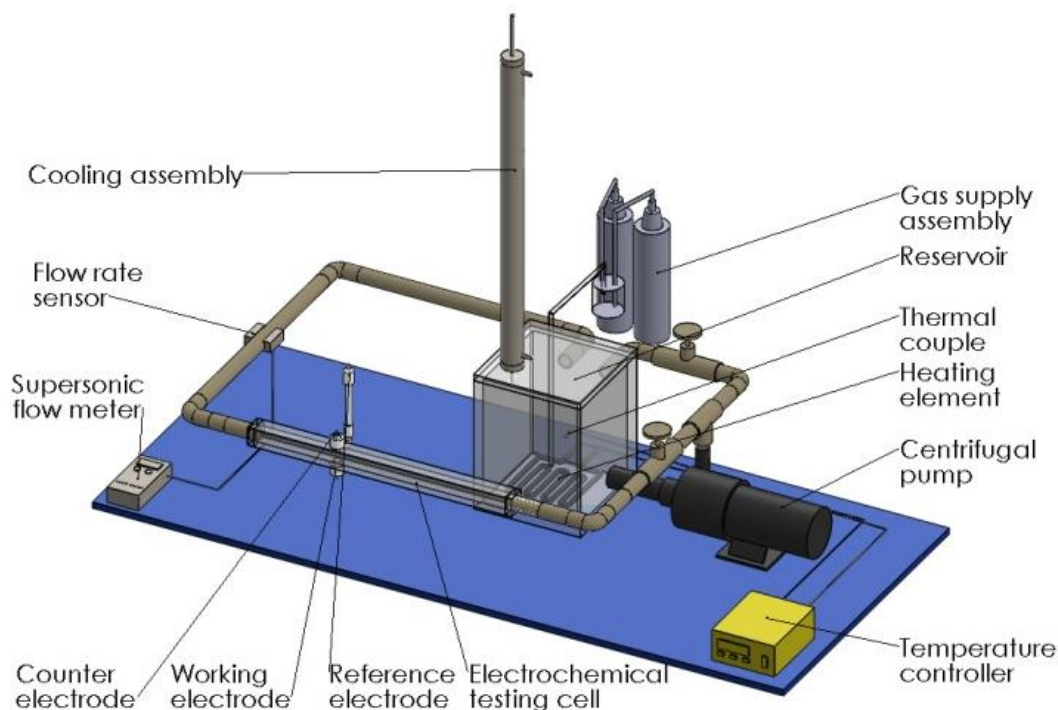


Figure 4.1 Schematic diagram of the home-made flow loop system.

4.2.3 Experimental setup and electrochemical measurements

The solution/emulsion was purged with CO₂ at least 1 h prior to testing, and was then heated to the testing temperature, and circulated in the bypass pipe. The three electrodes were installed in the testing unit and assembled in the loop system. The CO₂ purging was maintained throughout the test.

Electrochemical measurements were performed on the three-electrode testing unit with a Gamry Reference 600 system, where the steel specimen was used as WE, a carbon rod as CE and a SCE as RE. The OCP of the steel working electrode was monitored until it achieved a steady state. The EIS was measured with a sinusoidal disturbance potential of 10 mV in the frequency range from 100 kHz to 50 mHz. The steel electrode was maintained at its corrosion potential (E_{corr}). After the EIS measurement was finished, potentiodynamic polarization curves were measured immediately by scanning the potential from -600 mV to +600 mV relative to E_{corr} at a potential sweep rate of 0.5 mV/s.

4.3 CFD simulation and model development

4.3.1 CFD simulation settings

An ICEM CFD 15.0 module was used to construct the flow field model and do the meshing. Figure 4.2 shows the portion of a 3-dimensional meshed structure of the fluid flow in the electrochemical testing unit. A straight cylindrical pipe was set at both the upstream and downstream of the unit to help maintain a fully developed and stable flow condition. The tetrahedral mesh was used.

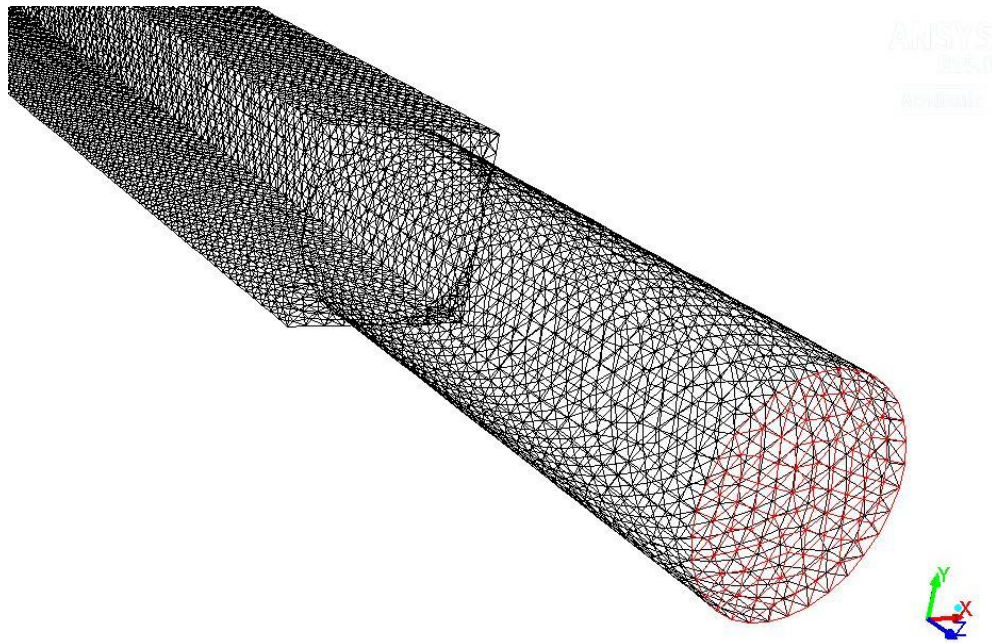


Figure 4.2 A portion of 3-dimensional meshed structure of the fluid flow in the electrochemical testing unit.

In CFD simulation, the fluid was assumed to be incompressible. The effect of temperature fluctuations on fluid flow was negligible under an isothermal condition. Phase changes were not included in this work, and there was no mass transfer between the phases.

At the pipe inlet, the velocity inlet boundary condition was used to define the actual velocity of the fluid. At the outlet of the pipe, the pressure outlet boundary condition was used. The wall boundary condition was used to bind the fluid and the solid region.

The CFD simulation and analysis was carried out using Fluent 15.0, where the standard k -epsilon turbulent model was used. Due to the relative simplicity of the loop geometry, standard wall functions were selected. It was assumed that the fluid was

stagnant at the wall of the pipe, and there was no slip boundary condition at the wall. The pipe wall roughness was set as 0.5. There were two phases, i.e., oil and water, contained in the fluid. A volume of fluid (VOF) model was used to simulate the two-phase fluid flow, where phase 1 was oil and phase 2 was water.

Under-relaxation factors, including momentum, volume fraction, turbulent kinetic energy and turbulent dissipation rate, were set as 0.3. A second order upwind discretization scheme was used for calculations of momentum equation, volume fraction, turbulent kinetic energy and turbulent dissipation rate. The convergence criterion was based on the residual value of the calculated variables including momentum, energy, mass, etc. The simulation was time dependent (transient), which was featured with 400 steps, 0.05 step size, and 100 iterations at each step size.

4.3.2 Corrosion model description

To accurately predict the corrosion rate of the steel under oil-water flow conditions, various parameters were included as inputs. These included temperature, CO₂ partial pressure, flow velocity, oil content, etc. The corrosion rate, CR (mm/year), was calculated by [17]:

$$CR = 31.15 \left(\frac{\Delta P}{L} \right)^{0.3} V^{0.6} P_{CO_2}^{0.8} T e^{\left(\frac{-2671}{T} \right)} \quad (4-1)$$

where $\Delta P/L$ is the pressure drop gradient, N/m³; V is the water cut; P_{CO_2} is the carbon dioxide partial pressure, MPa; and T is temperature, K. The method in Eq. (4-1) is able to

predict corrosion rate of steels for low viscosity oils, with carbon dioxide partial pressures up to 0.79 MPa and temperatures up to 90 °C. For corrosion prediction in this work, the flow-related variable, i.e., the pressure drop gradient, was determined by the CFD simulation.

4.4 Results

4.4.1 Polarization curve measurements

Figure 4.3 shows the potentiodynamic polarization curves of X65 steel in CO₂-saturated oil-free base solution and base oil-water emulsion, respectively, at 45 °C and various fluid flow rates. A diffusive limiting current density is observed for all measured cathodic curves over a certain potential range, and increases with the increasing flow velocity. This indicates that mass-transfer plays a big role in the cathodic process during corrosion of the steel in the system. The anodic curves almost copy each other at various fluid flow velocities. When the cathodic potential is sufficiently negative, e.g., more negative than -1 V (SCE), the diffusive current phenomenon disappears, and the cathodic curves become independent of the flow velocity. Furthermore, the slope of the diffusive limiting cathodic current density increases with the flow velocity.

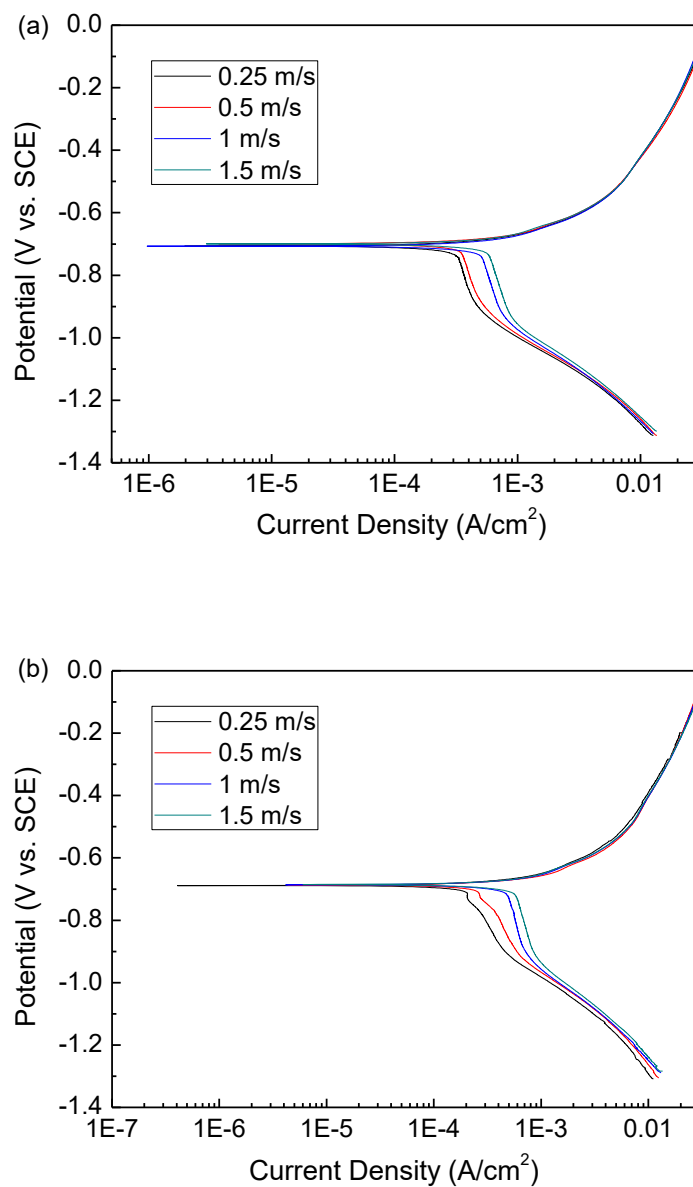
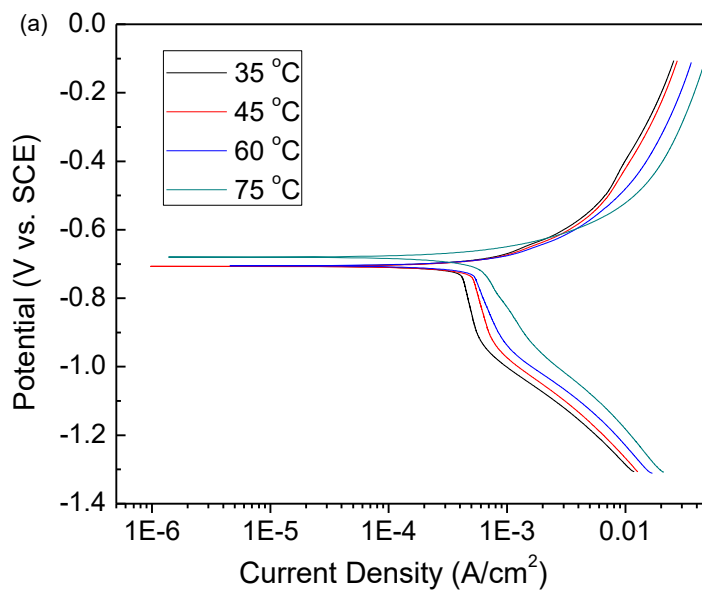


Figure 4.3 Potentiodynamic polarization curves of X65 steel in CO₂-saturated oil-free solution (a) and oil-water emulsion (b), respectively, at 45 °C at various fluid flow rates.

Figure 4.4 shows the polarization curves of X65 steel in CO₂-saturated base oil-free solution and base oil-water emulsion, respectively, at the flow velocity of 1 m/s and various temperatures. It is seen that both the anodic and cathodic current densities increase with temperature in the absence and presence of oil in the solution. With the increasing temperature, the slope of the diffusive limiting cathodic current density decreases. At 75 °C, a diffusive current density is not observed in the cathodic curves.



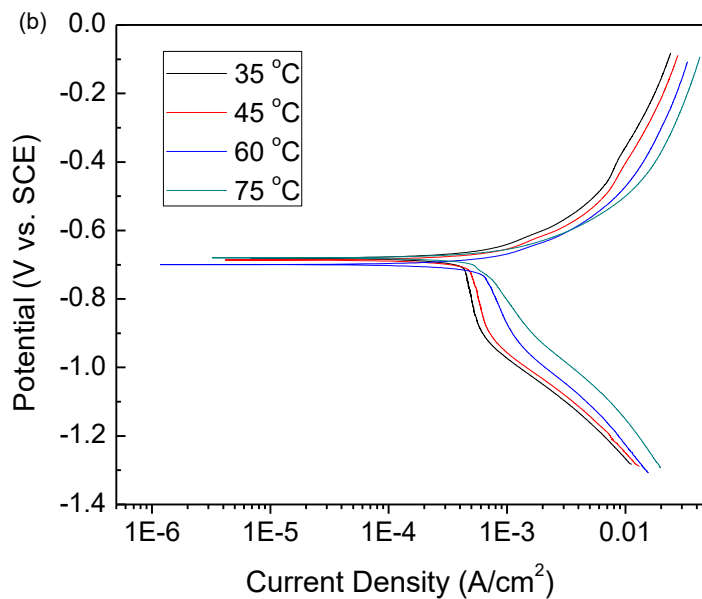


Figure 4.4 Polarization curves of X65 steel in CO₂-saturated oil-free base solution and base oil-water emulsion, respectively, at flow velocity of 1 m/s and various temperatures.

Figure 4.5 shows the polarization curves of X65 steel in CO₂-saturated solutions at 45 °C and flow velocity of 1 m/s, but with various oil contents. It is seen that, with the increase of the oil concentration in the fluid, both the cathodic and anodic current densities decrease.

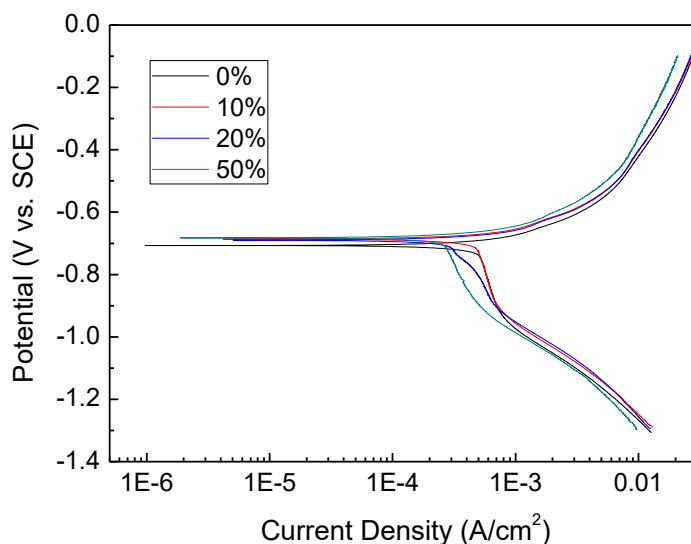


Figure 4.5 Polarization curves of X65 steel in CO₂-saturated solutions at 45 °C and flow velocity of 1 m/s, but with various oil contents.

4.4.2 EIS measurements

Figure 4.6 shows the Nyquist diagrams of X65 steel in CO₂-saturated base oil-free solution and base oil-water emulsion, respectively, at 45 °C and various fluid flow rates. It is seen that all impedance plots are featured with a capacitive semicircle in the high frequency range and an inductive loop in the low frequency range. With the increase in flow velocity, the size of the semicircle becomes smaller.

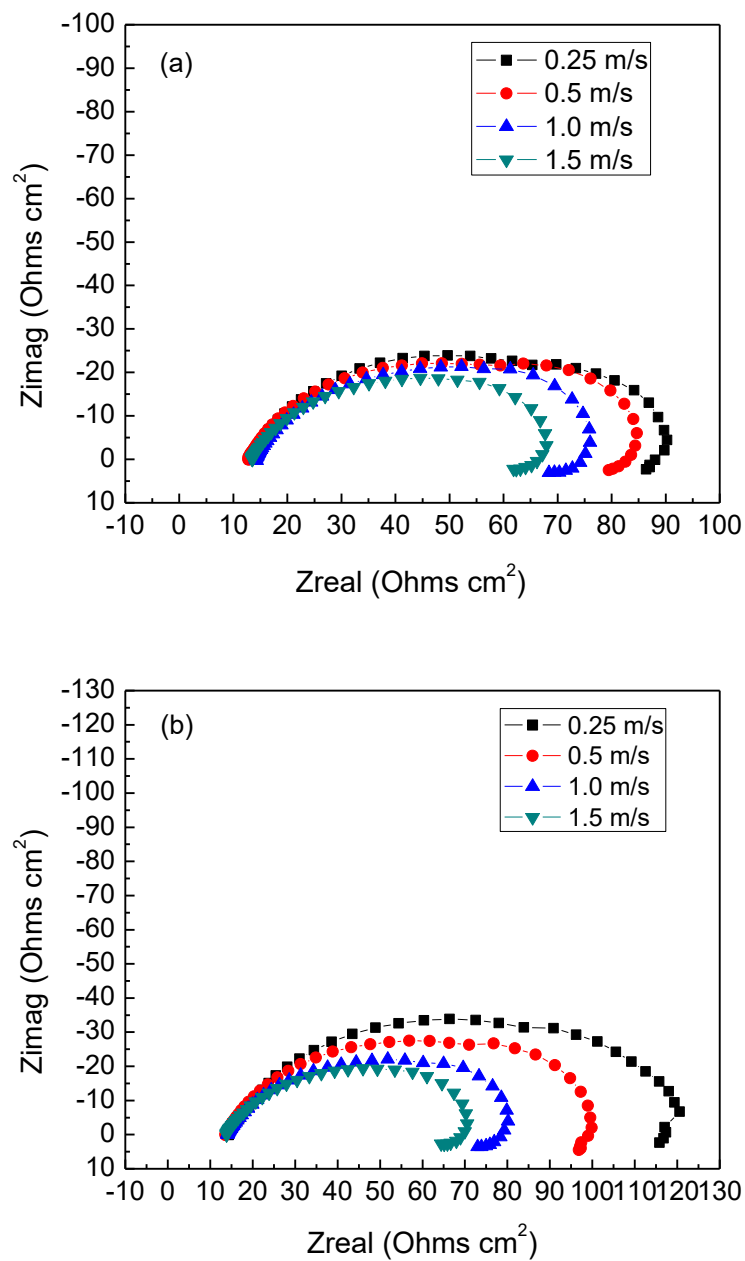


Figure 4.6 Nyquist diagrams of X65 steel in CO_2 -saturated oil-free solution (a) and oil-water emulsion (b), respectively, at 45 °C at various fluid flow rates.

Figure 4.7 shows the Nyquist diagrams of X65 steel in CO₂-saturated base oil-free solution and base oil-water emulsion, respectively, at flow velocity of 1 m/s and various temperatures. The impedance feature is same as that in Figure 4.6, and the size of semicircle is reduced with the increasing temperature.

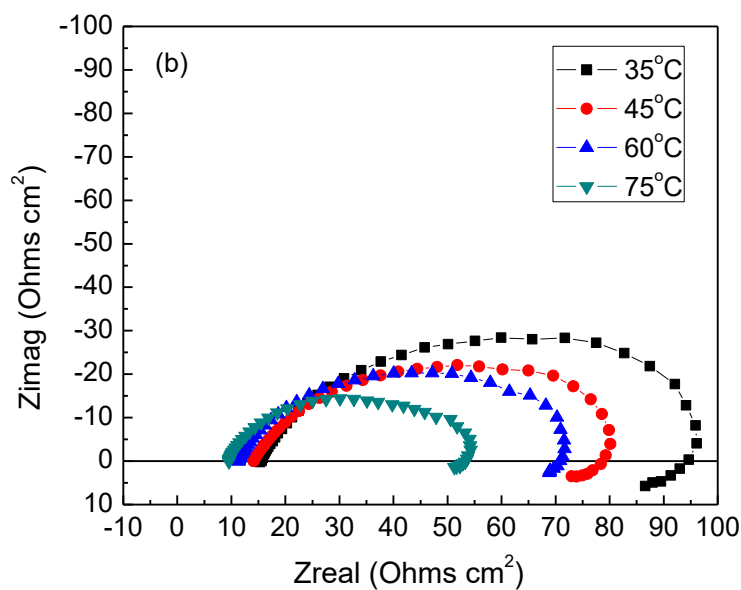
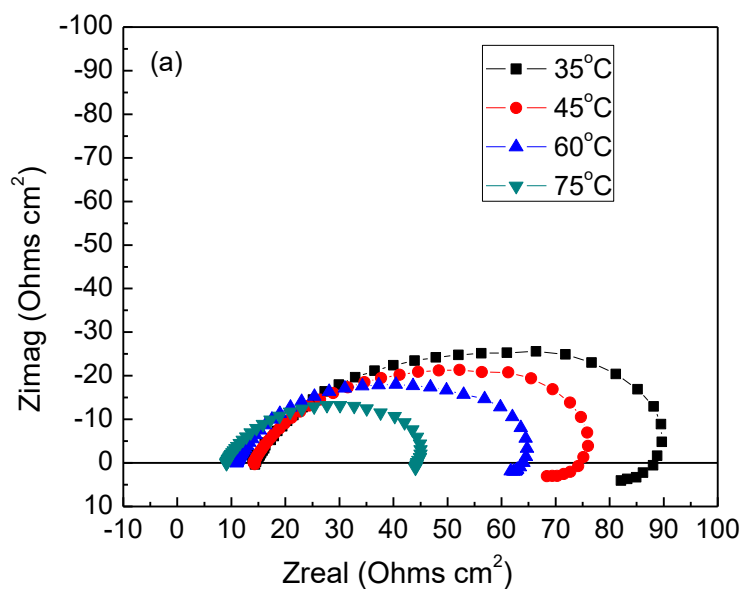


Figure 4.7 Nyquist diagrams of X65 steel in CO₂-saturated oil-free solution (a) and oil-water emulsion (b), respectively, at flow velocity of 1 m/s and various temperatures.

Figure 4.8 shows the Nyquist diagrams of X65 steel in CO₂-saturated solutions at 45 °C and flow velocity of 1 m/s, but with various oil contents. Again, the impedance keeps unchanged. The size of the semicircle increases with the increasing oil content.

The electrochemical equivalent circuit shown in Figure 4.9 is used to fit the impedance parameters, and the results are shown in Table 4.1, where R_s is the solution resistance, CPE is the constant phase element, R_p is the charge transfer resistance, R_L is the inductive resistance, and L is the inductance.

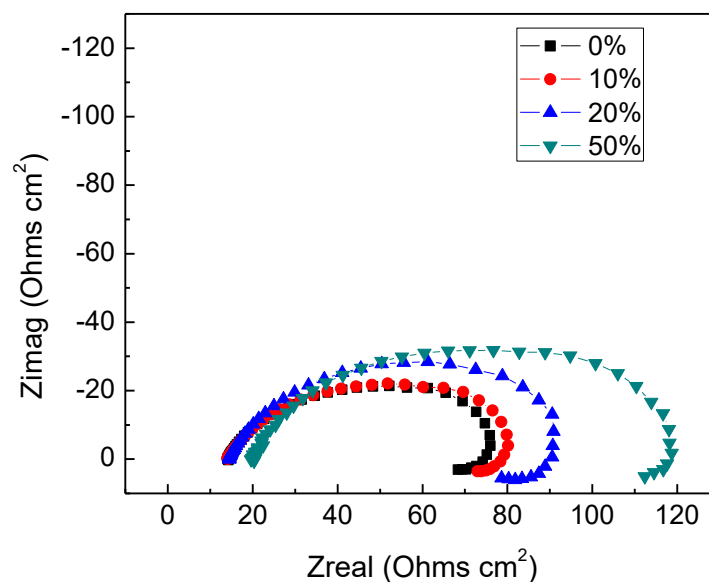


Figure 4.8 Nyquist diagrams of X65 steel in CO₂-saturated solutions at 45 °C and flow velocity of 1 m/s but with various oil contents.

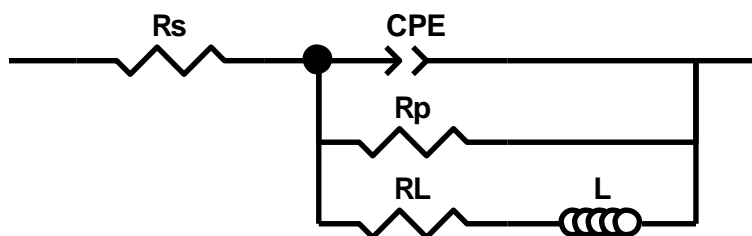


Figure 4.9 Electrochemical equivalent circuit for impedance data fitting, where R_s is the solution resistance, CPE is the constant phase element, R_p is the charge transfer resistance, R_L is the inductive resistance, and L is the inductance.

4.4.3 CFD simulation

Figure 4.10 shows the simulated distribution of oil in oil-water emulsion with various oil contents at flow velocity of 1 m/s and 45 °C. Obviously, in the absence of oil in the fluid, the steel wall surface is totally water-wetted. With the increasing oil content, the oily phase occupies more space in the pipe flow, and the pipe wall becomes intermittently oil-wetted. The oil-wetting opportunity increases with the increase in oil content in the emulsion.

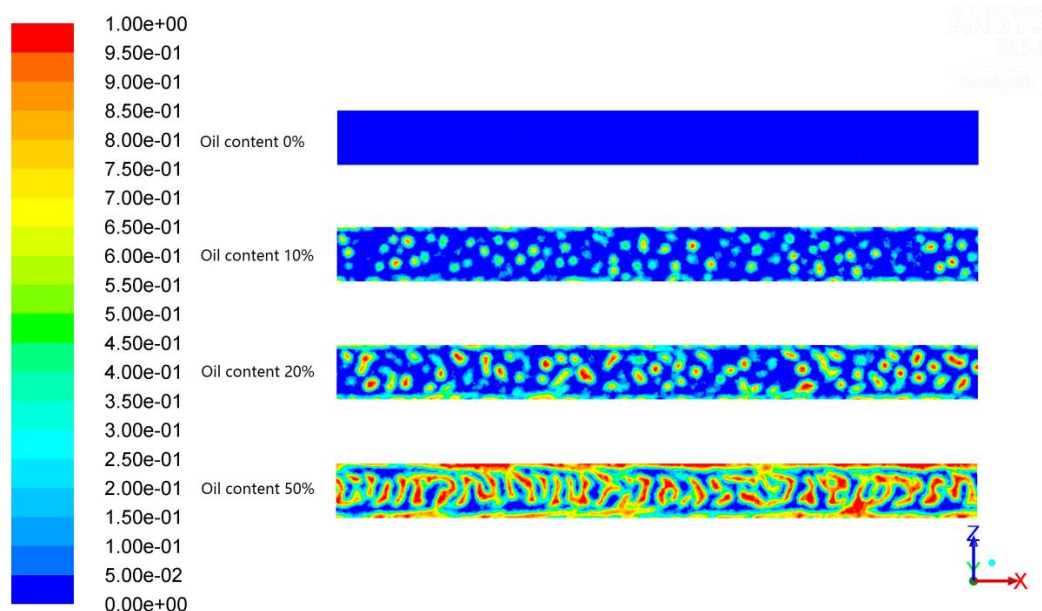


Figure 4.10 CFD simulated distribution of oil in oil-water emulsion with various oil contents at flow velocity of 1 m/s and 45 °C.

4.5 Discussion

4.5.1 CO₂ corrosion of pipelines in oil-free fluid flow

The CO₂ corrosion reactions of a carbon steel depend on the solution pH and temperature [95]. In this work, the CO₂ saturated solutions have a pH of about 4.00 and 4.43 at 45 °C and 75 °C, respectively. The dominant cathodic reactions are the reduction of hydrogen ions (Eq. (2-7)) and carbonic acid (Eq. (2-8)), and the anodic reaction is the oxidation of iron (Eq. (2-6)).

The anodic reaction can occur by multiple steps, with intermediate products such as FeOH_{ads} adsorbed on the steel surface, which contributes to the formation of an inductive loop in Nyquist diagrams [38]. Moreover, the FeCO₃ scale can form and precipitate on

the steel when the product of $[\text{Fe}^{2+}] \times [\text{CO}_3^{2-}]$ exceeds the solubility of iron carbonate.

The FeCO_3 scale can slow down corrosion of the steel by acting as a diffusion barrier to the corrosive species.

This work demonstrates that the mass transfer of reactive species, such as H^+ and H_2CO_3 , across the solution boundary layer towards the steel surface is important in the cathodic process. As the increasing fluid flow can reduce the thickness of the solution boundary layer, the diffusive limiting current density, which is inversely proportional to the thickness, increases, as shown in Figure 4.3. The accelerated cathodic process contributes to increased corrosion rate of the steel, as confirmed by the reduced charge-transfer resistance in impedance measurements, as seen in Figure 4.6 and Table 4.1.

Table 4.1 Electrochemical parameters fitted from the measured impedance data.

Velocity (m/s)	Temperature (°C)	Oil content (%)	R_s ($\Omega \text{ cm}^2$)	CPE ($\Omega^{-1} \text{ cm}^{-2} \text{ s}^{-n}$)	R_p ($\Omega \text{ cm}^2$)	R_L ($\Omega \text{ cm}^2$)	L (H cm^{-2})
0.25	45	0	12.81	2.0E-03	65.55	15.75	69.21
0.5	45	0	12.49	2.4E-03	62.52	15.94	46.52
1.0	45	0	13.97	2.9E-03	53.38	19.29	25.14
1.5	45	0	13.28	3.1E-03	47.74	15.78	20.12
1.0	35	0	14.24	2.7E-03	54.84	31.64	84.12
1.0	60	0	10.85	2.2E-03	48.47	10.68	15.69
1.0	75	0	9.016	3.5E-03	34.53	6.448	6.285
0.25	45	10	14.13	1.6E-03	92.59	18.96	91.77
0.5	45	10	13.37	1.9E-03	71.92	22.11	69.3
1.0	45	10	13.85	2.7E-03	57.28	20.24	27.97
1.5	45	10	13.57	3.2E-03	49.6	18.19	22.58
1.0	35	10	15.17	2.6E-03	57.95	26.58	42.89
1.0	60	10	11.12	1.8E-03	54.98	11.94	15.35
1.0	75	10	9.287	1.7E-03	40.93	5.799	12.17
1.0	45	20	14.26	1.9E-03	63.21	26.4	29.21
1.0	45	50	19.84	1.8E-03	81.44	25.75	93.57

Generally, an elevated temperature increases the corrosion reaction kinetics. At the same time, the iron carbonate scale is prone to form at high temperatures, which results in decreased corrosion rate. The present work shows that, at low solution pH, such as the pH smaller than 5, the increased corrosion kinetics, rather than the scale formation, dominates the temperature effect. As shown in Figures 4.4 and 4.7 and Table 4.1, as the temperature is elevated, the anodic current density increases and the charge-transfer resistance reduces, indicating the increasing corrosion rate. Moreover, the anodic polarization curves in Figure 4.4 indicate that the steel shows an active dissolution state in the solution. This also eliminates the possibility of the scale formation on the steel surface. At high temperatures, the diffusivity of reactive species, i.e., H^+ and H_2CO_3 , increases, resulting in increased limiting current densities as shown in Figure 4.4.

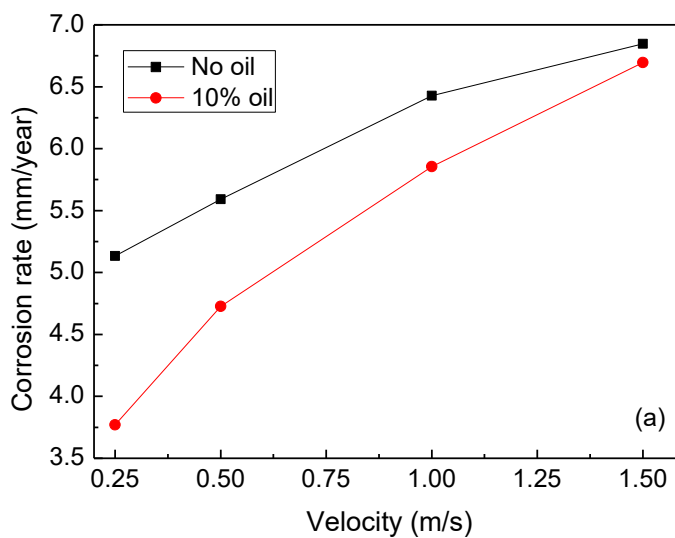
4.5.2 Corrosion of steel pipe in oil-water emulsions

The similar polarization and impedance features measured in oil-water emulsions in this work show that the presence of oil in fluid flow does not affect the corrosion mechanism of the steel. The impedance results in Table 4.1 show that the increasing oil content in the fluid would increase the charge-transfer resistance, i.e., reduce the corrosion rate of the steel. The results are consistent with the previous work [38].

As simulated in Figure 4.10 for the flow pattern in oil-water emulsions, the presence of oil increases the chance of oil-wetting of the pipe wall, serving as a physical barrier to isolate the steel from the corrosive environment. Under fluid flow, the oil wetting can be reduced due to increasing chances of oil-in-water, i.e., the chance of the water-wetting of

the steel pipe increases. Moreover, an elevated temperature could cause the partial or even complete removal of the oil layer from the pipe wall surface.

The corrosion rates of the steel in oil-free solution and 10% oil-water emulsion as a function of flow velocities and temperatures, as well as the dependence of the corrosion rates on the oil contents in oil-water emulsion are shown in Figure 4.11. Clearly, the presence of oil in the fluid reduces the corrosion rate of the steel. Moreover, the corrosion rate decreases with the increasing oil content. However, the increasing flow velocity and temperature can increase the corrosion rate.



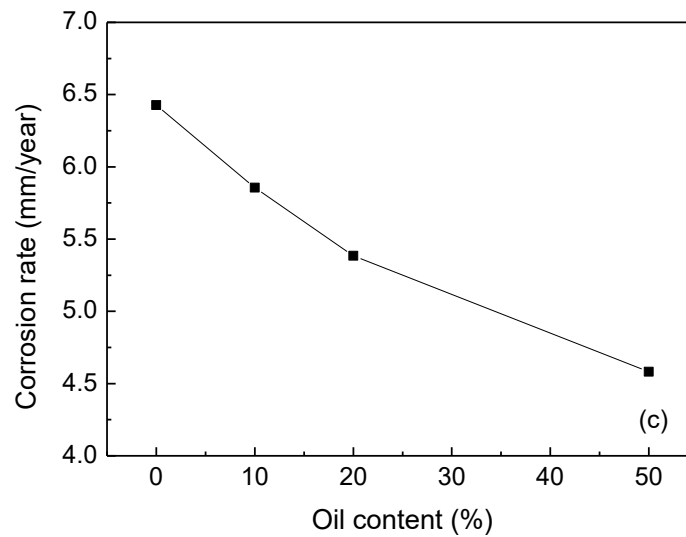
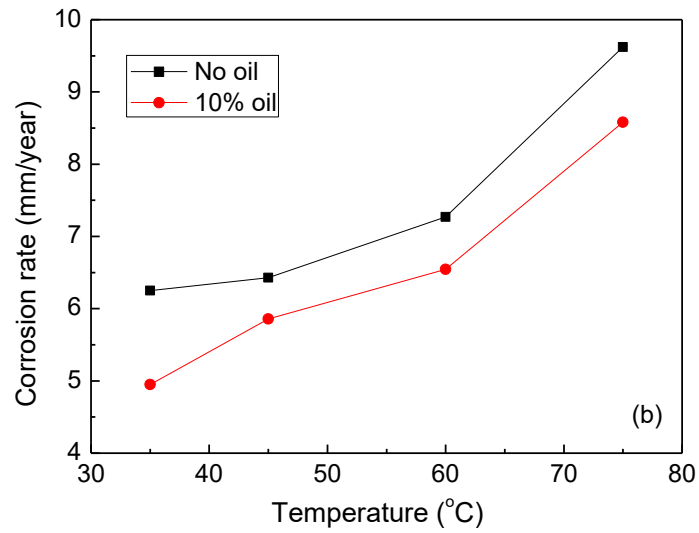


Figure 4.11 Corrosion rates of the steel in oil-free and 10% oil-water emulsion as a function of flow velocity (a) and temperature (b), as well as the dependence of corrosion rate on the oil content (c) in oil-water emulsions.

4.5.3 Corrosion prediction model and modelling validation

With the CFD simulation conducted on the flow loop, the pressure drop gradient on the steel electrode can be determined. Table 4.2 shows the pressure drop gradient obtained under various testing conditions in this work. Take the determined pressure drop gradients and relevant testing parameters into Eq. (4-1), the corrosion rate of the steel can be calculated. Figure 4.12 shows the comparison of the modelling corrosion rates with the results obtained from experimental testing. It is seen that the modelling results are relatively consistent with the testing results, indicating the reliability of the semi-empirical equation in combination with the CFD modelling for corrosion prediction. The slight difference between them is probably due to the fact that there are different properties of the oil used in this work from that used in the reference [103].

Table 4.2 Pressure drop gradient determined by CFD modelling for various flow conditions.

Velocity (m/s)	Temperature (°C)	Oil content (%)	Pressure drop gradient (N/m ³)
0.25	45	0	231
0.5	45	0	454
1.0	45	0	2026
1.5	45	0	4605
1.0	35	0	2689
1.0	60	0	1355
1.0	75	0	1162
0.25	45	10	476
0.5	45	10	2064
1.0	45	10	4914
1.5	45	10	9784
1.0	35	10	6875
1.0	60	10	1990
1.0	75	10	1213
1.0	45	20	5552
1.0	45	50	6756

It is noted that a universal model that can be applicable to all conditions for corrosion prediction does not exist. The method in Eq. (4-1) is a kind of semi-empirical model, with a certain applicability in terms of the corrosive environments and operating conditions. It is of great importance that this work proves the feasibility of CFD modelling and derivation of operating parameters that can be used for corrosion prediction.

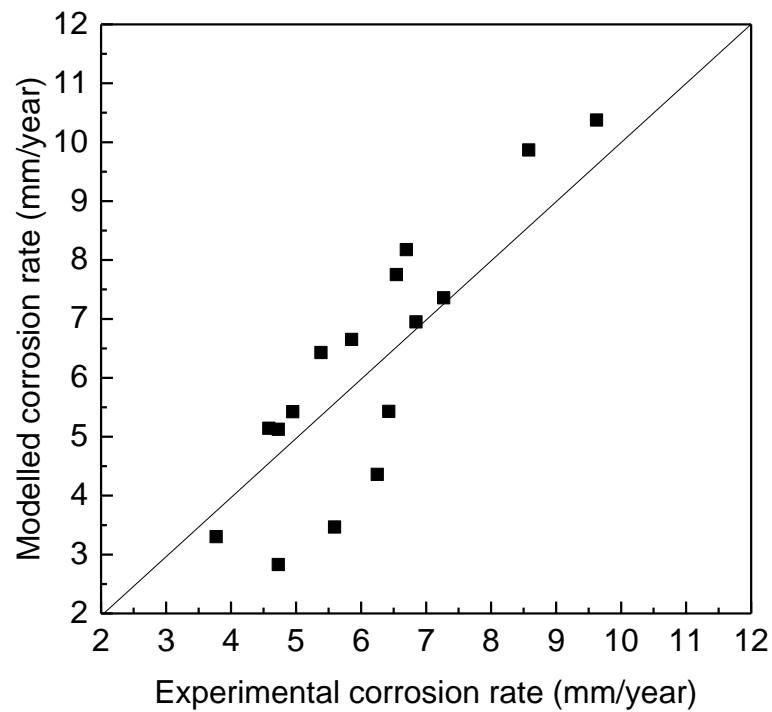


Figure 4.12 Comparison of the modelled corrosion rate with that obtained from the experimental testing.

4.6 Summary

In CO₂-saturated fluid flow, which is either the oil-free solution or oil-water emulsion, the mass-transfer of corrosive species, such as H⁺ and H₂CO₃ in this work, dominates the cathodic process during corrosion of the pipeline steel. With the increase in the fluid flow velocity, the mass transfer is accelerated, as indicated by the increasing diffusive limiting cathodic current density, contributing to increasing corrosion of the steel.

The steel corrosion is increased by elevated temperature. At low solution pH, such as the pH smaller than 5, the increased corrosion kinetics, rather than the scale formation, dominates the temperature effect on the steel corrosion.

The presence of oil in the fluid decreases the steel corrosion, and the effect is amplified with the increasing oil content. This is attributed to the increased opportunity that the pipe wall becomes oil-wetting when the fluid contains more oil. Moreover, the presence of oil in CO₂-saturated fluid flow does not affect the corrosion mechanism of the steel.

By the CFD simulation and the parameter derivation, a semi-empirical model is developed to predict the corrosion rate of steels in CO₂-saturated fluid flow.

Chapter Five: Modelling and prediction of corrosion of steel tubulars in SAGD/CO₂ co-injection and production systems

5.1 Introduction

The rapid growth of Canadian bitumen production is primarily attributed to the use of in-situ recovery technology such as SAGD, where a pair of horizontal wells are drilled into the oil reservoir, and the high temperature steam is injected into the upper tubular to heat the bitumen, causing it to drain into the lower tubular for pumping to the surface [104]. At the same time, to reduce the greenhouse gas (GHG) emission and to enable the sustainability of energy industry, carbon capture and storage (CCS) system and technology have been developed, where the captured CO₂ is stored permanently in deep geological formations or injected it into mature oil fields for EOR [23].

Reservoir simulations predict that, upon injection, a large fraction of the added CO₂ will remain underground without adversely affecting cumulative oil production. Hence, the steam/CO₂ co-injection can be an effective way to significantly reduce the GHG emission during bitumen production by SAGD.

The oil industry has a great interest in the initiative of co-injection of CO₂ with steam into bitumen reservoirs. However, there is a concern that CO₂, once dissolved in liquid existing in the injection and production tubulars, may cause corrosion of the tubulars. To date, there has been few relevant work reported to investigate corrosion in the SAGD/CO₂ co-injection system.

This work developed a model to predict the corrosion rate of tubular steel under the SAGD/CO₂ co-injection and production conditions. The parametric effects, including

temperature, pressure, CO₂ partial pressure, pH, oil phase, solid phase, etc., on the corrosion mechanism, formation of the corrosion scale and the corrosion rate of the steel were considered and quantified. Recommendations were provided to further improve the modelling and prediction accuracy.

5.2 Solubility of CO₂ in water

Determination of the pH of an electrolyte is crucial to corrosion evaluation of steels in the corrosive environments. In fact, in-situ measurement of the solution pH, especially under the high temperature SAGD conditions, is frequently difficult, if not impossible. Analysis of water chemistry can give pH values, but the electrolyte has undergone cooling, depressurization and exposure to atmosphere. Thus, the result is not representative of the reality in service. Derivation by modelling of solution pH based on the involved chemical reactions and their reaction equilibrium constants provides a reliable alternative for this purpose.

For water condensate in injection tubular and the produced water in the production tubular, the primary chemical reactions are similar to those listed in Eqs. (2-1) ~ (2-4). At temperatures higher than 100 °C, large amount of steam exists in the gas phase. Thus, the equilibrium reaction between water and steam should also be considered, and the reaction is expressed as [105]:



Equilibrium constants that describe water and CO₂ are expressed as:

$$K_{\text{H}_2\text{O}} = f_{\text{H}_2\text{O}(\text{g})} / a_{\text{H}_2\text{O}(\text{l})} \quad (5-2)$$

$$K_{\text{CO}_2(\text{g})} = f_{\text{CO}_2(\text{g})} / a_{\text{CO}_2(\text{aq})} \quad (5-3)$$

where K is the reaction equilibrium constant, f is gas fugacity, a is the activity of species in water.

The fugacity of gas i , f_i , is defined as:

$$f_i = \phi_i y_i P \quad (5-4)$$

where ϕ_i and y_i are the fugacity coefficient and mole fraction of component i , respectively. The activity of species i , a_i , is defined as:

$$a_i = \gamma_i x_i \quad (5-5)$$

where γ_i and x_i are the activity coefficient and mole fraction of species i , respectively.

Equilibrium constants $K_{\text{H}_2\text{O}}$ and K_{CO_2} are dependent on both temperature and pressure [106] as:

$$K_{(T,P)} = K_{(T,P^0)}^0 \exp\left(\frac{(P - P^0)\bar{V}_i}{RT}\right) \quad (5-6)$$

where R is the ideal gas constant, T is Kelvin temperature, P and P^0 are the total pressure and reference pressure (P^0 is taken as 0.1 MPa or water saturation pressure), K^0 is the equilibrium constant at the reference pressure, and \bar{V}_i is the average partial mole volume of component i in the pressure interval from P^0 to P .

The average partial mole volume of pure water $\bar{V}_{\text{H}_2\text{O}}$ (cm³/mol) and gaseous CO₂ $\bar{V}_{\text{CO}_2(\text{g})}$ (cm³/mol) are (T is supposed to be no smaller than 373.15 K) [105]:

$$\bar{V}_{\text{H}_2\text{O}} = 18.1 + 3.137 \times 10^{-2} (T - 373.15) \quad (5-7)$$

$$\bar{V}_{\text{CO}_2(\text{g})} = 32.6 + 3.413 \times 10^{-2} (T - 373.15) \quad (5-8)$$

The values of K^0 of water and CO₂ at the reference pressure are obtained by:

$$\log K_{\text{H}_2\text{O}}^0 = -2.1077 + 2.8127 \times 10^{-2} T_c - 8.4298 \times 10^{-5} T_c^2 + 1.4969 \times 10^{-7} T_c^3 - 1.1812 \times 10^{-10} T_c^4 \quad (5-9)$$

$$\log K_{\text{CO}_2(\text{g})}^0 = 1.668 + 3.992 \times 10^{-3} T_c - 1.156 \times 10^{-5} T_c^2 + 1.593 \times 10^{-9} T_c^3 \quad (5-10)$$

where T_c is temperature in °C.

Activities of water and CO₂ can be calculated using Margules expressions [105]:

$$\ln(\gamma_{\text{H}_2\text{O}}) = (A_M - 2A_M x_{\text{H}_2\text{O}}) x_{\text{CO}_2}^2 \quad (5-11)$$

$$\ln(\gamma_{\text{CO}_2}) = 2A_M x_{\text{CO}_2} x_{\text{H}_2\text{O}}^2 \quad (5-12)$$

Margules parameter A_M is zero when temperature is lower than 100 °C. At temperatures above 100 °C, it's expressed as [105]:

$$A_M = -3.084 \times 10^{-2}(T - 373.15) + 1.927 \times 10^{-5}(T - 373.15)^2 \quad (5-13)$$

The equation suggested by Panagiotopoulos and Reidto [107] was used to calculate the gas fugacity coefficient. A minor revision was made on the initial equation for simplicity by assuming that the binary interaction parameter k_{ij} is equal to k_{ji} :

$$\ln(\phi_k) = \frac{b_k}{b_{\text{mix}}} \left(\frac{PV}{RT} - 1 \right) - \ln \left(P \frac{V - b_{\text{mix}}}{RT} \right) + \left[\frac{\sum_{i=1}^n y_i (a_{ik} + a_{ki})}{a_{\text{mix}}} - \frac{b_k}{b_{\text{mix}}} \right] \left(\frac{a_{\text{mix}}}{RT^{1.5} b_{\text{mix}}} \right) \ln \left(\frac{V}{V + b_{\text{mix}}} \right) \quad (5-14)$$

The volume of the compressed gases can be derived by solving the equation of state (EOS). In this work, the Redlich-Kwong (RK) EOS was used, which is given by [108]:

$$P = \frac{RT}{V - b} - \frac{a}{T^{0.5} V(V + b)} \quad (5-15)$$

where V is mole volume of the gas phase at pressure P and temperature T , and a and b are parameters characterizing the intermolecular attraction and repulsion, respectively.

In CO₂-water mixtures, the mixture constants, a_{mix} and b_{mix} , were used to replace a and b in Eq. (5-14), and are calculated by the standard mixing rules [105]:

$$a_{\text{mix}} = \sum_{i=1}^n \sum_{j=1}^n y_i y_j a_{ij} = y_{\text{H}_2\text{O}}^2 a_{\text{H}_2\text{O}-\text{H}_2\text{O}} + 2y_{\text{H}_2\text{O}} y_{\text{CO}_2} a_{\text{H}_2\text{O}-\text{CO}_2} + y_{\text{CO}_2}^2 a_{\text{CO}_2-\text{CO}_2} \quad (5-16)$$

$$b_{\text{mix}} = \sum_{i=1}^n y_i b_i = y_{\text{H}_2\text{O}} b_{\text{H}_2\text{O}} + y_{\text{CO}_2} b_{\text{CO}_2} \quad (5-17)$$

where

$$a_{\text{CO}_2-\text{CO}_2} = 8.008 \times 10^7 - 4.984 \times 10^4 T \text{ (bar cm}^6 \text{ K}^{0.5}/\text{mol}^2) \quad (5-18)$$

$$a_{\text{H}_2\text{O}-\text{H}_2\text{O}} = 1.337 \times 10^8 - 1.4 \times 10^4 T \text{ (bar cm}^6 \text{ K}^{0.5}/\text{mol}^2) \quad (5-19)$$

$$a_{\text{CO}_2-\text{H}_2\text{O}} = \sqrt{a_{\text{CO}_2-\text{CO}_2} a_{\text{H}_2\text{O}-\text{H}_2\text{O}}} (1 - k_{\text{CO}_2-\text{H}_2\text{O}}) \quad (5-20)$$

$$k_{\text{CO}_2-\text{H}_2\text{O}} = K_{\text{CO}_2-\text{H}_2\text{O}} y_{\text{CO}_2} + K_{\text{H}_2\text{O}-\text{CO}_2} y_{\text{H}_2\text{O}} \quad (5-21)$$

$$K_{\text{CO}_2-\text{H}_2\text{O}} = 0.4228 - 7.422 \times 10^{-4} T \quad (5-22)$$

$$K_{\text{H}_2\text{O}-\text{CO}_2} = 1.427 \times 10^{-2} - 4.037 \times 10^{-4} T \quad (5-23)$$

The $b_{\text{H}_2\text{O}} = 15.7 \text{ cm}^3/\text{mol}$, and $b_{\text{CO}_2} = 28.25 \text{ cm}^3/\text{mol}$.

For pure water, the mole fractions of water in the gas phase and CO₂ in the liquid phase can be expressed as:

$$y_{\text{H}_2\text{O}} = \frac{K_{\text{H}_2\text{O}}^0 a_{\text{H}_2\text{O}}}{\phi_{\text{H}_2\text{O}} P} \exp\left(\frac{(P - P^0) \bar{V}_{\text{H}_2\text{O}}}{RT}\right) \quad (5-24)$$

$$x_{\text{CO}_2} = \frac{(1 - y_{\text{H}_2\text{O}}) \phi_{\text{CO}_2} P}{55.508 K_{\text{CO}_2(\text{g})}^0 \gamma_{\text{CO}_2}} \exp\left(-\frac{(P - P^0) \bar{V}_{\text{CO}_2}}{RT}\right) \quad (5-25)$$

where the activity of water, $a_{\text{H}_2\text{O}}$, is:

$$a_{\text{H}_2\text{O}} = \gamma_{\text{H}_2\text{O}} (1 - x_{\text{CO}_2}) \quad (5-26)$$

The activity of CO₂, $a_{\text{CO}_2} = m_{\text{CO}_2} \gamma_{\text{CO}_2}$, where m_{CO_2} is:

$$m_{\text{CO}_2} = \frac{55.508 x_{\text{CO}_2}}{x_{\text{H}_2\text{O}}} \quad (5-27)$$

If salts are contained in the water, the mole fraction of water in the gas phase is still calculated by Eq. (5-24), but the activity of the water, $a_{\text{H}_2\text{O}}$, is rewritten as [105]:

$$a_{\text{H}_2\text{O}} = \gamma_{\text{H}_2\text{O}} (1 - x_{\text{CO}_2} - x_{\text{salt}}) \quad (5-28)$$

where

$$x_{salt} = \frac{\sum \nu m_{salt}}{55.508 + \sum \nu m_{salt} + m_{CO_2}} \quad (5-29)$$

where ν is the stoichiometric number of ions contained in the dissolved salt, and m_{salt} is the molality of a salt compound. m_{CO_2} is calculated with Eq. (5-27) except that:

$$x_{H_2O} = 1 - x_{CO_2} - x_{salt} \quad (5-30)$$

The mole fraction of CO_2 in saline solutions is:

$$x_{CO_2} = \frac{(1 - y_{H_2O}) \phi_{CO_2} P}{55.508 K_{CO_2(g)}^0 \gamma_{CO_2} \gamma'_{CO_2}} \exp\left(-\frac{(P - P^0) \bar{V}_{CO_2}}{RT}\right) \quad (5-31)$$

where the activity coefficient γ'_{CO_2} represents the salting out effect, which means salts exist in the solution reduce the solubility of gases in the solution, as [105]:

$$\begin{aligned} \gamma'_{CO_2} = & \left(1 + \frac{\sum m_i}{55.508}\right) \exp[2\lambda(m_{Na} + m_K + 2m_{Ca} + 2m_{Mg}) \\ & + \xi m_{Cl}(m_{Na} + m_K + m_{Ca} + m_{Mg}) - 0.07m_{SO_4}] \end{aligned} \quad (5-32)$$

where λ and ξ are coefficients that are defined as a function of temperature by:

$$\lambda = 2.217 \times 10^{-4} T + 1.074/T + 2648/T^2 \quad (5-33)$$

$$\xi = 1.3 \times 10^{-5} T - 20.12/T + 5259/T^2 \quad (5-34)$$

The activity of CO₂ in saline solutions is $a_{\text{CO}_2} = m_{\text{CO}_2} \gamma_{\text{CO}_2} \gamma'_{\text{CO}_2}$. An iterative method is used for computation.

5.3 Determination of solution pH

After dissolution of CO₂ in water, carbonic acid and other relevant species are formed, as illustrated in Eqs. (2-2) ~ (2-4). For the CO₂ hydration reaction, the chemical reaction equilibrium is written as [97]:

$$K_{\text{hy}} = \frac{C_{\text{H}_2\text{CO}_3}}{a_{\text{CO}_2} a_{\text{H}_2\text{O}}} \quad (5-35)$$

where K_{hy} is the CO₂ hydration equilibrium constant, and $C_{\text{H}_2\text{CO}_3}$ is the concentration of H₂CO₃, mol/L.

For dissociation of carbonic acid, the reaction equilibrium constant is defined as [97]:

$$K_{\text{ca}} = \frac{C_{\text{H}^+} C_{\text{HCO}_3^-}}{C_{\text{H}_2\text{CO}_3}} \quad (5-36)$$

where K_{ca} is the equilibrium constant for dissociation of H_2CO_3 , and C_{H^+} and $C_{HCO_3^-}$ are the concentrations of H^+ and HCO_3^- , respectively, mol/L.

For the reaction in Eq. (2-4), the equilibrium constant of the bicarbonate dissociation, K_{bi} , is:

$$K_{bi} = \frac{C_{H^+} C_{CO_3^{2-}}}{C_{HCO_3^-}} \quad (5-37)$$

The dissociation of water follows:



The reaction equilibrium constant for water dissociation is defined as:

$$K_{wa} = C_{H^+} C_{OH^-} / a_{H_2O} \quad (5-39)$$

where K_{wa} is the equilibrium constant for dissociation of water; and C_{OH^-} is the concentration of OH^- , mol/L.

In the water condensate containing dissolved CO_2 in the SAGD/ CO_2 injection system, it is reasonable to assume that, in addition to the chemical species mentioned

above, others do not affect corrosion of the steel due to negligible amount. The following relationship is derived according to the electro-neutral theory:

$$C_{\text{H}^+} = C_{\text{HCO}_3^-} + 2C_{\text{CO}_3^{2-}} + C_{\text{OH}^-} \quad (5-40)$$

In the production water, a number of species are present, such as NaHCO₃ and NaCl.

The relationship is revised as:

$$C_{\text{Na}^+} + C_{\text{H}^+} = C_{\text{HCO}_3^-} + 2C_{\text{CO}_3^{2-}} + C_{\text{OH}^-} + C_{\text{Cl}^-} \quad (5-41)$$

where C_{Na^+} and C_{Cl^-} are concentrations of Na⁺ and Cl⁻, respectively.

By combining all equations listed above and considering the charge neutrality and mass balance, the following expression is derived to determine the concentration of hydrogen ions:

$$C_{\text{H}^+}^3 + C_{\text{bicarb}}^0 C_{\text{H}^+}^2 - (\phi K_{\text{sol}} K_{\text{hy}} K_{\text{ca}} P_{\text{CO}_2} + K_{\text{wa}}) \times C_{\text{H}^+} - 2\phi K_{\text{sol}} K_{\text{hy}} K_{\text{bi}} K_{\text{ca}} P_{\text{CO}_2} = 0 \quad (5-42)$$

where C_{bicarb}^0 is the initial concentration of bicarbonate ions, mol/L. When the solution is saturated with FeCO₃, the equation is rewritten as:

$$\left(\frac{2K_{\text{spFeCO}_3}}{\phi K_{\text{sol}} K_{\text{hy}} K_{\text{bi}} K_{\text{ca}} P_{\text{CO}_2}} \right) C_{\text{H}^+}^4 + C_{\text{H}^+}^3 + C_{\text{bicarb}}^0 C_{\text{H}^+}^2 - (\phi K_{\text{sol}} K_{\text{hy}} K_{\text{ca}} P_{\text{CO}_2} + K_{\text{wa}}) \times C_{\text{H}^+} - 2\phi K_{\text{sol}} K_{\text{hy}} K_{\text{bi}} K_{\text{ca}} P_{\text{CO}_2} = 0 \quad (5-43)$$

where K_{spFeCO_3} is the solubility of iron carbonate.

As stated, when the concentrations of Fe^{2+} and CO_3^{2-} ions present in the solution exceed the solubility limit, solid iron carbonate is formed by Eq. (2-12) and deposited on the steel surface. The solubility is defined as [109]:

$$K_{\text{spFeCO}_3} = C_{\text{Fe}^{2+}} C_{\text{CO}_3^{2-}} \quad (5-44)$$

where $C_{\text{Fe}^{2+}}$ and $C_{\text{CO}_3^{2-}}$ are the concentrations of Fe^{2+} and CO_3^{2-} , respectively, mol/L. It's noted that all equilibrium constants mentioned above are included in Appendix A.

After the concentration of hydrogen ions is calculated, the solution pH is determined by:

$$\text{pH} = -\log(C_{\text{H}^+}) \quad (5-45)$$

A computational code, which integrates all equations and constants as listed, is written based on Visual Basic, where solutions to the equations are derived by Newton's method. The user-interface is shown in Figure 5.1. The solution pH can be obtained upon

provision of various input conditions, such as temperature, operating pressure, CO₂ partial pressure, and concentrations of various species contained in the solution, etc.

The user-interface for determining solution pH includes the following elements:

- Temperature (K) input field
- Operating Pressure (Bar) input field
- CO₂ Partial Pressure (Bar) input field
- Concentration of Ca²⁺ (mol/l) input field
- Concentration of Na⁺ (mol/l) input field
- Concentration of K⁺ (mol/l) input field
- Concentration of HCO₃⁻ (mol/l) input field
- Concentration of Cl⁻ (mol/l) input field
- Radio buttons for "Condensate or Formation water ?" with "Formation water" selected.
- Radio buttons for "Will Iron Carbonate saturation be Considered ?" with "No" selected.
- pH output field
- Calculate pH button
- Help button
- Exit button

Figure 5.1 The user-interface of the computational code for determination of the solution pH.

5.4 CO₂ corrosion of steel tubular in water condensate in SAGD/CO₂ injection system

To calculate the corrosion rate of steel tubulars in water condensate in SAGD/CO₂ injection system, it is assumed that the water condensate is present as a water film over a certain area, rather than isolated water droplets, on the steel surface. Corrosion of the steel occurs uniformly in the water film. The corrosion rate, V_{corr} , is calculated using Eq. (2-21).

The calculated corrosion rate V_{corr} is only used for CO₂ saturated bulk water, without considering the formation of corrosion product film. In addition, the presence of protective scale and various species, such as H₂S, oil, organic acids and even inhibitors, would affect the corrosion rate. Thus, correction factors must be determined to improve the corrosion rate calculation.

Under conditions encountered in the SAGD/CO₂ injection and production systems (such as high temperature and near-neutral pH conditions), the iron carbonate scale is anticipated to form on the steel surface to protect the steel from further corrosion. The scaling temperature, T_{scale} , above which the protective scale can be formed, is determined by [67]:

$$T_{\text{scale}} = \frac{2400}{6.7 + 0.6 \log(\phi P_{\text{CO}_2})} \quad (5-46)$$

The scaling factor, F_{scale} , for corrosion protection when the scale is formed above the scaling temperature is expressed as [67]:

$$\log(F_{\text{scale}}) = \frac{2400}{T} - 0.6 \log(\phi P_{\text{CO}_2}) - 6.7 \quad (5-47)$$

The scaling factor gives a minimum estimation of the protectiveness of the scale. However, it is noted that the risk of the film breakdown may undermine the protectiveness of the scale, and, sometimes, even lead to pitting corrosion. Moreover, the scale can be thinned by fluid flow.

Previous work showed [67] that the corrosion rate of steels exposed to condensed water phase in CO₂ environments decreases with time. The condensation factor, F_{cond} , is used to include its effect as:

$$F_{\text{cond}} = 0.1, \text{ when condensate rate (g/m}^2 \text{ s)} < 0.25$$

$$F_{\text{cond}} = 0.4 \times \text{condensate rate, when condensate rate} < 2.5 \quad (5-48)$$

$$F_{\text{cond}} = 1, \text{ when condensate rate} \geq 2.5$$

5.5 CO₂ corrosion of steel tubulars in oil-water emulsion in SAGD/CO₂ production system

To determine the corrosion rate of steel tubulars in oil-water emulsions contained in the SAGD/CO₂ production system, the following assumptions are made. The oil-water emulsion is uniform in the tubular and on the steel surface. Since the water cut is above 60% in the production tubular, water is assumed as the continuous phase and oil as the dispersive phase. If the steel is oil-wetted, corrosion does not occur. Under water-wetting, the steel corrosion happens. Previous work [39] found that the addition of oil in the electrolyte reduces the corrosion rate of steels. Thus, the corrosion rate of the steel tubular in production system is first calculated in oil-free water. An oil-inhibitive factor is then added to account for the effect of oil on the steel corrosion.

The oil-inhibitive factor, F_{oil} , is calculated as [110]:

$$F_{\text{oil}} = 0.071 \frac{W}{W_{\text{break}}} U_{\text{liq}} \quad (W < W_{\text{break}}, F_{\text{oil}} \leq 1)$$

$$F_{\text{oil}} = 0.071 \frac{W}{W_{\text{break}}} U_{\text{liq}} + 0.545 \frac{\alpha}{90} + 0.071 \frac{\alpha}{90} \frac{W}{W_{\text{break}}} U_{\text{liq}} \quad (W \geq W_{\text{break}}, F_{\text{oil}} \leq 1) \quad (5-49)$$

where W is the average water fraction in the liquid, α is the angle of the tubular deviating from the vertical direction, and W_{break} is the breakpoint of water in oil-water emulsion,

which indicates the interfacial tension between oil and water. Generally, the smaller the W_{break} , the more water is present in the emulsion. The W_{break} is expressed as:

$$W_{\text{break}} = -0.0166 \times {}^\circ API + 0.83 \quad (20 < {}^\circ API < 50) \quad (5-50)$$

where the ${}^\circ API$ gravity is used to express the density of oil. A small value is associated with a high oil density.

At high water cuts, the validity of Eq. (5-49) is limited. An additional constraint is added:

$$F_{\text{oil}} \geq W \quad (5-51)$$

At a very small flow velocity or near stagnant conditions,

$$U_{\text{liq}} < \frac{\alpha}{90}, F_{\text{oil}} = 1 \quad (5-52)$$

5.6 Corrosion of steel tubulars in oil-water-sand multi-phased fluid

Inorganic sands contained in the fluid would enhance corrosion of steel tubulars by two mechanisms [111], i.e., breakage of the protective scale and exposure of the steel to corrosive medium, and depolarization of the anodically or cathodically controlled corrosion process by plastic deformation and/or disruption of the steel surface. The erosion rate for mild steels in sand-containing fluid can be calculated by [112]:

$$E_{\text{erosion}} = 0.223U_p^{2.148}d_p^{0.344}C_w^{0.556} \quad (5-53)$$

where E_{erosion} is the erosion rate, mm/year; U_p is the flow velocity of solid particles, m/s; d_p is the particle diameter, μm ; and C_w is the sand concentration, wt. %. The enhanced steel corrosion by sand induced erosion can thus be quantified by modifying the corrosion rate with the erosive effect factor

5.7 Quantitative prediction of corrosion rate of steel tubulars in SAGD/CO₂ co-injection and production systems

5.7.1 Corrosion rate of the injection tubular

The operating conditions of the SAGD/CO₂ co-injection tubular are shown in Table 5.1. It is seen that there are two sets of operating conditions to be considered in this work. The total operating pressures of the tubular are 1,500 kPa and 3,000 kPa. It is believed that the pressures provided by industry are the gauge-measured ones. Thus, the absolute pressures, i.e., the gauge pressure plus atmospheric pressure, of the injection tubular are 1,601 kPa and 3,101 kPa, respectively. In the following analysis, the operating pressure of the steel tubular refers to the gauge-measured value.

Table 5.1 The operating conditions of the SAGD/CO₂ co-injection tubular.

	Condition 1	Condition 2
Total operating pressure, gauge (kPa)	1,500	3,000
Total operating pressure, absolute (kPa)	1,601	3,101
Water content in steam (wt. %)	5	10
CO ₂ content in steam (wt. %)	5	10
Steam chemistry	Very clean	
Steam flow velocity (m ³ /h)	6 ~ 8	
Tubular diameter (mm)	102.9	

- ***CO₂ partial pressure***

The CO₂ contents under the two operating conditions are 5 wt. % and 10 wt. %, respectively, as shown in Table 5.1. The ratio of pressures is proportional to the ratio of molar quantities. With the molar weights of CO₂ and steam, which are 44 g/mol and 18 g/mol, respectively, the CO₂ partial pressure, P_{CO_2} , under condition 1 can be calculated as:

$$P_{\text{CO}_2} = \frac{\frac{5\% \times \text{total weight}}{44} + \frac{90\% \times \text{total weight}}{18}}{44} \times P \quad (5-54)$$

where P is the total operating pressure of the tubular. Similarly, the P_{CO_2} under condition 2 can be calculated in the same way. With the known parameters, the calculated P_{CO_2} under conditions 1 and 2 in Table 5.1 are 33 kPa and 146 kPa, respectively.

- ***Operating temperature***

Without extra information provided, the operating temperature is taken as the steam saturation temperature at absolute pressure of the steam (determined by subtracting the CO₂ partial pressure from the total pressure). By referring to the data base edited by the National Institute of Standard and Technology (NIST) [113], the operating temperatures are obtained as 201.4 °C and 235.8 °C, respectively.

- ***Average fluid density***

Based on the volume fraction of liquid (water) and gas (steam and CO₂) phases present in the fluid, the average density of the fluid can be calculated by:

$$\text{Average density} = \frac{\text{total weight}}{\frac{\% \text{ water} \times \text{total weight}}{863.0} + \frac{\% \text{ steam} \times \text{total weight}}{8.1}} \quad (5-55)$$

where the values 863.0 and 8.1 refer to the density of water and steam at condition 1, i.e., 863.0 kg/m³ and 8.1 kg/m³, respectively. From Table 5.1, the weight fractions of water and steam in the fluid under condition 1 are 5% and 90%, respectively. Under condition 2, the weight fractions of water, and steam are 10% and 80%, respectively. For the two operating conditions, the average densities of the fluid for conditions 1 and 2 are 9.0 kg/m³ and 19.3 kg/m³, respectively.

- ***Thickness of the water condensate film***

The diameter of the tubular is 0.1029 m. The weight of the fluid per unit length under the two sets of operating conditions are calculated to be 0.0731 kg and 0.1537 kg, respectively, from the tubular volume and the average density of the fluid, which is calculated above.

The water contents in steam are 5 wt. % and 10 wt. % under the two conditions. The thickness of the water condensate film can be calculated by:

$$V_{\text{H}_2\text{O}} = 1/4 \times \pi \times [d^2 - (d - \delta)^2] \quad (5-56)$$

where δ is the thickness of the water condensate film, m; $V_{\text{H}_2\text{O}}$ is the volume of the water condensate, which is calculated from the weight and density of water, m^3 ; and d is the diameter of the tubular, m. Assume a layer of uniform water condensate, the thicknesses of the condensate film are 0.5 mm and 1.2 mm, respectively, under the two operating conditions listed in Table 5.1.

- ***Flow velocity of the steam***

As seen in Table 5.1, the flux of the steam flow is $8 \text{ m}^3/\text{h}$. The flow velocity is calculated as:

$$U_{\text{liq}} = \frac{Q}{A} = \frac{8 \text{ m}^3/\text{h}}{1/4 \times \pi \times (0.1029)^2 \times 3600 \text{ m}^2/\text{s/h}} = 0.267 \text{ m/s} \quad (5-57)$$

where Q is the flow flux, m^3/h ; and A is the cross-sectional area of the tubular, m^2 . It is noted that the actual flow velocity of liquid phase (water condensate) can be smaller than that of steam as calculated above. The corrosion rate calculated based on the above formula is thus somewhat conservative.

- ***Condensing rate and condensation factor***

With the density of water condensate and its flow velocity under given conditions, the condensing rate can be calculated by multiplying the two values. For example, the condensing rate under condition 1 in Table 5.1 is $863.5 \times 10^3 \text{ g/m}^3 \times 0.267 \text{ m/s} = 2.3 \times 10^5$

$\text{g/m}^2\cdot\text{s} \gg 2.5 \text{ g/m}^2\cdot\text{s}$. According to the criterion expressed in Eq. (5-48), the condensation factor, F_{cond} , under the two conditions are both set as 1.0.

During corrosion of the steel tubular in water condensate, the concentration of Fe^{2+} increases while H^+ ions and dissolved H_2CO_3 are consumed. When the product of the concentrations of Fe^{2+} and CO_3^{2-} exceeds the solubility limit, K_{spFeCO_3} , of FeCO_3 , the iron carbonate scale starts to precipitate. Under the operating conditions, Fe_3O_4 could also be formed due to the reaction of FeCO_3 with water [114]. Since the flow velocity of the liquid is small, the water solution is expected to be saturated with FeCO_3 or Fe_3O_4 or both. Thus, the solution pH at the saturation condition is used to calculate the corrosion rate of the steel.

Based on all calculated parameters summarized above, the corrosion rate of the steel tubular in SAGD/ CO_2 co-injection system is shown in Table 5.2. Important findings can be obtained from modelling of the steel corrosion in SAGD/ CO_2 co-injection tubulars. It is seen that, in the absence of iron carbonate scale, the corrosion rate of the steel tubular is quite high in water condensate, especially under condition 2, where the corrosion rate is up to 2.26 mm/year. However, after the scale is formed on the steel, corrosion of the steel is remarkably inhibited. Compare the corrosion rate of the scale-covered steel with that of bare steel, the latter is over 100 times higher than the former. Obviously, if the scale remains intact on the steel surface, the injection tubular will maintain its integrity in the system.

Table 5.2 The calculated parameters for calculation of the corrosion rate and the corrosion rates of the steel tubular in SAGD/CO₂ co-injection system.

	Condition 1	Condition 2
Temperature (K)	474.55	508.95
P_{CO_2} (Bar)	0.33	1.46
pH	Non-saturated	4.86
	Saturated	5.74
V_r (mm/year)	80.08	309.08
V_m (mm/year)	0.51	2.28
V_{corr} - scale free (mm/year)	0.51	2.26
F_{scale}	0.044	0.008
F_{cond}	1.00	1.00
V_{corr} - with scale (mm/year)	0.0224	0.0181

5.8 Corrosion rate of the production tubular

5.8.1 Corrosion rate of the steel in oil-water emulsions

The operating condition of the production tubular is shown in Table 5.3. It is seen that, identical to the injection tubular, there are two operating conditions where corrosion is to be modelled. The fluid in the production tubular contains oil, water and solid sands. Thus, the fluid is under a multiphase flow condition. It has been known that the presence of sands could lead to erosion corrosion. Thus, a high corrosion rate of the steel is expected.

The total operating pressure of the production tubular is ranged from 500 kPa to 2,000 kPa. The temperature is the equilibrium temperature at each pressure. Generally, although steam does not exist in the fluid, the equilibrium temperature is not simply the boiling temperature of water at individual pressures. The presence of oil and its composition and properties will affect the equilibrium temperature. However, with limited information provided and also for simplification of numerical calculation, the

equilibrium temperatures are assumed to be the boiling temperatures of water at each pressure, which are 159 °C and 215 °C, respectively.

Table 5.3 Operating conditions of the production tubular in SAGD/CO₂ co-injection systems.

	Condition 1	Condition 2
Total operating pressure (kPa)	500	2,000
Oil-water emulsion composition (wt. %)	Oil: 25 ~ 30; Water: 75 ~ 70	
Sand content (wt. %)	0.6 ~ 0.7	
CO ₂ content in oil-water emulsion (mol %)	f(pressure)	
Emulsion flow velocity (m ³ /h)	20	
Tubular diameter (mm)	102.9	

The composition of the oil-water emulsion is given in a range. To model the most corrosive environmental condition, the oil composition is set as 25% and water the balance (the presence of oil can inhibit the steel corrosion). The chemistry of the SAGD-produced water from Bridle's work [115], as shown in Table 5.4, is used for the ionic strength selection and pH calculation. The species with a content no larger than 1 mg/L are eliminated from the work.

According to Table 5.4, the initial ionic strength of the produced water is calculated to be 0.066 mol/L.

Table 5.4 Chemical composition of the SAGD-produce water [115].

Species	Content (mg/L)	Molar concentration (mmol/L)
Ca ²⁺	8	0.2
Na ⁺	1420	61.7
K ⁺	148	3.8
HCO ₃ ⁻	237	3.9
Cl ⁻	2200	62.0

The flow flux of the oil-water emulsion is 20 m³/h (Table 5.3). The flow velocity is calculated as:

$$U_{\text{liq}} = \frac{Q}{A} = \frac{20 \text{ m}^3/\text{h}}{1/4 \times \pi \times (0.1029)^2 \times 3600 \text{ m}^2/\text{s/h}} = 0.668 \text{ m/s} \quad (5-58)$$

The CO₂ content in oil-water emulsions is not known. Since the CO₂ partial pressure is critical in calculation of the corrosion rate, a range of P_{CO_2} is assumed. With the condition of the operating temperature, CO₂ partial pressure and water chemistry, the solution pH can be obtained by the developed computational code. Figures 5.2 and 5.3 show the calculated solution pH and scaling factor, F_{scale} , as a function of CO₂ partial pressure under the total operating pressures of 500 kPa and 2,000 kPa, respectively. The CO₂ partial pressure of 0.1 ~ 2.5 bar is selected for the total operating pressure of 500 kPa, and 0.1 ~ 10 bar for the operating pressure of 2,000 kPa condition.

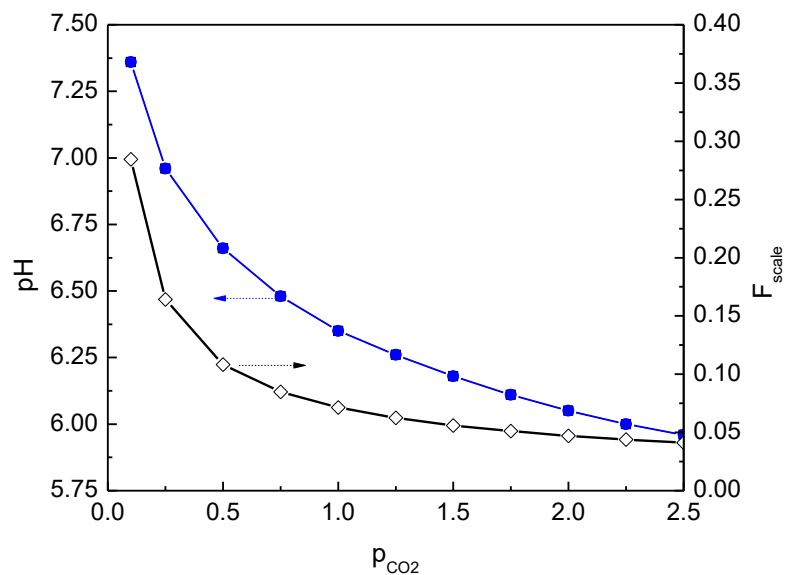


Figure 5.2 Solution pH and scaling factor calculated at various CO₂ partial pressures (Operating pressure 500 kPa, and flow flux 20 m³/h).

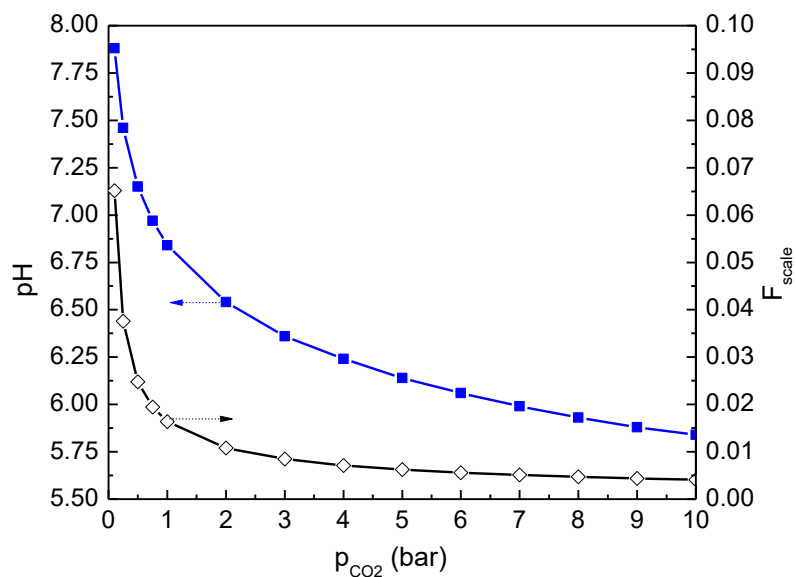


Figure 5.3 Solution pH and scaling factor calculated at various CO₂ partial pressures (Operating pressure 2,000 kPa, and flow flux 20 m³/h).

The properties of oil in SAGD operation are not given. If the API density of the oil in the production tubular is between 20 and 50, such as API 21, the oil effect factor, F_{oil} , is calculated to be 0.69 by Eqs. (5-49) and (5-50). However, according to Eq. (5-51), the F_{oil} should not be smaller than the fraction of water in the emulsion, i.e., 0.75. Moreover, F_{oil} should be 1 if Eq. (5-52) is considered. Since the addition of oil is able to reduce the steel corrosion at relative low flow velocities, the value 0.9 is used for F_{oil} in this work to reflect the inhibitive effect of oil. A corrective factor can be obtained based on the real API if provided.

Combine the calculated corrosion rate V_{corr} with the F_{scale} and F_{oil} , the minimum corrosion rate of the steel can be determined. Assume that the steel is at the maximum corrosion rate when the scale is not formed, or the formed scale does not provide sufficient protection to the steel. The maximum corrosion rate is simply the calculated corrosion rate, V_{corr} , i.e., the corrosion rate without protection from scale and inhibition by oil. Both the minimum and maximum corrosion rates of the steel tubular in oil-water emulsions in the production system are shown in Figures 5.4 and 5.5 under the operating pressures of 500 kPa and 2,000 kPa, respectively.

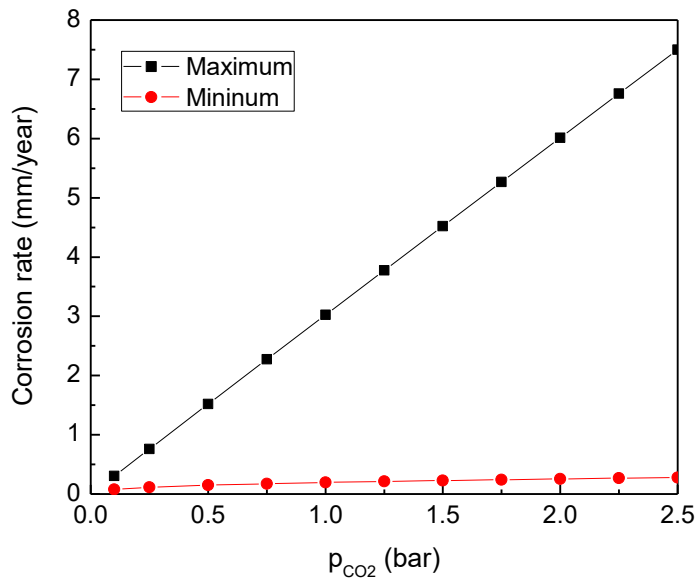


Figure 5.4 Maximum and minimum corrosion rate at various CO₂ partial pressures

(Operating pressure 500 kPa and flow flux 20 m³/h).

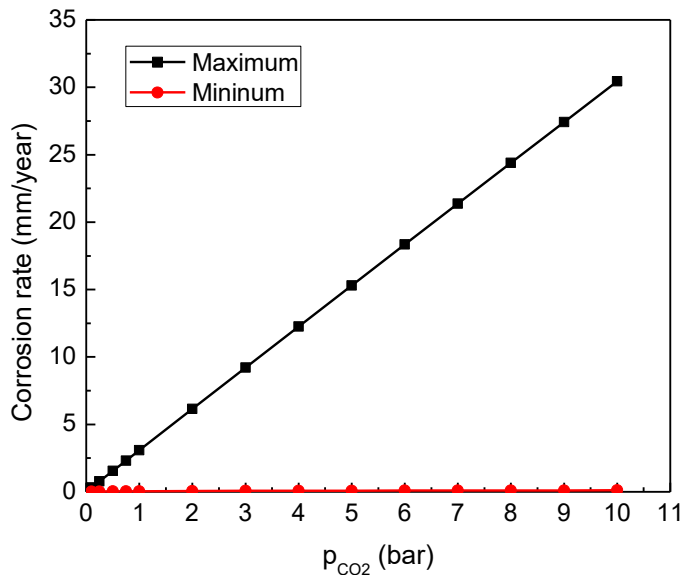


Figure 5.5 Maximum and minimum corrosion rate at various CO₂ partial pressures

(Operating pressure 2,000 kPa and flow flux 20 m³/h).

5.8.2 Corrosion rate of the production tubular in oil-water-sand fluid

To simulate the effect of sands on the steel corrosion, the size and concentration of sands are selected as 250 μm and 0.7 wt. %, respectively. The sand size is consistent with others' work conducted on oil pipeline corrosion [116], and the content of sands takes the upper percentage present in the production tubular, as shown in Table 5.3. It is assumed that the flow velocity of sands is approximately identical to that of the oil-water emulsion, which is calculated to be 0.668 m/s. The erosion rate of the steel due to sands can be calculated from Eq. (5-53), and is equal to 0.51 mm/year.

Consider the low content of sands contained in the emulsion, the synergism of corrosion and erosion is ignored. The total metal loss of bare steel, i.e., the scale-free steel tubular, in oil-water-sand fluid is simply the summation of corrosion rates shown in Figures 5.4 (operating pressure 500 kPa) and 5.5 (operating pressure 2,000 kPa) and the calculated erosion rate. It can be found that, at small CO_2 partial pressures, the erosion rate is comparable to the corrosion rate. Thus, the sand-induced erosion is important to degrade the steel tubular. As the increase in P_{CO_2} , the corrosion rate increases rapidly. The erosion rate becomes much smaller than the corrosion rate, and does not make a big contribution to the steel degradation.

When a layer of protective scale is formed on the steel surface, the corrosion rate of the steel is much smaller than the calculated erosion rate. However, it is not meaningful to add the corrosion and erosion rates to obtain the total metal loss. The presence of scale would inhibit the erosion induced by sands, especially when the sand content is low in the emulsion. However, the sands in flowing condition are able to damage, such as causes

breakage or local thinning, the scale. When the scale is broken locally, localized corrosion would occur. Since the sand content is small and a large amount of oil is present, it is expected that there is a small possibility to encounter the sand induced scale breakage and localized corrosion.

5.9 Summary

A model is developed to calculate and predict the corrosion rate of both injection and production steel tubulars in SAGD/CO₂ co-injection system. A computational code is written to enable calculation of the pH of CO₂-saturated solutions present in the steel tubulars based on mechanistic analysis of chemical reactions and use of the reaction equilibrium constants. In addition to solution pH, the effects of CO₂ partial pressure, scaling factor, oil and sands on the steel corrosion are quantified.

For the injection tubular, the CO₂ corrosion rates of the steel in water condensate are 0.0224 mm/year and 0.0181 mm/year under the operating pressures of 1,500 kPa and 3,000 kPa, respectively. The formation of a compact scale, which may be composed of iron carbonate and Fe₃O₄, under high temperatures plays a great role in protecting the steel from corrosion.

For the production tubular, the corrosion rate of steel in oil-water emulsions is derived under two situations. In the presence of a layer of compact scale, the corrosion rate of the steel is quite small; while the maximum corrosion rate is obtained on the scale-free steel. Since the CO₂ content in oil-water emulsions is not given, the corrosion rate of the steel as a function of CO₂ partial pressure is derived. Moreover, the oil effect factor cannot be quantified because the property of the oil is unknown. However, the inhibitive

effect of oil is limited. The presence of sands in oil-water emulsions could potentially result in erosion of the steel. When a compact scale is formed, the role of erosion in steel corrosion is negligible. When the steel tubular is free of scale, erosion could contribute to an enhanced corrosion. Since the sand content is low, the effect of sands on the corrosion rate is not expected to be significant, especially when oil is present.

Under the SAGD/CO₂ co-injection and production conditions, a layer of compact scale would be formed on the surface of steel tubulars, effectively protecting the tubular from corrosion attack. The research findings from this work confirm that corrosion is not an essential threat to the integrity of steel tubulars in SAGD/CO₂ co-injection systems. It is noted that this conclusion does not consider breakdown of the scale. Once it occurs, the corrosion rate of the steel increases remarkably. Moreover, localized corrosion could happen.

Investigation of corrosion of steel tubulars in SAGD system is quite limited compared to corrosion research in other areas of petroleum production. This causes limited data available for verification of the modelling results. Although laboratory testing could provide corrosion data on steel coupons installed in high temperature high pressure autoclaves, the testing conditions, such as hydrodynamic condition, scale-formation condition, etc., are not representative of the reality in SAGD systems. Thus, the lab testing data are not expected to be useful for the modelling verification. It is recommended that reliable lab testing methods be developed to enable reproduction of the corrosive environment where the steel tubular is experienced in SAGD system. Furthermore, it is recommended that corrosion monitoring techniques be developed and installed in-situ for instant corrosion measurements in the field.

Chapter Six: Modelling of corrosion of steel tubing in CO₂ storage *

6.1 Introduction

The global warming observed over the past 50 years is attributed to human activities, from which CO₂ emission due to fossil fuel burning makes the largest contribution [23]. Besides CO₂ injection in wells, which is primarily for enhanced oil recovery purpose, CO₂ storage in sites, such as saline formations and exhausted oil/gas fields, is also a practically effective solution to reduce CO₂ emission, and has been operated worldwide over the recent years.

Under CO₂ storage conditions, CO₂ is present under supercritical conditions at temperatures over 31 °C and the pressure of about 7.38 MPa [24]. In the presence of water, dissolved CO₂ can make a very corrosive environment. Generally, cement is applied to the exterior of the steel tubing [117] for reinforcing purpose, and also protecting the tubing by isolating them from the surrounding environment. However, the cement can be intrinsically incomplete or fail to reach the expected height due to poor cementing job [118, 119]. Moreover, cement can become degraded in the harsh downhole environments. Stress cracking may happen on the cement due to the earth and rock movement [120]. When the protection from surrounding cement fails, the tubing would suffer from severe corrosion. The corrosion rate of carbon steel tubing as high as 10 mm/year [18, 19] was reported.

* This work has been published as: Q. Li, Y.F. Cheng, Modeling of corrosion of steel tubing in CO₂ storage, *Greenhouse Gases-Science and Technology*, 6 (2016) 797-811.

Experimental work has been performed to study corrosion of steels under supercritical CO₂ conditions, but suffering from the difficulty to reproduce the realistic environmental conditions. Instead, modelling has been emerging as an effective alternative to enable prediction of the steel corrosion and facility reliability under harsh environmental conditions such as that of the CO₂ storage. Some models have been developed for corrosion prediction under high CO₂ pressure conditions. Nevertheless, they either did not apply for the CO₂ storage conditions [87] or gave too conservative results because important factors that affect the steel corrosion were not included. For example, Han et al. [44] developed a coupled electrochemical-geochemical model to predict corrosion of mild steels under high pressure CO₂-saline environments. The model did not consider the effect of scale formation on the corrosion rate, thus causing relatively conservative predictive results.

In this research, a new mechanistic model was developed to predict the corrosion of steel tubing under CO₂ storage conditions. The uniqueness of this model is in the integration of a number of interrelated sub-models that describe and quantify individual steps occurring during corrosion processes. The parametric effects, including CO₂ partial pressure (up to 60 MPa), temperature (up to 120 °C), salinity of brine water and the presence of geological species (H⁺, Na⁺, Ca²⁺, OH⁻, Cl⁻, HCO₃⁻, SO₄²⁻), on the steel corrosion were modelled. Moreover, the corrosion rate was determined by consideration of the effect of a protective scale formed on the steel surface. The modelling results were validated by the laboratory testing data obtained from controlled experimental work, and by the data collected from available literature. The limitations of the model were also discussed.

6.2 Overview of the model

Figure 6.1 shows the physical block of the model developed in this work, where the cement is absent from the tubing, exposing the steel to ground water directly. CO_2 is dissolved in water, and various chemical species are at an equilibrium state initially. During corrosion, the species are either consumed or generated at the steel/solution interface, accompanying diffusion of ions in the solution. Corrosion scale is formed on the steel surface, and affects both the diffusion of species and the corrosion rate of the steel.

The mechanistic model for corrosion of steels under CO_2 storage conditions considers three interrelated processes, i.e., chemical reactions including homogeneous reactions occurring in the solution and heterogeneous reactions occurring at the gas/liquid interface (CO_2 hydration) and on the steel surface (scale formation), electrochemical reactions at the steel/solution interface, and mass transfer of corrosive species in the solution. The following assumptions are made to facilitate numerical calculations:

- Precipitation of inorganic CaCO_3 and CaSO_4 on the steel surface and their effect on corrosion are ignored;
- The concentration of corrosive species is uniformly distributed along the axial direction of the tubing; and
- One-dimensional computational domain from the steel surface to the liquid/gas interface is used for modelling purpose.

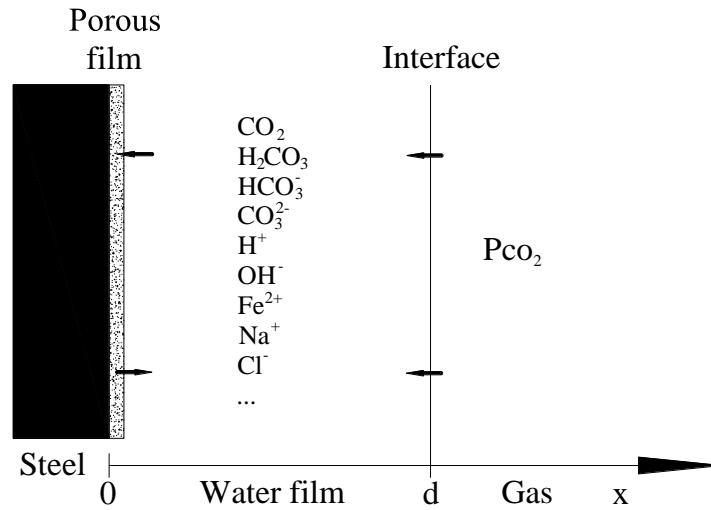


Figure 6.1 Schematic diagram of the physical model in the mechanistic modelling.

6.3 Water chemistry sub-model

6.3.1 Chemical reactions and reaction equilibrium constants

In brine water systems containing H^+ , Na^+ , Ca^{2+} , OH^- , Cl^- , HCO_3^- , SO_4^{2-} and $CO_{2(aq)}$, at temperature below 120 °C and the total pressure of 60 MPa, the following chemical reactions, along with their reaction equilibrium constants, are considered:

$$K_{hy} = \frac{m_{H_2CO_3} \cdot \gamma_{H_2CO_3}}{a_{CO_2} \cdot a_{H_2O}} \quad (6-1)$$

$$K_{ca} = \frac{(m_{H^+} \cdot \gamma_{H^+}) \cdot (m_{HCO_3^-} \cdot \gamma_{HCO_3^-})}{m_{H_2CO_3} \cdot \gamma_{H_2CO_3}} \quad (6-2)$$

$$K_{bi} = \frac{(m_{H^+} \cdot \gamma_{H^+}) \cdot (m_{CO_3^{2-}} \cdot \gamma_{CO_3^{2-}})}{m_{HCO_3^-} \cdot \gamma_{HCO_3^-}} \quad (6-3)$$

$$K_{\text{wa}} = \frac{(m_{\text{H}^+} \cdot \gamma_{\text{H}^+}) \cdot (m_{\text{OH}^-} \cdot \gamma_{\text{OH}^-})}{a_{\text{H}_2\text{O}}} \quad (6-4)$$

$$K_{\text{spFeCO}_3} = (m_{\text{Fe}^{2+}} \cdot \gamma_{\text{Fe}^{2+}}) \cdot (m_{\text{CO}_3^{2-}} \cdot \gamma_{\text{CO}_3^{2-}}) \quad (6-5)$$

where K is the reaction equilibrium constant, f is the gas fugacity, a and γ are activity and activity coefficient of species in the solution, and m is the mole quantity (mol/kg H₂O) of the species. The values of $K_{\text{H}_2\text{O}}$ and $K_{\text{CO}_2(\text{g})}$ will be discussed later, and the other equilibrium constants are available in literature [109, 121-124].

It is noted that the fugacity and activity, rather than pressure and concentration, are used to quantify the CO₂ partial pressure and the concentration of species, respectively, in order to improve the accuracy of modelling results under high pressure CO₂ conditions.

6.3.2 Solubility of CO₂ in H₂O

In CO₂-brine systems, the equilibrium constants $K_{\text{H}_2\text{O}}$ and K_{CO_2} are dependent on temperature and pressure [106], as indicated in Eq. (5-6).

The average partial molar volume of pure water ($\bar{V}_{\text{H}_2\text{O}} = 18.1 \text{ cm}^3/\text{mol}$) and CO₂ ($\bar{V}_{\text{CO}_2(\text{g})} = 32.6 \text{ cm}^3/\text{mol}$, $\bar{V}_{\text{CO}_2(\text{l})} = 32 \text{ cm}^3/\text{mol}$), and the K parameters at reference pressure are obtained from the literature [106, 125].

$$\log K_{\text{H}_2\text{O}}^0 = -2.209 + 3.097 \times 10^{-2} T_c - 1.098 \times 10^{-4} T_c^2 + 2.048 \times 10^{-7} T_c^3 \quad (6-6)$$

$$\log K_{\text{CO}_2(\text{g})}^0 = 1.189 + 1.304 \times 10^{-2} T_c - 5.446 \times 10^{-5} T_c^2 \quad (6-7)$$

$$\log K_{\text{CO}_2(\text{l})}^0 = 1.169 + 1.368 \times 10^{-2} T_c - 5.380 \times 10^{-5} T_c^2 \quad (6-8)$$

where T_c is temperature, °C.

At subcritical CO₂ temperatures and pressures, there is a phase change between gaseous CO₂ and liquid CO₂. $K_{\text{CO}_2(\text{l})}^0$ is used to replace $K_{\text{CO}_2(\text{g})}^0$ when the following conditions are met:

- Temperature is below 31 °C (the round-off value of the critical temperature of pure CO₂);
- The calculated volume of the compressed gas phase is < 94 cm³/mol (the round-off value of the critical volume of pure CO₂) [106].

Mole fractions of water in the gas phase, $y_{\text{H}_2\text{O}}$, can be calculated by Eq. (5-24). The dissolved CO₂ concentration in the liquid phase, m_{CO_2} , is calculated with Eq. (5-27).

6.3.3 Fugacity coefficient

The fugacity coefficient can be derived from the EOS, which is able to calculate properties of CO₂-water mixtures. In this work, the Redlich-Kwong (RK) EOS, i.e., (Eq. (5-15)), is used to determine the fugacity coefficient and volume of the compressed gas [108].

In CO₂-water mixtures, the constants, a_{mix} and b_{mix} , are used to replace a and b , and are calculated by Eq. (5-16) and (5-17) [106]:

$$a_{\text{CO}_2\text{-CO}_2} = 7.54 \times 10^7 - 4.13 \times 10^4 \cdot T \cdot \text{bar} \cdot \text{cm}^6 \cdot \text{K}^{0.5} \cdot \text{mol}^{-2} \quad (6-9)$$

$$a_{\text{H}_2\text{O}-\text{CO}_2} = 7.89 \times 10^7 \text{ T} \cdot \text{bar} \cdot \text{cm}^6 \cdot \text{K}^{0.5} \cdot \text{mol}^{-2} \quad (6-10)$$

$b_{\text{CO}_2-\text{CO}_2} = 27.8 \text{ cm}^3/\text{mol}$, and $b_{\text{H}_2\text{O}-\text{H}_2\text{O}} = 18.18 \text{ cm}^3/\text{mol}$. The value of $y_{\text{H}_2\text{O}}$ is very small and negligible, which gives $y_{\text{CO}_2} = 1$ by mixing rules. The fugacity, ϕ_{CO_2} and $\phi_{\text{H}_2\text{O}}$, can be calculated in a direct, non-iterative manner by:

$$\begin{aligned} \ln(\phi_k) = & \ln\left(\frac{V}{V-b_{\text{mix}}}\right) + \left(\frac{b_k}{V-b_{\text{mix}}}\right) - \left(\frac{2\sum_{i=1}^n y_i a_{ik}}{RT^{1.5} b_{\text{mix}}}\right) \ln\left(\frac{V+b_{\text{mix}}}{V}\right) + \left(\frac{a_{\text{mix}} b_k}{RT^{1.5} b_{\text{mix}}^2}\right) \times \\ & \left[\ln\left(\frac{V+b_{\text{mix}}}{V}\right) - \left(\frac{b_{\text{mix}}}{V+b_{\text{mix}}}\right)\right] - \ln\left(\frac{PV}{RT}\right) \end{aligned} \quad (6-11)$$

6.3.4 Activity coefficients

Activity coefficients of components in the liquid phase represent the thermodynamic properties of concentrated brine solutions, which are different from those in dilute solutions. Pitzer's model [126], which was derived from Debye-Huckel's method, is used to calculate the activity of water, and activity coefficients of cations, anions and neutral species in the solution. The third-order virial terms are neglected in this model due to their small contributions.

$$\begin{aligned} \phi - 1 = & \left(\frac{2}{\sum_i m_i}\right) \cdot \left[\frac{-A^\phi I^{3/2}}{1+1.2I^{1/2}} + \sum_{c=1}^{N_c} \sum_{a=1}^{N_a} m_c m_a (B_{ca}^\phi + ZC_{ca}) + \sum_{c=1}^{N_c-1} \sum_{c'=c+1}^{N_c} m_c m_{c'} (\Phi_{cc'}^\phi + \sum_{a=1}^{N_a} m_a \psi_{cc'a})\right. \\ & \left. + \sum_{a=1}^{N_a-1} \sum_{a'=a+1}^{N_a} m_a m_{a'} (\Phi_{aa'}^\phi + \sum_{c=1}^{N_c} m_c \psi_{aa'c}) + \sum_{n=1}^{N_n} \sum_{a=1}^{N_a} m_n m_a \lambda_{na} + \sum_{n=1}^{N_n} \sum_{c=1}^{N_c} m_n m_c \lambda_{nc}\right] \end{aligned} \quad (6-12)$$

The activity of water is:

$$a_{\text{H}_2\text{O}} = \exp\left(-\frac{M_{\text{H}_2\text{O}} \cdot \phi}{1000} \cdot \sum_j m_j\right) \quad (6-13)$$

Activity coefficients of other species are calculated by:

$$\begin{aligned} \ln \gamma_M = & z_M^2 F + \sum_{a=1}^{N_a} m_a (2B_{Ma} + ZC_{Ma}) + \sum_{c=1}^{N_c} m_c (2\Phi_{Mc} + \sum_{a=1}^{N_a} m_a \psi_{Mca}) + \sum_{a=1}^{N_a-1} \sum_{a'=a+1}^{N_a} m_a m_{a'} \psi_{aa'M} \\ & + |z_M| \left| \sum_{c=1}^{N_c} \sum_{a=1}^{N_a} m_c m_a C_{ca} + \sum_{n=1}^{N_n} m_n (2\lambda_{nM}) \right| \end{aligned} \quad (6-14)$$

$$\begin{aligned} \ln \gamma_X = & z_X^2 F + \sum_{c=1}^{N_c} m_c (2B_{cX} + ZC_{cX}) + \sum_{a=1}^{N_a} m_a (2\Phi_{Xa} + \sum_{c=1}^{N_c} m_c \psi_{Xac}) + \sum_{c=1}^{N_c-1} \sum_{c'=c+1}^{N_c} m_c m_{c'} \psi_{cc'X} \\ & + |z_X| \left| \sum_{c=1}^{N_c} \sum_{a=1}^{N_a} m_c m_a C_{ca} + \sum_{n=1}^{N_n} m_n (2\lambda_{nX}) \right| \end{aligned} \quad (6-15)$$

$$\ln \gamma_N = \sum_{n=1}^{N_n} m_n (2\lambda_{Nn}) + \sum_{c=1}^{N_c} m_c (2\lambda_{Nc}) + \sum_{a=1}^{N_a} m_a (2\lambda_{Na}) \quad (6-16)$$

where ϕ is the osmotic coefficient of water, γ_M , γ_X and γ_N are activity coefficients for cations, anions and neutral species, respectively, a and c represent anions and cations, respectively, $M_{\text{H}_2\text{O}}$ is molecular weight of water, β and C are Pitzer parameters, and can be found in Table 6.1, the second virial coefficients, λ_{ni} , represents the interactions

between ions and neutral species, and ψ_{ijk} for each cation-cation-anion and anion-anion-cation triplet can be found in Table 6.2 and 6.3, respectively.

Table 6.1 List of β and C Pitzer parameters.

$\beta^{(0)}, \beta^{(1)}, \beta^{(2)}$ and C^ϕ	Reference
Na ⁺ -Cl ⁻	[127]
Na ⁺ -HCO ₃ ⁻	[128]
Na ⁺ -CO ₃ ²⁻	[128]
Na ⁺ -OH ⁻	[129]
Na ⁺ -SO ₄ ²⁻	[130]
H ⁺ -Cl ⁻	[131]
H ⁺ -SO ₄ ²⁻	[132]
Ca ²⁺ -Cl ⁻	[130], [133]
Ca ⁺ -OH ⁻	[133]
Ca ⁺ -SO ₄ ⁻	[130], [134]

Table 6.2 The λ term for neutral species relevant to this model.

λ	Reference
CO ₂ -CO ₂	[135]
CO ₂ -Na ⁺	[135]
CO ₂ -Ca ²⁺	[122]
CO ₂ -Cl ⁻	[136]
CO ₂ -HCO ₃ ⁻	[135]
CO ₂ -CO ₃ ²⁻	[135]
CO ₂ -SO ₄ ²⁻	[134]

- I is the ionic strength and is calculated as

$$I = \frac{1}{2} \sum_i m_i z_i^2 \quad (6-17)$$

$$Z = \sum_i m_i |z_i| \quad (6-18)$$

where z_i is charge of species.

Table 6.3 The ψ term for three-ion interaction relevant to this model.

ψ	Reference
Na ⁺ -H ⁺ -Cl ⁻	[137]
Na ⁺ -Cl ⁻ -HCO ₃ ⁻	[138]
Na ⁺ -Cl ⁻ -CO ₃ ²⁻	[139]
Na ⁺ -Cl ⁻ -OH ⁻	[137]
Na ⁺ -HCO ₃ ⁻ -CO ₃ ²⁻	[132]
Na ⁺ -HCO ₃ ⁻ -OH ⁻	[140]
Na ⁺ -CO ₃ ²⁻ -OH ⁻	[140]
Na ⁺ -Ca ²⁺ -Cl ⁻	[130]
Na ⁺ -Ca ²⁺ -OH ⁻	[122]
Na ⁺ -Ca ²⁺ -SO ₄ ²⁻	[130]
Na ⁺ -H ⁺ -SO ₄ ²⁻	[141]
Na ⁺ -Cl ⁻ -SO ₄ ²⁻	[130]
Na ⁺ -HCO ₃ ⁻ -SO ₄ ²⁻	[132]
Na ⁺ -OH ⁻ -SO ₄ ²⁻	[132]
Na ⁺ -CO ₃ ²⁻ -SO ₄ ²⁻	[140]
Ca ²⁺ -H ⁺ -Cl ⁻	[133]
Ca ²⁺ -Cl ⁻ -OH ⁻	[133]
Ca ²⁺ -Cl ⁻ -SO ₄ ²⁻	[130]
Ca ²⁺ -H ⁺ -OH ⁻	[133]
Ca ²⁺ -H ⁺ -SO ₄ ²⁻	[133]
Ca ²⁺ -SO ₄ ²⁻ -OH ⁻	[133]

- Debye-Huckel limiting slope is defined as:

$$A^\phi = \left(\frac{1}{3}\right)(2\pi N_o d_w)^{1/2} \left(\frac{e^2}{4\pi\epsilon\epsilon_0 kT}\right)^{3/2} \quad (6-19)$$

where N_o is Avogadro's number, d_w is the density of the solvent, k is Boltzmann's constant, ϵ is the dielectric constant or the relative permittivity of water, and ϵ_0 is the

permittivity of free space. Both density of water and dielectric constant can be found in Appendix B.

- Parameter F in Eq. (6-12) is expressed as:

$$F = -A^\phi \left[\frac{I^{1/2}}{1+1.2I^{1/2}} + \frac{2}{1.2 \ln(1+I^{1/2})} + \sum_{c=1}^{N_c} \sum_{a=1}^{N_a} m_c m_a B'_{ca} + \sum_{c=1}^{N_c-1} \sum_{c'=c+1}^{N_c} m_c m_{c'} \Phi'_{cc'} + \sum_{a=1}^{N_a-1} \sum_{a'=a+1}^{N_a} m_a m_{a'} \Phi'_{aa'} \right] \quad (6-20)$$

where the ionic strength dependence of the second virial coefficient, B_{MX}^ϕ , is described as:

$$B_{MX}^\phi = \beta_{MX}^{(0)} + \beta_{MX}^{(1)} e^{-\alpha_1 \sqrt{I}} + \beta_{MX}^{(2)} e^{-\alpha_2 \sqrt{I}} \quad (6-21)$$

The parameters $\beta_{MX}^{(0)}$, $\beta_{MX}^{(1)}$ and $\beta_{MX}^{(2)}$ are specific to the electrolytes. Generally, for 1-1, 1-2 and 2-1 types of electrolytes (or in other words, either cation M or anion X is univalent), $\alpha_1 = 2.0 \text{ kg}^{1/2}$, and $\beta_{MX}^{(2)} = 0 \text{ kg}^{1/2}$ for most cases. For 2-2 type electrolytes (or higher valence pairs), $\alpha_1 = 1.4 \text{ kg}^{1/2}$, $\alpha_2 = 12.0 \text{ kg}^{1/2}$.

$$B_{MX} = \beta_{MX}^{(0)} + \beta_{MX}^{(1)} g(\alpha_1 I^{1/2}) + \beta_{MX}^{(2)} g(\alpha_2 I^{1/2}) \quad (6-22)$$

$$B'_{MX} = \beta_{MX}^{(1)} g'(\alpha_1 I^{1/2}) + \beta_{MX}^{(2)} g'(\alpha_2 I^{1/2}) \quad (6-23)$$

$$g(x) = \frac{2[1 - (1+x)\exp(-x)]}{x^2} \quad (6-24)$$

$$g'(x) = -2 \frac{[1 - (1 + x + x^2/2)\exp(-x)]}{x^2} \quad (6-25)$$

- The third virial coefficient of a single electrolyte, C_{MX} , is defined as:

$$C_{MX} = C_{MX}^{\phi} / 2\sqrt{|z_M z_X|} \quad (6-26)$$

C_{MX} or C_{MX}^{ϕ} is specific to electrolytes.

- The second virial coefficient that accounts for the interactions between ions with the same sign is given in the following form:

$$\Phi_{ij}^{\phi} = \Phi_{ij} + I\Phi'_{ij} \quad (6-27)$$

$$\Phi_{ij} = \theta_{ij} + {}^E\theta_{ij}(I) \quad (6-28)$$

$$\Phi'_{ij} = {}^E\theta'_{ij}(I) \quad (6-29)$$

where θ_{ij} is a single parameter for each pair of anions or cations, and the source is shown in Table 6.4. Functions ${}^E\theta_{ij}(I)$ and ${}^E\theta'_{ij}(I)$ refer to the electrostatic unsymmetrical mixing effects, and depend on ionic strength and the type of electrolyte pair. When ions i and j are of the same charge, ${}^E\theta_{ij}(I)$ and ${}^E\theta'_{ij}(I)$ are zero, else they can be expressed as [142]:

$${}^E\theta_{ij}(I) = \frac{z_i z_j}{4I} (J(X_{ij}) - \frac{1}{2}J(X_{ii}) - \frac{1}{2}J(X_{jj})) \quad (6-30)$$

$${}^E\theta'_{ij}(I) = \frac{z_i z_j}{8I^2} (J'(X_{ij}) - \frac{1}{2}J'(X_{ii}) - \frac{1}{2}J'(X_{jj})) - \frac{{}^E\theta_{ij}(I)}{I} \quad (6-31)$$

$$X_{ij} = 6z_i z_j A^\phi \sqrt{I} \quad (6-32)$$

$$J(x) = \frac{1}{4}x - 1 + \frac{1}{x} \int_0^\infty [1 - \exp(-\frac{x}{y})e^{-y}]y^2 dy \quad (6-33)$$

$$J'(x) = \frac{1}{4}x - \frac{1}{x} \int_0^\infty [1 - (1 + \frac{x}{y}e^{-y})\exp(-\frac{x}{y}e^{-y})]y^2 dy \quad (6-34)$$

Table 6.4 The θ_{ij} term for same-charge ion interaction relevant to this model.

θ_{ij}	Reference
Na ⁺ -H ⁺	[137]
Na ⁺ -Ca ²⁺	[130]
H ⁺ -Ca ²⁺	[133]
Cl ⁻ -HCO ₃ ⁻	[138]
Cl ⁻ -CO ₃ ²⁻	[138]
Cl ⁻ -OH ⁻	[137]
Cl ⁻ -SO ₄ ²⁻	[130]
HCO ₃ ⁻ -CO ₃ ²⁻	[140]
CO ₃ ²⁻ -OH ⁻	[140]
CO ₃ ²⁻ -SO ₄ ²⁻	[132]
OH ⁻ -SO ₄ ²⁻	[143]

6.4 Electrochemical model

6.4.1 Electrochemical reactions

The corrosion reactions under supercritical CO₂ conditions are identical to those occurring under normal conditions. The iron oxidation is the anodic reaction, and

cathodic reactions include the reduction of proton and carbonic acid. The anodic and cathodic current densities, according to Tafel equations, are:

$$i_{a,j} = \varepsilon i_{a,j}^0 \times 10^{\frac{E - E_{arev,j}}{b_{a,j}}} \quad (6-35)$$

$$i_{c,j} = \varepsilon i_{c,j}^0 \times 10^{\frac{-E + E_{crev,j}}{b_{c,j}}} \quad (6-36)$$

where $i_{a,j}^0$ and $i_{c,j}^0$ are the anodic and cathodic exchange current densities, respectively, A/m²; E is the corrosion potential, V; $E_{arev,j}$ and $E_{crev,j}$ are the anodic and cathodic reversible potentials, respectively, V; and $b_{a,j}$ and $b_{c,j}$ are the anodic and cathodic Tafel slopes, respectively, V/dec.

The exchange current density depends on the surface concentrations, C , of the species involved in electrochemical reactions and temperature, and can be calculated by:

$$i^0 = i_{0ref} \left(\frac{C_{H^+}}{C_{H^+ref}} \right)^{a_1} \left(\frac{C_{CO_2}}{C_{CO_2ref}} \right)^{a_2} \left(\frac{C_{H_2CO_3}}{C_{H_2CO_3ref}} \right)^{a_3} \times e^{\frac{-\Delta H}{R} \left(\frac{1}{T} - \frac{1}{T_{ref}} \right)} \quad (6-37)$$

where the values of i_{0ref} , a_1 , a_2 , a_3 , T_{ref} , E_{rev} and b for each reaction can be found in Table 6.5.

Table 6.5 Electrochemical parameters of anodic and cathodic reactions included in the model [29, 97, 144, 145].

		H ₂ CO ₃ reduction	H ⁺ reduction	Fe oxidation
$i_{0\text{ref}}$	$\frac{\text{A}}{\text{m}^2}$	0.018	0.03	1
a_1		-0.5	0.5	1 for $P_{\text{CO}_2} < 1$ bar; 0 for $P_{\text{CO}_2} = 1$ bar
$C_{\text{H}^+\text{ref}}$	mol/L	10^{-4}	10^{-4}	10^{-4}
a_2		0	0	2 for pH<4; 1 for 4<pH<5; 0 for pH>5;
$C_{\text{CO}_2\text{ref}}$	mol/L	N/A	N/A	0.0366
a_3		1	0	0
$C_{\text{H}_2\text{CO}_3\text{ref}}$	mol/L	10^{-4}	N/A	N/A
ΔH	J/mol	50,000	30,000	37,500
T_{ref}	K	293.15	293.15	298.15
E_{rev}	V	$-\frac{2.303RT}{F}\text{pH}$	$-\frac{2.303RT}{F}\text{pH}$	-0.488
b	V	$\frac{2.303RT}{0.5F}$	$\frac{2.303RT}{0.5F}$	$\frac{2.303RT}{1.5F}$

Note: ΔH is the activation energy and T_{ref} is the reference temperature.

For a spontaneous corrosion process, the potential of the steel, E , can be calculated from the charge balance equation on the steel surface by:

$$\sum_i^{n_a} i_a = \sum_i^{n_c} i_c \quad (6-38)$$

where n_a and n_c are the total number of anodic and cathodic reactions, respectively.

The corrosion rate, CR (mm/year), is determined with the rearrangement of Faraday's law as:

$$CR = \frac{i_{\text{Fe}}}{2F} \frac{M_{\text{Fe}}}{\rho_{\text{Fe}}} \times 3600 \times 24 \times 365 = 1.16 i_{\text{Fe}} \quad (6-39)$$

where M_{Fe} is the molecular weight of iron, and ρ_{Fe} is the density of iron.

6.4.2 Mass transfer model

Eqs. (2-26) and (2-27) are used to describe the mass transport of species in the water film. Under CO_2 storage conditions, the water film is usually stagnant. Thus, the convection is negligible. In addition, electro-migration is also neglected due to its small contribution to the overall flux of species [55]. The electroneutrality equation is used as:

$$\sum_{j=1}^n C_j z_j = 0 \quad (6-40)$$

The molecular diffusion coefficient of different species is shown in Table 6.6. Note that the values are for the reference temperature 298.15 K. Eq. (6-41) can be used for correction of the coefficients at other temperatures by:

$$D_j = D_{j\text{ref}} \frac{T_k}{T_{\text{ref}}} \frac{\mu_{\text{H}_2\text{Oref}}}{\mu_{\text{H}_2\text{O}}} \quad (6-41)$$

where $\mu_{\text{H}_2\text{Oref}} = 8.9 \times 10^{-4} \text{ m}^2/\text{s}$ at the reference temperature of 298.15 K, and $\mu_{\text{H}_2\text{O}}$ is calculated as:

$$\mu_{\text{H}_2\text{O}} = \mu_{\text{H}_2\text{Oref}} 10^{\frac{1.3272(298.15-T_k) - 0.001053(298.15-T_k)^2}{T_k - 105}} \quad (6-42)$$

Table 6.6 Molecular diffusion coefficient of species included in the model (298.15 K).

D_{iref}	Diffusion coefficient (m^2/s)	Reference
CO_2	1.96×10^{-9}	[146]
H_2CO_3	2.00×10^{-9}	[147]
HCO_3^-	1.105×10^{-9}	[76]
CO_3^{2-}	0.92×10^{-9}	[147]
H^+	9.312×10^{-9}	[76]
OH^-	5.26×10^{-9}	[76]
Cl^-	2.032×10^{-9}	[76]
HSO_4^-	1.33×10^{-9}	[76]
SO_4^{2-}	1.065×10^{-9}	[76]
Na^+	1.334×10^{-9}	[76]
Fe^{2+}	0.72×10^{-9}	[147]
Ca^{2+}	0.792×10^{-9}	[76]

The overall species conservation equation can be rewritten as:

$$\frac{\partial(\varepsilon C_j)}{\partial t} - D_j \frac{\partial^2(\varepsilon^{1.5} C_j)}{\partial x^2} = \varepsilon R_j \quad (6-43)$$

For the chemical reactions listed above, the generation/consumption rate of species j , R_j , is calculated from the forward and backward reaction rate constants and the concentration of the involved species. It is found that the net change of bicarbonate ions and carbonate ions is larger than that of CO_2 due to their larger forward and backward reaction rate constants [19]. The net change rate of CO_2 and H_2CO_3 are considered as [22]:

$$R_{\text{CO}_2} = -k_{\text{f,hy}} C_{\text{CO}_2} + k_{\text{b,hy}} C_{\text{H}_2\text{CO}_3} \quad (6-44)$$

$$R_{\text{H}_2\text{CO}_3} = k_{\text{f,hy}} C_{\text{CO}_2} - k_{\text{b,hy}} C_{\text{H}_2\text{CO}_3} \quad (6-45)$$

where $k_{\text{f,hy}}$ and $k_{\text{b,hy}}$ are the forward and backward CO_2 hydration rate constants, respectively.

6.4.3 Formation of corrosion scale

When the product of concentrations of Fe^{2+} and CO_3^{2-} exceed the solubility limit (K_{spFeCO_3}) of FeCO_3 , solid FeCO_3 starts to precipitate on the steel surface. The precipitation rate is temperature and pH dependent, and is expressed by [89]:

$$R_{\text{FeCO}_3} = k_{\text{fFeCO}_3} \sigma K_{\text{spFeCO}_3} (S_{\text{FeCO}_3} - 1) \quad (6-46)$$

where σ is the ratio of surface area over the volume of the precipitate, and is set to be 10^5 m^{-1} [57]; $S_{\text{FeCO}_3} = C_{\text{Fe}^{2+}} C_{\text{CO}_3^{2-}} / K_{\text{spFeCO}_3}$ is the supersaturation of FeCO_3 ; and k_{FeCO_3} is the rate constant, and is expressed by [89]:

$$k_{\text{FeCO}_3} = e^{\frac{28.2 - 64851.4}{RT_k}} \quad (6-47)$$

The precipitation process is considered to be irreversible, and the precipitation rate is rewritten as [148]:

$$R_{\text{FeCO}_3} = \max(0, R_{\text{FeCO}_3}) \quad (6-48)$$

The volumetric porosity ε describes the morphology of the scale, and can be expressed as:

$$\varepsilon = \frac{V_{\text{void}}}{V_{\text{total}}} = \frac{(1 - V_{\text{total}})}{V_{\text{total}}} = 1 - \frac{C_{\text{FeCO}_3} \times M_{\text{FeCO}_3}}{\rho_{\text{FeCO}_3}} \quad (6-49)$$

where M_{FeCO_3} is the molecular weight of FeCO_3 , 115.8 kg/kmol; and ρ_{FeCO_3} is FeCO_3 density, 3900 kg/m³. The variation of the volumetric porosity with time, for any space in the system, can be expressed as:

$$\frac{\partial \varepsilon}{\partial t} = -\frac{M_{\text{FeCO}_3}}{\rho_{\text{FeCO}_3}} R_{\text{FeCO}_3} \quad (6-50)$$

6.5 Modelling solutions

6.5.1 Initial and boundary conditions

When corrosion of a steel achieves an equilibrium state, chemical reactions and the reaction equilibrium constants in Eqs. (2-1), (5-1) and (6-1) ~ (6-5) are combined with the electroneutrality equation (Eq. (6-40)) to calculate the activities of all species. The activity of H^+ is used to determine the solution pH by:

$$\text{pH} = -\log a_{\text{H}^+} = -\log(\gamma_{\text{H}^+} \times C_{\text{H}^+}) \quad (6-51)$$

The activities of all involved species are used as the initial conditions, assuming that the activities are uniform in the solution. At the liquid/gas interface, the boundary conditions are different for individual species. The CO_2 concentration is constant, and can be determined by the equilibrium constants mentioned above. For other species, a zero-flux boundary condition is applied.

On the steel surface, for the species that are not involved in electrochemical reactions, a zero flux ($N_j=0$) is applied. For those participating in the electrochemical reactions, i.e. H^+ , H_2CO_3 , Fe^{2+} , etc., the flux on the steel surface can be determined by:

$$N_j = \frac{i_j}{n_j F} \quad (6-52)$$

where n_j is the number of moles of electrons exchanged per mole of species j .

6.5.2 Numerical methods

For the chemical/electrochemical reactions, the boundary conditions and the scale formation equation are nonlinearly coupled. They should be solved simultaneously and continuously. The finite difference method (FDM) is used to solve the unsteady ordinary and partial differential equations, with non-uniform space interval grids created for the one-dimensional model. For Eq. (6-43), the central implicit scheme is used as:

$$\varepsilon_i \frac{c_{j,i}^{n+1} - c_{j,i}^n}{\Delta t} \Delta x_i = \varepsilon_i^{1.5} \frac{(c_{j,i+1}^{n+1} - c_{j,i}^{n+1})}{0.5(\Delta x_{i+1} + \Delta x_i)} - \varepsilon_i^{1.5} \frac{(c_{j,i}^{n+1} - c_{j,i-1}^{n+1})}{0.5(\Delta x_i + \Delta x_{i-1})} + \varepsilon_i R_{j,i}^{n+1} \Delta x_i \quad (6-53)$$

where Δt is the time increment, $n+1$ and n represent new and old points, respectively, Δx_i is the size of grid i , and Δx_{i+1} and Δx_{i-1} are the sizes of grids adjacent to grid i . If the precipitation of FeCO_3 is considered, a negative R_{FeCO_3} is added to Eq. (6-53) for Fe^{2+} .

For CO_3^{2-} , the flux on the steel surface also has a negative R_{FeCO_3} .

A comprehensive MATLAB code is written based on the developed water chemistry sub-model and electrochemical corrosion sub-model, coupled with mass-transfer equations and the scale formation equation. This enables calculation of corrosion rate of the steel under CO_2 storage conditions. The modelling results and the model validation are described as follows.

6.6 Water chemistry sub-modelling results and validation

In order to model the corrosion of steel in CO₂ storage, the water chemistry associated with the corrosion process must be determined. This includes the concentrations (activities actually) of species existing in the solution. Particularly, the species' concentrations are used as the initial or boundary conditions for the modelling calculation. As hydrogen ions are involved in many chemical reactions, the concentrations of the relevant species can be represented by the H⁺ concentration. As noted in Eq. (6-51), the solution pH is used as to quantify the concentration of H⁺. Determination of the pH is the vital step to accurately predict corrosion rate of the steel under specific water chemistry conditions.

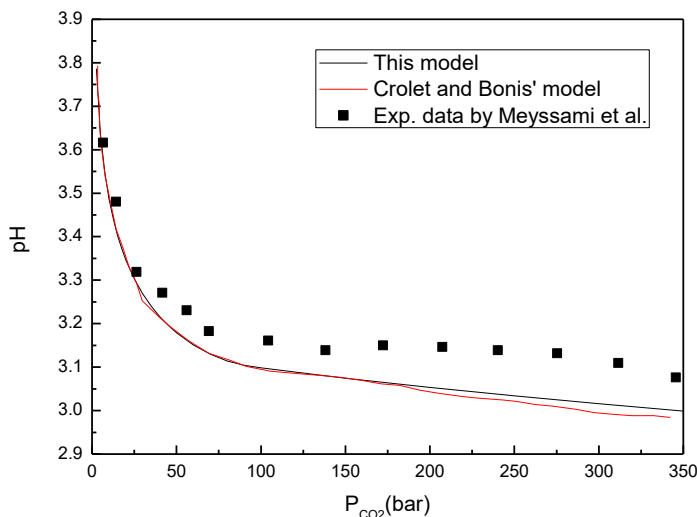


Figure 6.2. Solution pH calculated from the developed model as a comparison with published data Crolet and Bonis [149], Meyssami et al. [150] at 42 °C and various CO₂ partial pressures.

The developed water chemistry sub-model is validated by the published data. It is realized that there are just a few publications containing pH data under high pressure and high temperature CO₂ conditions. Figure 6.2 shows the calculated solution pH from the developed model as a comparison with published data at 42 °C and various CO₂ partial pressures. It is seen that, with the increase of the CO₂ partial pressure, the solution pH decreases rapidly first. When the CO₂ partial pressure is over 50 bar, the pH drops slowly and reaches a relatively steady value. The model accurately predicts this trend. Moreover, the modelling pH data are very close to the testing ones.

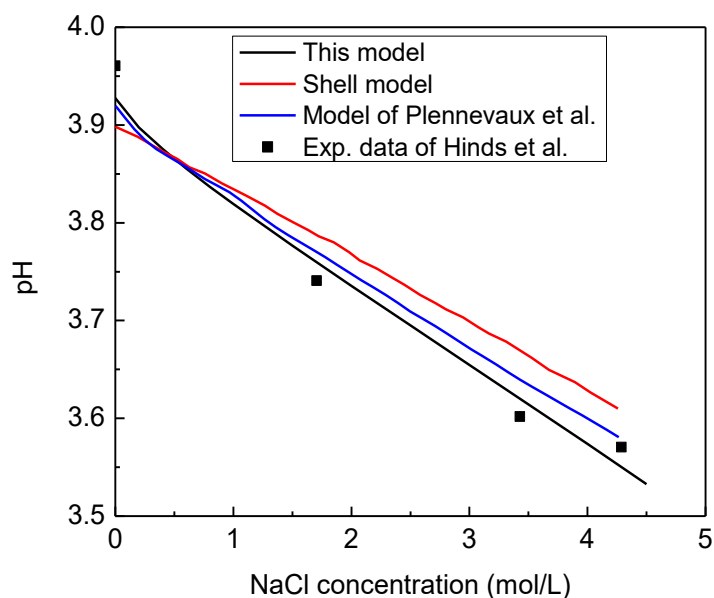


Figure 6.3 Solution pH obtained from the developed model as a function of NaCl concentration at 25 °C under 1 bar CO₂.

Since the solution salinity affects the solubility of CO₂ in solutions and thus the solution pH, the variation of solution pH as a function of various NaCl concentrations at 25 °C under 1 bar CO₂ is modelled, and the results are shown in Figure 6.3, where some published data are present for comparison [151, 152]. It is seen that the pH decreases with the increasing NaCl concentration. Compare to the other two published models, this model gives the best prediction to the experimental data.

Furthermore, the modelling pH results are compared with the data from Duan and Li [122] over a wide CO₂ pressure range at 77 °C in Figure 6.4. It is seen that the results obtained from the developed model almost copy with those published.

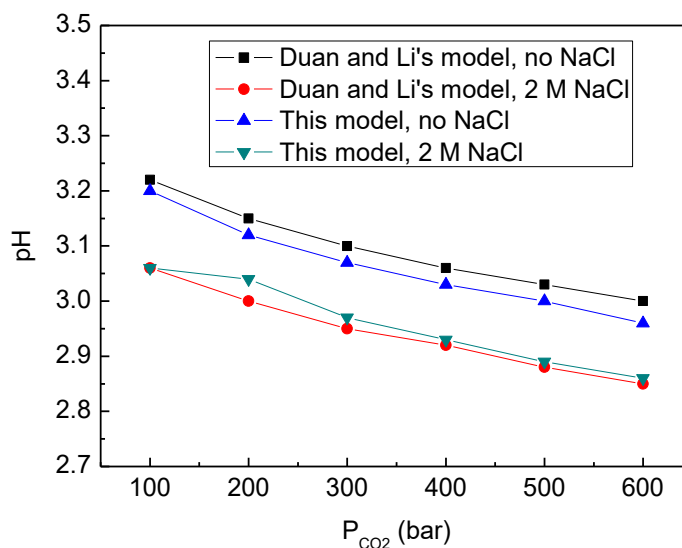


Figure 6.4 Modelling pH results are compared with the data from Duan and Li [122] over a wide CO₂ pressure range at 77 °C.

In summary, the developed water chemistry sub-model is able to determine the pH of solutions generated under supercritical CO₂ storage conditions. Moreover, the modelling results are confirmed by the published data for validation purpose.

6.7 Electrochemical sub-modelling results and validation

6.7.1 Modelling and validation of corrosion rate of steels

Figure 5.5 shows the comparison of the predicted corrosion rates by the developed model with data from the experimental work and published literature under supercritical CO₂ conditions. For the experimental work, the testing solution is 1.8 g/L NaCl solution. The testing temperatures are 30 °C, 60 °C, 90 °C, and 120 °C, and the pressures are 0.3 MPa, 1.4 MPa, and 7.5 MPa. The testing period is 5 days. The published results were obtained under different corrosive conditions. When the corrosion rate is obtained from the developed model, the input conditions are kept identical to those where the tests were conducted. It is seen that the modelling results are relatively consistent with those obtained in the experiments and from the published literature, demonstrating the reliability of the developed model in corrosion prediction under supercritical CO₂ conditions.

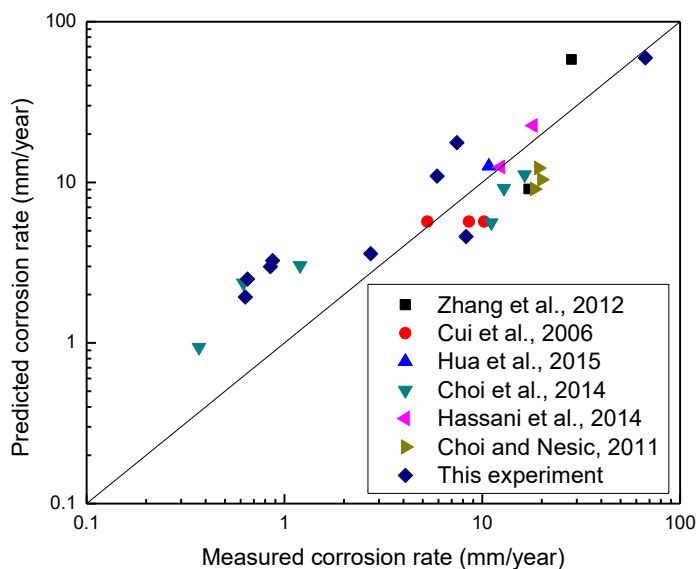


Figure 6.5 Comparisons of the predicted corrosion rates by the developed model with data from the experimental testing and published literature (Cui et al. [153], Zhang et al. [42], Choi and Nestic [125], Choi et al. [154], Hassani et al. [155] and Hua et al. [156]) under supercritical CO₂ conditions.

6.7.2 Effect of the solution layer thickness on corrosion of the steel

It has been confirmed [148] that a thick diffusive boundary layer of the solution results in a small corrosion rate due to increased resistance to mass transport. Without knowledge of the solution layer thickness, the prediction of corrosion rate does not make sense, at least theoretically. Figure 6.6 shows the dependence of the corrosion rate on the solution layer thickness at 80 °C and 10 bar and 95 bar CO₂ partial pressures, respectively. It is seen that, as the solution layer becomes thicker, the corrosion rate decreases. When the solution layer is over 1 cm in thickness, the corrosion rates keeps

approximately constant. Thus, a critical thickness of the solution layer exists, above which the corrosion rate alters slightly. This phenomenon is attributed to the fact that corrosion would not be affected by the solution layer thickness if it exceeds the thickness of the diffusive boundary layer, where the diffusion and concentration gradients of corrosive species determine the corrosion rate of the steel. Thus, the critical solution thickness refers to the thickness that corrosive species in the solution have the initial equilibrium concentration before the corrosion reaction starts.

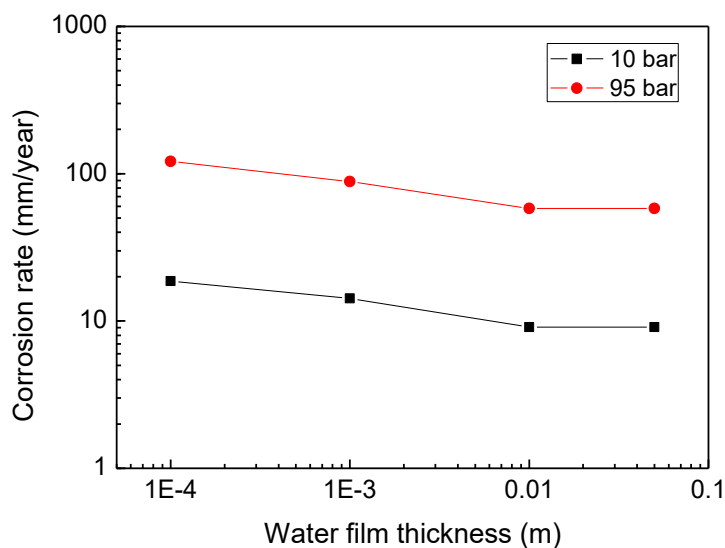


Figure 6.6 Dependence of corrosion rate on the solution layer thickness at 80 °C and 10 bar and 95 bar CO₂ partial pressures, respectively.

To consider the effect of the mass-transfer step of corrosive species on steel corrosion, the solution layer thickness should exceed the critical thickness of the diffusive boundary layer. In this work, a solution layer thickness of 5 cm, which is thicker than the

critical diffusive boundary layer, is chosen for numerical calculation and the corrosion rate modelling.

6.7.3 Effect of temperature on corrosion of the steel

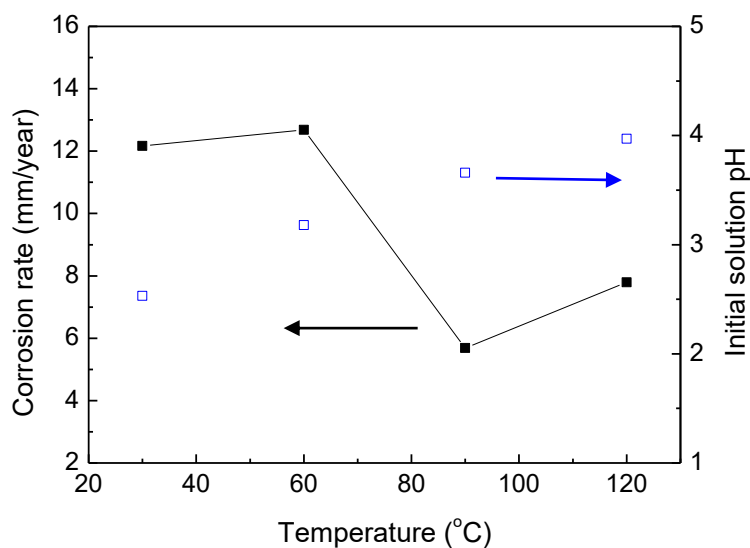


Figure 6.7 Calculated solution pH and corrosion rate as a function of temperature in simulated oilfield produced water (CaCl_2 15 g/L, NaHCO_3 1.1 g/L) at 82.74 bar of CO_2 .

Generally, temperature can affect the corrosion of steel in three aspects. First, with the elevated temperature, the solubility of CO_2 in water decreases, making the solution less acidic. This would decrease the corrosion rate of the steel. Figure 6.7 shows the calculated solution pH as a function of temperature in simulated oilfield produced water (CaCl_2 15 g/L, NaHCO_3 1.1 g/L) at 82.74 bar of CO_2 . Second, an elevated temperature would decrease the reaction energy barrier and enhance the mass transfer of corrosive

species, increasing the corrosion rate. Finally, when a protective scale is formed on the steel surface during corrosion, i.e., FeCO_3 scale in CO_2 corrosion, the increased temperature can reduce the solubility of FeCO_3 and facilitate its precipitation. Thus, the corrosion rate of the steel is reduced remarkably. Obviously, the role of the elevated temperature in steel corrosion is complex, depending on the dominant factors at specific temperature ranges. It can be seen from Figure 6.7 that, when temperature is below 60°C , the corrosion rate increases with the temperature because the corrosion scale formed at this temperature is not protective. At temperatures above 90°C , the scale can protect the steel from corrosion attack. Thus, the corrosion rate at high temperatures is much smaller than that at low temperatures.

6.7.4 Effect of CO_2 partial pressure on corrosion of the steel

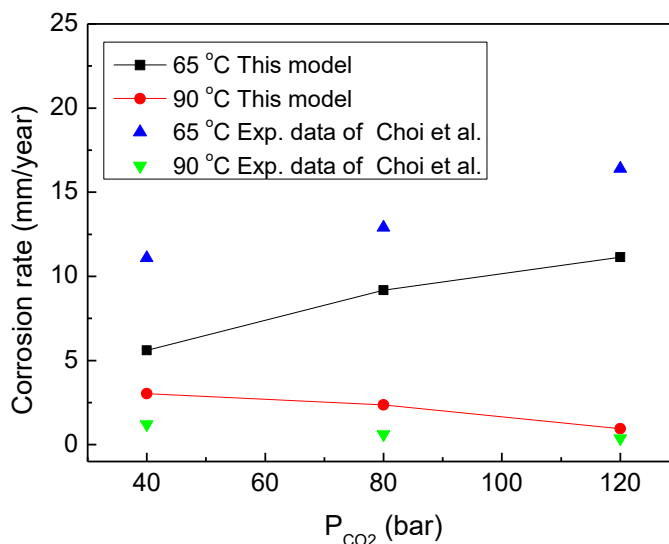


Figure 6.8 Dependence of corrosion rate of the steel on CO₂ partial pressure in 25% NaCl solution, as well as comparison with the published data under this condition (Choi et al. [154]).

Figure 6.8 shows the dependence of corrosion rate of the steel on CO₂ partial pressure in 25% NaCl solution at 65 and 90 °C, as well as the comparison with the published data under this condition [154]. It is seen that, at a relatively low temperature of 65 °C, the corrosion rate increases with the increasing CO₂ partial pressure; while at 90 °C, the corrosion rate decreases as the CO₂ partial pressure is increased. The modelling results are consistent with the experimental data. As analyzed, the results indicate the essential effect of temperature on the corrosion rate of steels via the protectiveness of the formed scale FeCO₃.

A further look at the comparison of the modelling data with the experimental measurements shows that, at 65 °C, there is a big difference between the predicted corrosion rates and the experimental results. The possible reason for this discrepancy is that the corrosion products formed at low-temperatures during CO₂ corrosion also include Fe₃C [154], which has different protective effect on corrosion from FeCO₃. This gives an insight into the improvement of the model for a more accurate prediction.

6.7.5 Time dependence of corrosion rate

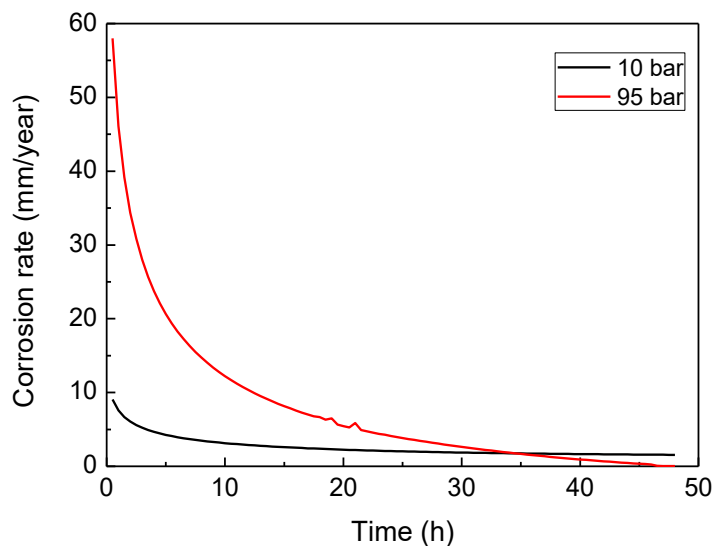


Figure 6.9 Time dependence of corrosion rate of steels in brine water at 80 °C and 10 bar and 95 bar CO₂ partial pressures.

For corrosion systems with a product scale formed on the steel surface, the corrosion rate of the steel usually decreases with time. It is mainly due to the fact that the scale formation is time dependent. Along with time, the scale becomes thicker, more compact and thus more protective, decreasing the corrosion rate. This also applies for supercritical CO₂ corrosion of steels. As shown in Figure 6.9, the time dependence of corrosion rate of the steel in brine water at 80 °C and 10 bar and 95 bar CO₂ partial pressures is modelled. It is seen that the corrosion rate decreases quickly first, and then reaches a relatively steady state gradually. This gives the profile of the corrosion rate in the solution, depending on evolution of corrosion scale with time.

6.7.6 Time dependence of porosity of the corrosion scale

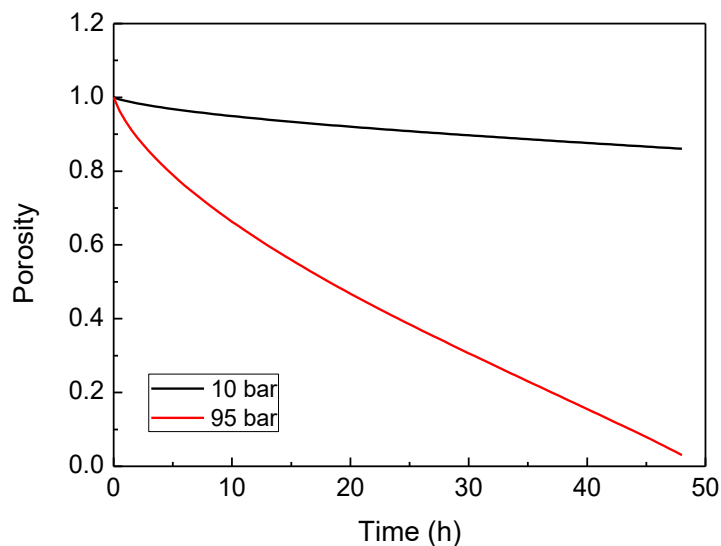


Figure 6.10 Time dependence of the scale porosity under the same condition as that of Figure 6.9.

As modelled above, the corrosion rate of the steel decreases with time, which is due to the improved protectiveness of the scale formed on the steel surface. Porosity is an important indicator of the scale structure, and thus, the protective ability of the scale to corrosion. The time dependence of the scale porosity is modelled under the same condition as that of Figure 6.9, and the results are shown in Figure 6.10. It is seen that, indeed, the porosity of the scale decreases with time at both CO₂ partial pressures. Moreover, there is a smaller porosity for the scale formed at a higher CO₂ partial pressure such as 95 bar than that formed at a lower CO₂ partial pressure, i.e., 10 bar. As analysed above, the dissolved CO₂ causes generation of Fe²⁺ ions, and facilitates precipitation of the FeCO₃ scale.

6.7.7 Distributions of the species concentration in the solution

Under high CO₂ partial pressure conditions, the pH of the bulk solution can be low. However, on the steel surface, both H⁺ and H₂CO₃ are consumed in cathodic reactions. A high pH environment can be generated locally. Figures 6.11 shows the modelled distributions of the concentration of various species in the solution at 80 °C and 10 bar and 95 bar CO₂ partial pressures, respectively. Based on the concentration of H⁺ ions, the pH of the bulk solution, i.e., the solution away from the steel surface, is calculated to be 3.78 and 3.26 at 10 bar and 95 bar CO₂ partial pressures, respectively. Due to the low solution pH, FeCO₃ cannot be formed in the acidic conditions. However, on the steel surface, the solution pH are 5.63 and 5.58 at 10 bar and 95 bar CO₂ partial pressures, respectively. The elevated pH makes it possible to deposit FeCO₃ scale on the steel surface.

Furthermore, it is seen from Figure 6.11 that the concentrations of CO₂, H⁺ and H₂CO₃ are smaller on the steel surface than those in the bulk solution away from the steel. Both H⁺ and H₂CO₃ are consumed in electrochemical cathodic reactions at the steel/solution interface, and the CO₂, upon hydration, is involved in corrosion reactions on the steel surface. The direct corrosion products, HCO₃⁻ and Fe²⁺, are generated on the steel surface. Their concentrations are larger than those in the bulk solution.

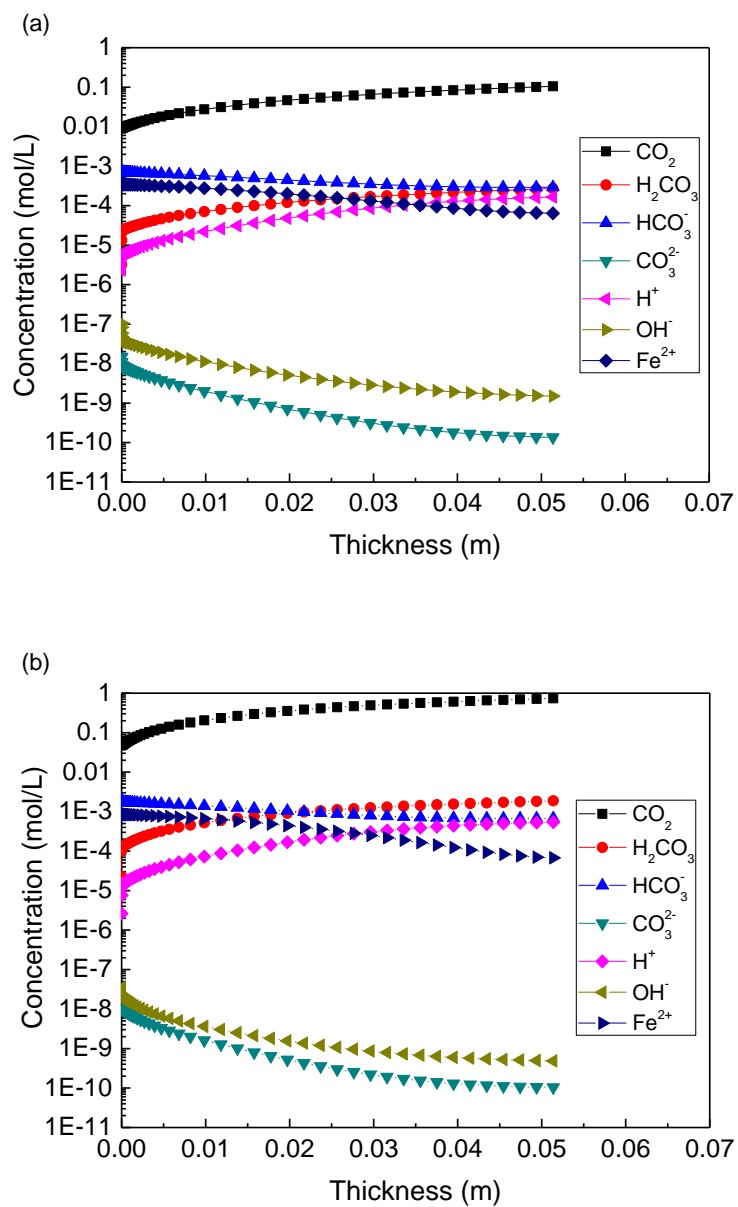


Figure 6.11 Distributions of the concentration of various species in the solution at 80 °C and a) 10 bar, b) 95 bar CO_2 partial pressure.

6.8 Limitations of the model

The reliability and applicability of a developed model rely largely on validation by available data. As stated, there have been so far limited experimental works conducted to investigate corrosion of steels under supercritical CO₂ conditions. Moreover, the published results are scatter and conducted under a wide variety of environmental conditions. Although big efforts have been made to collect the literature data for model validation, there is still a space to have further, complete validations.

The developed model focuses on prediction of the uniform corrosion rate of tubing steel in CO₂ storage. It models the situation that the cement to support the tubing is absent, exposing the tubing steel directly to corrosive environments over a sufficiently big area. However, in reality, another common corrosion scenario is the generation of micro-annulus or crevices in the cement, resulting in localized pitting corrosion occurring on the tubing [154, 156]. Thus, a modification of the model to make it applicable for modelling the local solution chemistry/electrochemistry and enabling the localized corrosion prediction is required.

6.9 Summary

A mechanistic model is developed to predict the corrosion rate of steel under the supercritical CO₂ storage conditions. The model integrates a number of sub-models that quantify various interrelated steps contributing to the steel corrosion. Moreover, the environmental parameters and conditions used are representative of those encountered in CO₂ storage.

The water chemistry sub-model is able to determine the solution pH and the concentration of involved species. To correct the non-ideal environmental conditions, both gas fugacity coefficient and ion activity coefficient are used to quantify the effect of high pressure and high salinity environmental conditions on corrosion. In the electrochemical corrosion sub-model, both charge-transfer and mass-transfer steps and their effect on corrosion are quantified. The scale formation is considered due to its effect on the corrosion rate. The modelled corrosion rates are consistent with the testing and literature results, demonstrating the reliability of the model in corrosion prediction for steel tubing in CO₂ storage. In addition to prediction of the corrosion rate, the model is able to determine the parametric effects, including temperature, CO₂ partial pressure, solution salinity, solution pH, time, etc., on steel corrosion. Moreover, the model enables determination of the effect of corrosion scale and its porosity on steel corrosion. The distribution of the concentrations of various species existing in the solution is also modelled.

There are still spaces to improve the model. These include a complete validation by data obtained under more relevant conditions, and a modification of the model for prediction of localized corrosion.

Chapter Seven: Mechanism of corrosion of X52 pipeline steel in a simulated soil solution

7.1 Introduction

According to a report from AER, the recorded pipelines in Alberta have a distance of 415,512 km, of which about 17% is discontinued or abandoned [8]. When it comes to nationwide and worldwide level, the distance of pipelines to be abandoned can be much higher. Moreover, new pipeline constructions triggered by the increasing oil and gas demands also prompt the increase in abandonment of old pipelines. The integrity management of the abandoned pipelines, which are left in soils, for sake of economic, environmental and social concerns, has become a more and more urgent problem and needs close considerations and research work.

External corrosion of abandoned pipelines happens due to the interaction between pipe steel and the surrounding soil when the applied coating is missed over a certain area. The soil environment remarkably affects the corrosion behavior of abandoned pipelines. Previous studies on corrosion of ferrous metals in soils showed that the soil corrosion of metals can be related to a number of factors, including soil resistivity, dissolved salts, moisture, pH, oxygen concentration, the presence of bacteria, etc. [50]. Differences in the physical property and chemical composition of soils from various places may lead to totally different corrosion behavior and corrosion rates. It is thus important to study pipeline corrosion in a certain soil environment where the pipeline is to be abandoned.

Investigation of corrosion of pipelines steels in simulated soil solutions is a common method to study soil corrosion. It has the advantages of easy to control soil chemistry, solution pH, gas content, etc. [51, 53, 157].

In this work, the corrosion of an abandoned X52 pipeline steel was studied in a soil solution simulating the Regina clay soil. Electrochemical measurements, including OCP, linear polarization resistance (LPR), and potentiodynamic polarization, were conducted to determine the corrosion mechanism and corrosion rate. The microstructure and corrosion morphology were characterized with optical microscopy and SEM. X-ray diffraction (XRD) was used to analyze the composition of corrosion products generated on the steel surface. Parametric effects, including DO concentration, solution pH, Cl^- concentration and testing time, on the steel corrosion were studied and discussed.

7.2 Experimental

7.2.1 Material, specimen and solution

Specimens used in this work were cut from an abandoned X52 steel pipe, with a chemical composition (wt. %): C 0.24%, Si 0.45%, Mn 1.4%, P 0.025%, S 0.015%, V 0.1%, Nb 0.05%, Ti 0.04% and Fe the balance. The specimens were machined into a cubic shape. After sealed in epoxy resin, the specimen has a square working face with an area of 1.0 cm^2 . The specimen was ground consequentially from 120 to 1000 grit emery paper, polished with $1 \mu\text{m}$ diamond pasta, and then rinsed with distilled water and degreased in acetone.

For microstructural characterization, the specimen was etched with 4% nitric acid (ethonal balanced) for 5 s. The optical view of the microstructure of X52 steel is shown

in Figure 7.1. It is seen that the steel mainly consists of polygonal ferrite and pearlite, which is typical of the microstructure of low strength pipeline steels.

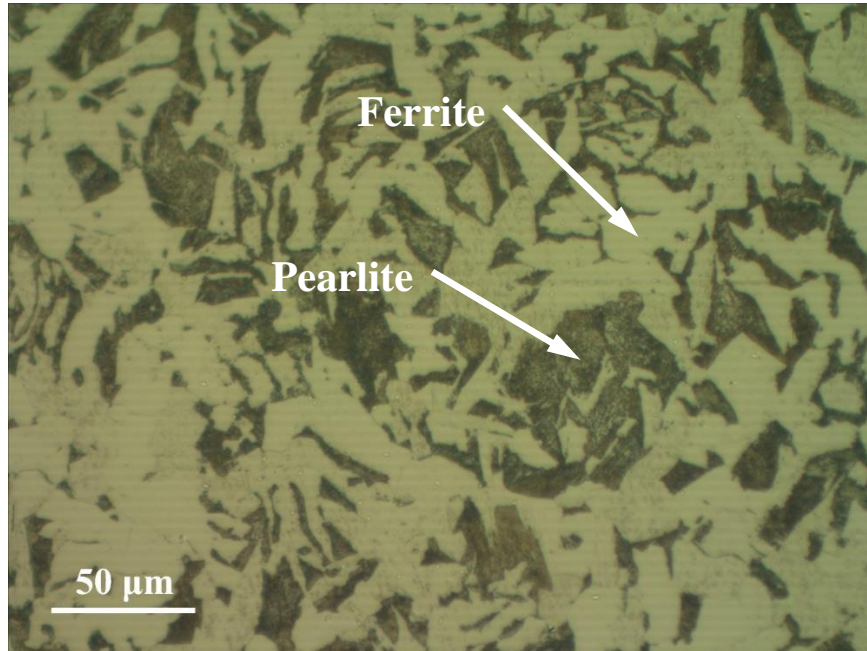


Figure 7.1 Optical view of the microstructure of X52 steel.

The solution used in this work simulated the chemical composition of the Regina clay soil (Table 7.1). The solution was made of analytical grade reagents and deionized water. The base condition was open to air at ambient temperature (22 ± 1 °C). The content of DO was measured with an EXTECH instruments SDL150 oxygen meter, and the value was $7.7 (\pm 0.1)$ mg/L. The pH of the base soil solution was $7.40 (\pm 0.14)$ measured with a pH meter (Oaklon Acorn pH meter). Mixed gases of CO₂ and N₂ were purged into the solution to adjust the solution pH. To study the effect of Cl⁻ concentration on the corrosion behavior, additional NaCl with controlled concentrations was added in the base solution.

Table 7.1 Chemical composition of the simulated Regina soil solution.

Compound	NaHCO ₃	NaNO ₃	NaCl	Na ₂ SO ₄	CaSO ₄ •2H ₂ O	K ₂ SO ₄	MgSO ₄ •7H ₂ O
Concentration (g/L)	0.0755	0.0014	0.0092	0.0773	1.116	0.0619	0.662

7.2.2 Electrochemical measurements

Electrochemical measurements were performed on a three-electrode system, where the steel specimen was used as WE, a carbon rod as CE, and a SCE as RE, using a Gamry Reference 600 electrochemical system. Prior to electrochemical measurements, a steady state OCP of the steel was achieved in the test solution. LPR plots were measured by scanning the potential from -15 mV to +15 mV relative to corrosion potential at a potential sweep rate of 0.1667 mV/s. Potentiodynamic polarization curves were measured by scanning the potential from -500 mV to +500 mV relative to corrosion potential at a potential sweep rate of 0.5 mV/s.

7.2.3 Surface morphology observation and corrosion product composition characterization

The SEM (Model FEI XL 30) was used to characterize the surface morphology of the steel electrodes after various times of immersion in the soil solution. After that, corrosion products were removed carefully from the steel surface by chemical methods, according to ASTM G1-03 [158]. An optical microscope was used to observe the morphology of the steel substrate.

The XRD (Rigaku Multiflex X-ray Diffractometer) was used to characterize the composition of the corrosion products. A range from 20° to 90° was scanned with the step width of 0.02° and the scan rate was $2^{\circ}/\text{min}$.

7.3 Results

7.3.1 Potentiodynamic polarization curve measurements

Potentiodynamic polarization curves of X52 pipeline steel are measured immediately after the OCP becomes stable and after 30 days of immersion in the base soil solution, and the results are shown in Figure 7.2. It is seen that, after the OCP is stable, the steel shows an active dissolution behavior in the anodic curve. There are two transition points, i.e., points a and b, in the cathodic branch. The polarization curve between points a and b shows a diffusive limiting current density, indicating the diffusion controlled cathodic reaction in this potential range. After 30 days of immersion in the solution, the corrosion potential is shifted negatively. There is no diffusive limiting current density in the cathodic branch. A “passivated” behavior can be found in the anodic branch.

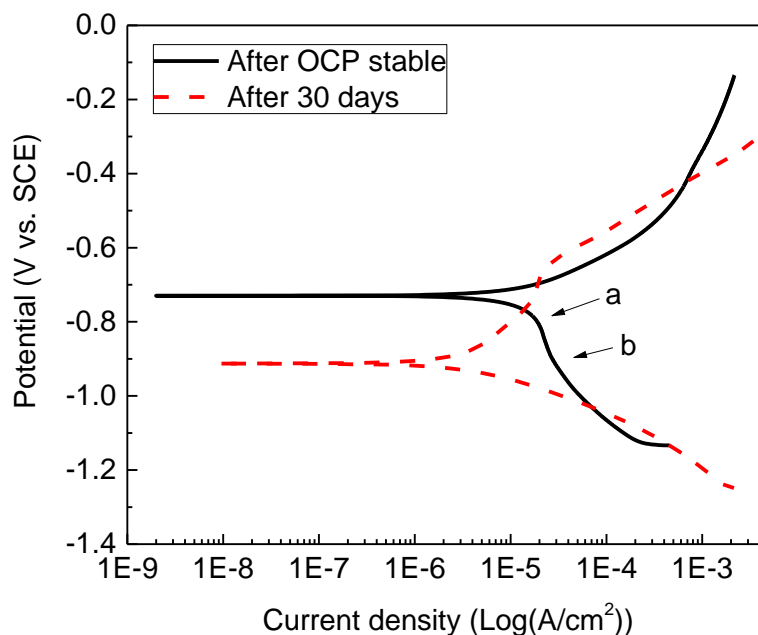


Figure 7.2 Potentiodynamic polarization curves of X52 steel immediately after the OCP becomes stable and after 30 days of immersion in the base soil solution.

Figure 7.3 shows the polarization curves of X52 pipeline steel in the soil solutions with different DO concentrations, i.e., 7.7 ppm (base condition), 3.9 ppm and 0.4 ppm, respectively. It is seen that the corrosion potential is shifted negatively when the DO concentration decreases. In the cathodic branch, the diffusive limiting current density is obvious at a high DO concentration. When the DO concentration is reduced to 0.4 ppm, the limiting diffusive current density is not observed. Moreover, the anodic curves almost overlap each other when the DO concentrations are 7.7 ppm and 3.9 ppm, while a passivation phenomenon is observed at the DO concentration of 0.4 ppm.

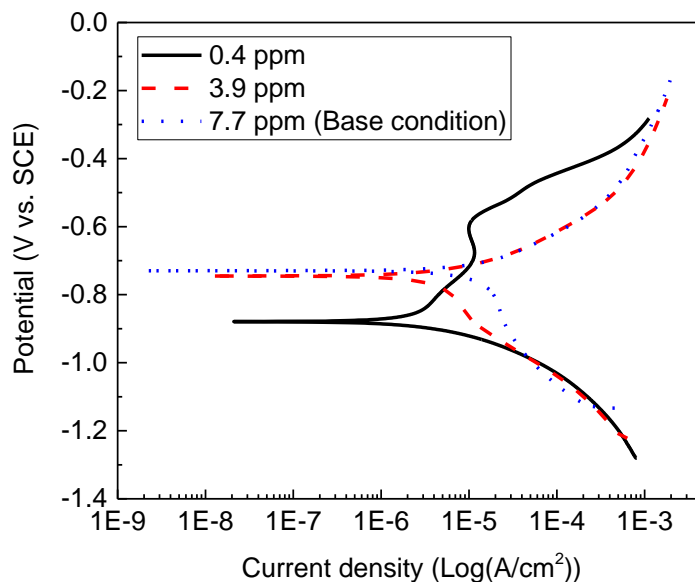


Figure 7.3 Potentiodynamic polarization curves of X52 steel in the soil solution with different DO concentrations.

When the base soil solution is purged with various gasses, the solution pH is measured. The pH values are around 6.21 and 5.77 during bubbling with 5% and 10% CO₂, respectively. The polarization curves of the steel measured in the soil solutions with various pH are shown in Figure 7.4. It is seen that the anodic branch almost copy each other at pH 6.21 and 5.77. When the solution is up to 7.40, the anodic current density decreases at individual potentials. For the cathodic branch, the diffusive limiting current density is found in the base solution with pH 7.40, but is not observed at the other two pH conditions.

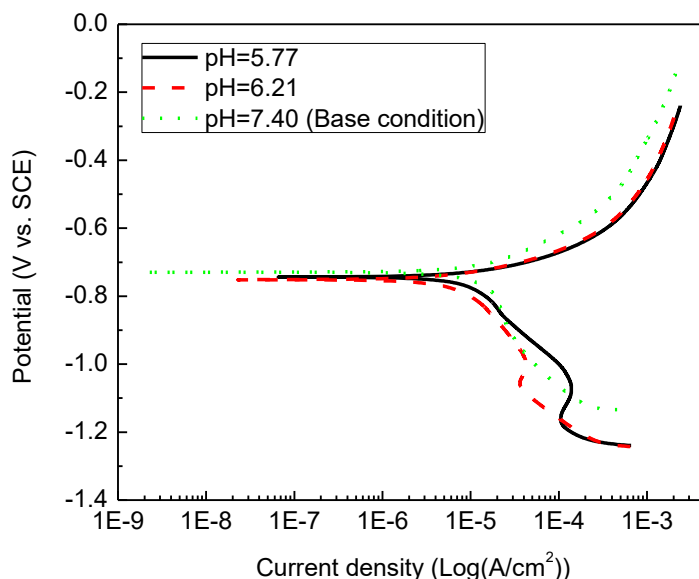


Figure 7.4 Potentiodynamic polarization curves of X52 steel in soil solution with different solution pH values.

Figure 7.5 shows the polarization curves of X52 steel in the soil solutions containing various Cl^- concentrations, i.e., 5 ppm (base condition), 50 ppm, 500 ppm and 5000 ppm, immediately after the OCP becomes stable and after 30 days of immersion in the solution. It is seen that, after the OCP is stable, the steel is in an active dissolution state. The increase in Cl^- concentration would increase the anodic current density, and there is no apparent effect on the cathodic current density. After 30 days of immersion in the solution, the steel becomes passivated at anodic potentials. The anodic current density increases with the increasing Cl^- concentration. However, the cathodic current density is independent of the Cl^- concentration. The corrosion potential of the steel is shifted negatively after 30 days of testing in the solution.

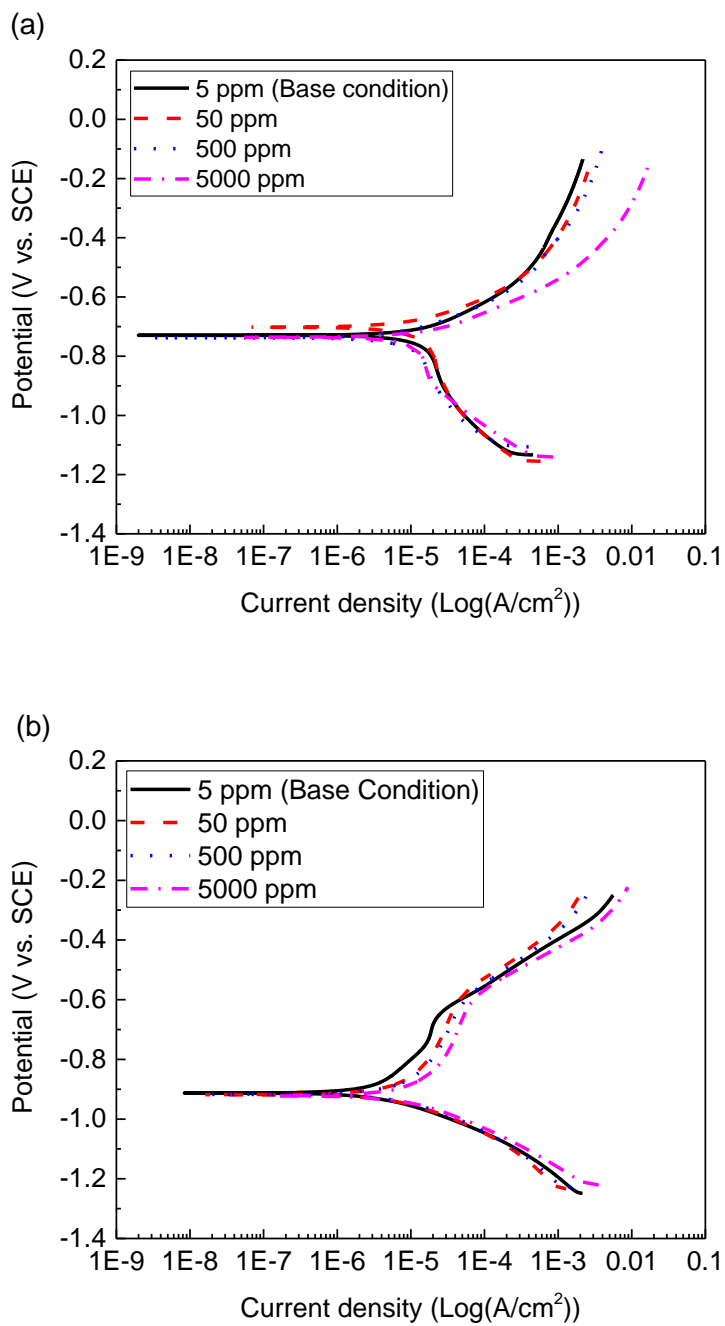


Figure 7.5 Potentiodynamic polarization curves of X52 steel in the soil solutions containing various Cl⁻ concentrations (a) Immediately after the OCP is stable, (b) After 30 days of immersion in the solution.

7.3.2 Open circuit potential and linear polarization resistance measurements

The OCP of X52 steel in the base soil solution as a function of time is shown in Figure 7.6. It is shown that the OCP shifts negatively when immersing in the solution, and becomes gradually stable at around -758 mV (SCE).

Figure 7.7 shows the polarization resistance (R_p) determined from the LPR measurements in the base soil solution. Generally, the R_p increases rapidly first, and gradually tends to be stable around $4000 \Omega \cdot \text{cm}^2$ after 14 days of immersion.

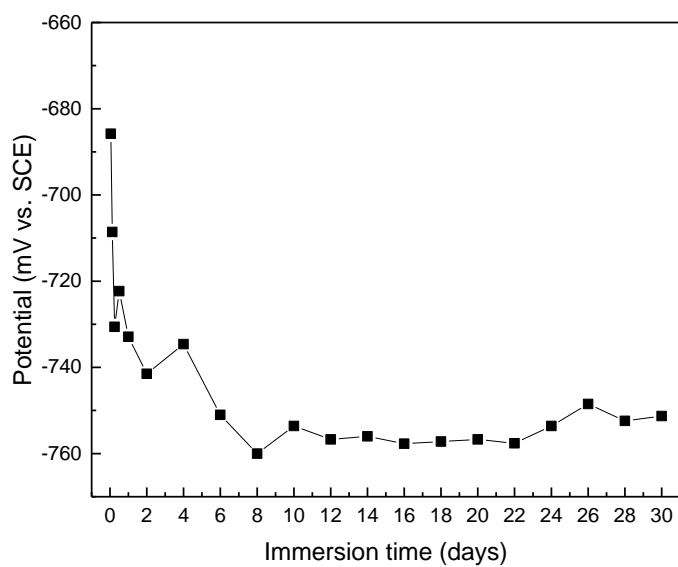


Figure 7.6 OCP of X52 steel in basic soil solution as a function of time.

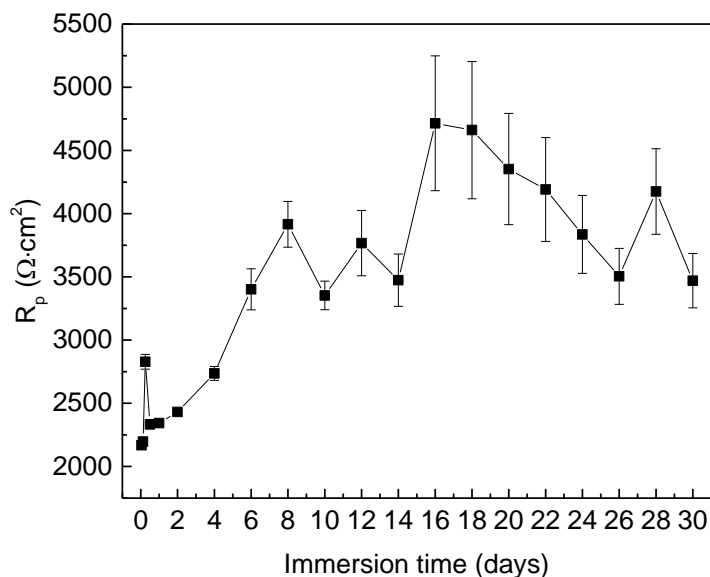


Figure 7.7 The R_p values fitted from the LPR measurements on X52 steel in the base soil solution.

Furthermore, the R_p values measured in the soil solutions containing various DO concentrations are $10780 \Omega \cdot \text{cm}^2$, $3949 \Omega \cdot \text{cm}^2$ and $2168 \Omega \cdot \text{cm}^2$ for 0.4 ppm, 3.9 ppm and 7.7 ppm of DO, respectively. Obviously, the R_p decreases as the DO concentration increases.

The R_p values measured on X52 steel in the soil solutions with various pH values are $1398 \Omega \cdot \text{cm}^2$ and $1945 \Omega \cdot \text{cm}^2$ for pH 5.77 and 6.21, respectively. A smaller R_p is associated with a lower solution pH.

The LPR measurements are also conducted on X52 steel in the soil solutions containing various Cl^- concentrations. Table 7.2 shows the R_p values as a function of Cl^- concentration immediately after the OCP is stable and after 30 days of testing in the

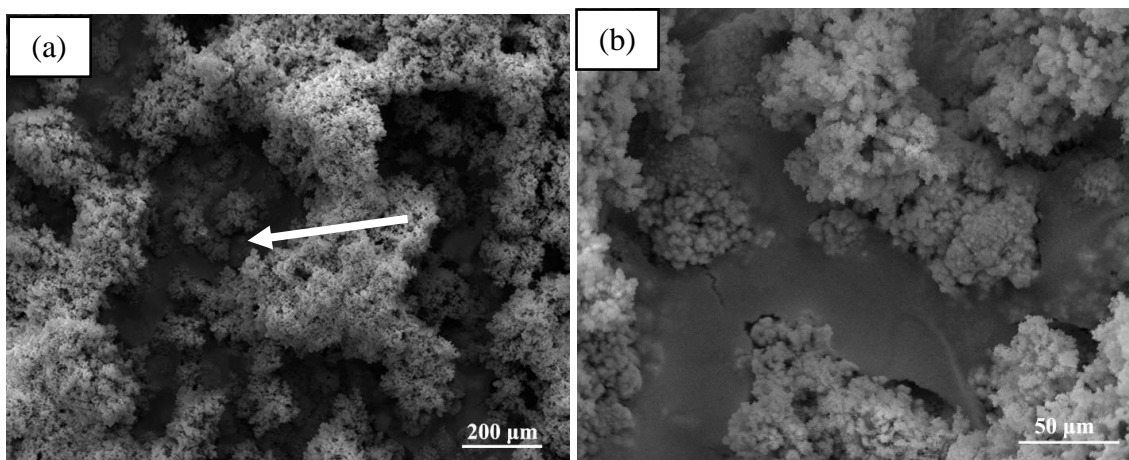
solution. It is shown that, generally, with the increasing Cl^- concentration, the R_p decreases. After 30 days of immersion, the R_p value measured in 5 ppm Cl^- solution is higher than that measured after OCP is initially stable, but the R_p values are smaller at other Cl^- concentrations.

Table 7.2 The R_p values of X52 steel in the soil solutions containing various Cl^- concentrations immediately after the OCP is stable and after 30 days of testing in the solution.

After OCP stable		30 days	
Cl^- concentration	R_p ($\Omega \cdot \text{cm}^2$)	Cl^- concentration	R_p ($\Omega \cdot \text{cm}^2$)
5 ppm (Base condition)	2168	5 ppm (Base condition)	3470
50 ppm	2184	50 ppm	2075
500 ppm	2006	500 ppm	1795
5000 ppm	1568	5000 ppm	1414

7.3.3 SEM analysis

SEM images of X52 steel in base soil solution at various immersion times are shown in Figure 7.8. It is seen that corrosion products are formed on the steel surface. The corrosion products are generally porous, and do not uniformly distribute on the steel.



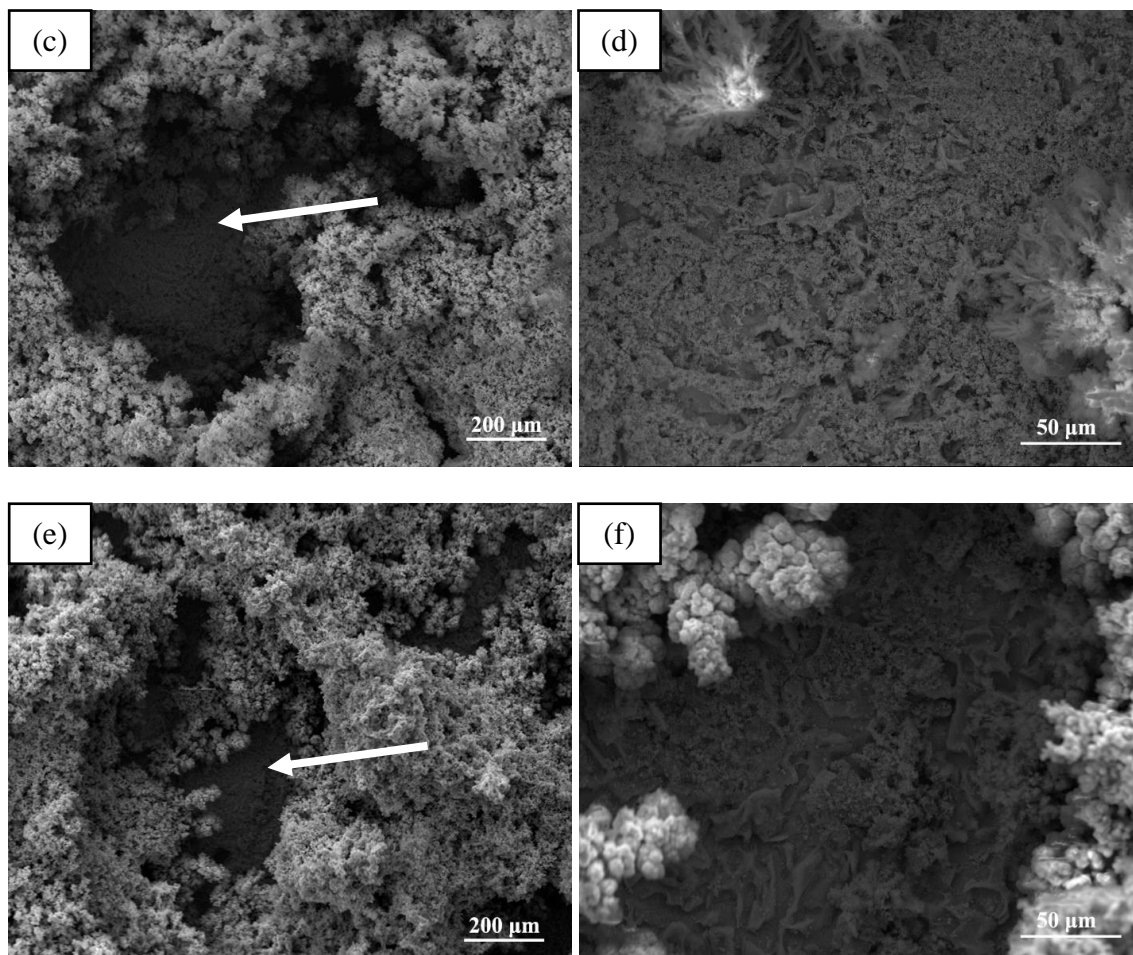


Figure 7.8 SEM images obtained for X52 steel in base soil solution at various immersion times: (a, b) 10 days, (c, d) 20 days, (e, f) 30 days.

Figure 7.9 shows the SEM views of the steel electrode after 30 days of immersion in the soil solutions containing various Cl^- concentrations. It is seen that there are less corrosion products on the steel surface when the Cl^- concentration is higher. A flower-like structure of the corrosion products is found when the Cl^- concentration is 500 ppm and 5000 ppm.

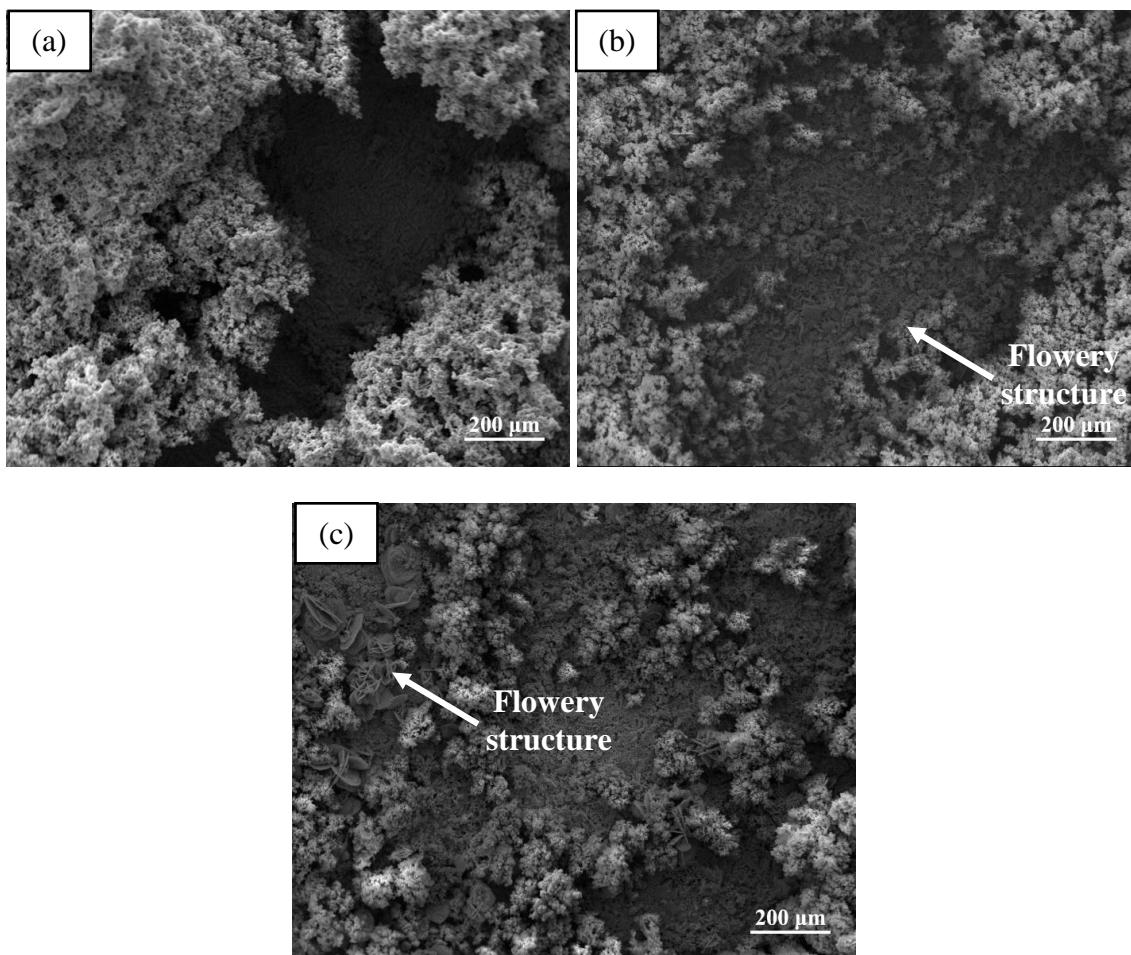


Figure 7.9 SEM images of X52 steel after 30 days of immersion in the soil solutions containing various Cl^- concentrations: (a) 50 ppm, (b) 500 ppm, (c) 5000 ppm.

7.3.4 Optical microscope observation

After the corrosion products are removed from the steel surface, optical images of the steel are taken and shown in Figure 7.10. It is seen that corrosion pits are present on the steel in all solutions. The size of the pits formed in low Cl^- concentration solutions is larger than that formed at high Cl^- concentration solutions, as indicated by the arrows.

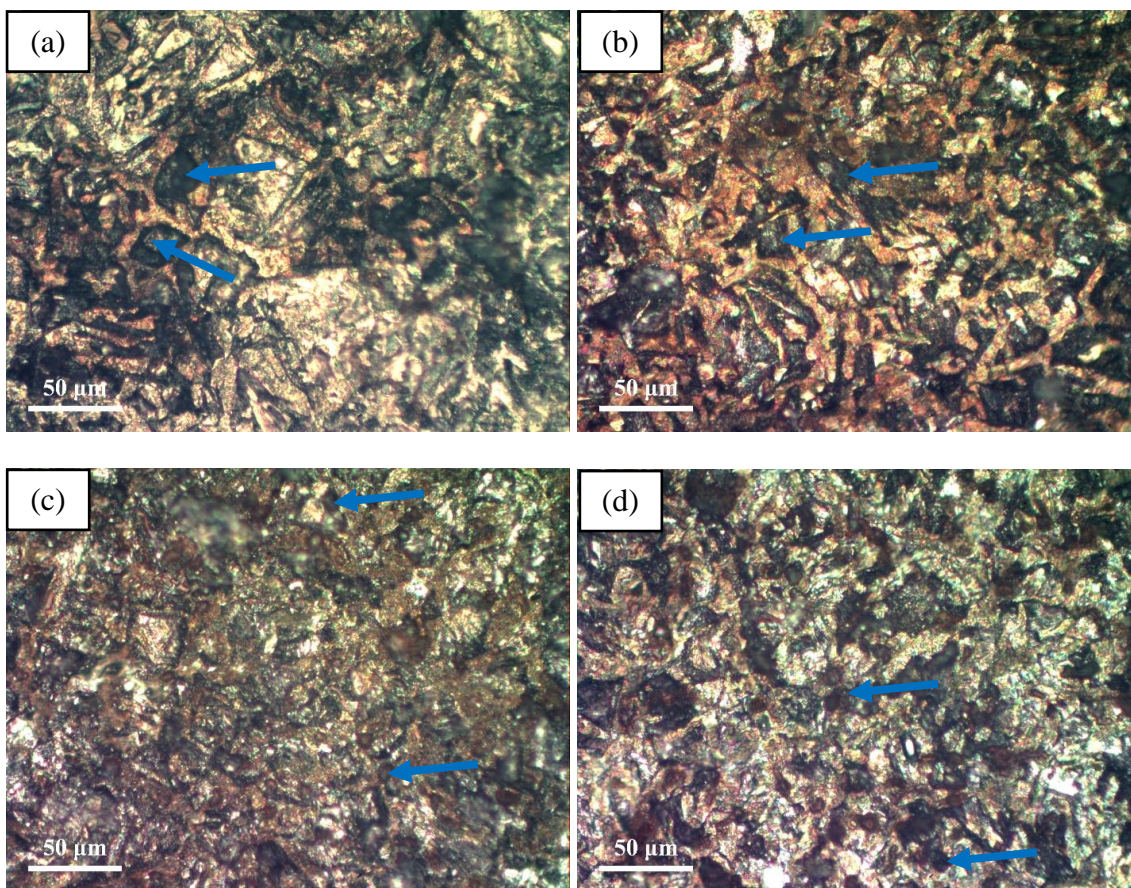


Figure 7.10 Optical images of X52 steel after 30 days of immersion in the soil solutions containing various Cl^- concentrations upon removal of corrosion products:

(a) 5 ppm, (b) 50 ppm, (c) 500 ppm, (d) 5000 ppm.

7.3.5 XRD patterns

Figure 7.11 shows the XRD spectra of the corrosion products on the steel specimen after various times of immersion in the soil solution. It is seen that Fe, $\gamma\text{-FeOOH}$ and CaCO_3 are identified, where $\gamma\text{-FeOOH}$ emerges as the dominant products.

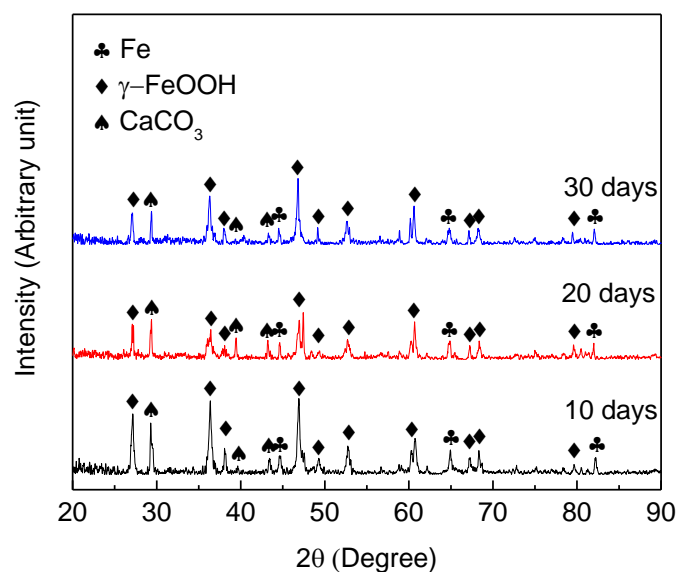


Figure 7.11 XRD patterns spectra of the corrosion products on the X52 steel specimen after various times of immersion in the soil solution.

7.4 Discussions

7.4.1 Corrosion of X52 steel in the simulated soil solution

The soil solution used in this work is at a near-neutral pH condition. The base solution is open to air, and the content of DO is 7.7 ppm. The cathodic reaction is mainly the reduction of dissolved oxygen, and the anodic reaction is the iron oxidation.

The XRD results show that the dominant corrosion products are γ -FeOOH, which are formed by chemical reactions (2-15) ~ (2-17) [53]. It is accepted that γ -FeOOH has two structures, i.e., small crystalline globules (sandy crystals) and fine plates (flowery structures) [159]. In this work, the sandy crystalline structure is found for most testing

conditions as shown in Figures 7.8 and 7.9, and the flowery structure is only found in Cl^- concentrations of 500 ppm and 5000 ppm after 30 days of immersion.

Figures 7.2 and 7.5 show that the anodic branch possesses a passivation behavior over a certain potential range, which is associated with the formation of $\gamma\text{-FeOOH}$. However, $\gamma\text{-FeOOH}$ is usually porous, and can provide somewhat protection to the steel. Localized pitting corrosion can occur at the pores of the corrosion products. Moreover, the $\gamma\text{-FeOOH}$ can detach from the steel easily, exposing the steel to the soil solution and causing corrosion.

CaCO_3 is also found on the steel surface, and it could be due to the relatively high Ca^{2+} concentration in the soil solution. The CO_3^{2-} is produced due to dissociation of bicarbonate ions upon dissolution of CO_2 in the solution.

7.4.2 Effect of dissolved oxygen concentration on the corrosion process

Oxygen will be depleted on the steel surface as it is consumed in the cathodic reaction. The depletion rate, which is the same as the electrochemical cathodic reaction rate, is usually higher than the diffusion rate of dissolved oxygen from the bulk solution to the steel surface. As a result, when the oxygen reduction reaction becomes the dominant cathodic reaction, the oxygen diffusion rate determines the total corrosion reaction rate. The diffusive limiting current density i_L can be expressed as:

$$i_L = D_z n F C_b / \delta \quad (7-1)$$

where D_z is the diffusivity of reactive species, n is the number of electrons/mole exchanged in a redox reaction, F is Faraday's constant, δ is the thickness of the stagnant layer on the electrode, and C_b is the bulk concentration of the reactive species.

In Eq. (7-1), D_z is a function of temperature. If the temperature keeps constant and δ does not change, i_L is proportional to C_b . When the DO concentration in the soil solution is changed from 7.7 ppm to 3.9 ppm and 0.4 ppm, the cathodic limiting current density reduces, as shown in Figure 7.3. When the DO content is as low as 0.4 ppm, the limiting current density is not observed, indicating a change of the dominant cathodic reaction from the oxygen reduction to the reduction of water.

The R_p values measured at the three DO concentrations show that the R_p increases as the DO content decreases. Since the R_p is inversely proportional to corrosion rate, the corrosion of X52 steel is reduced at a low DO concentration. In the base solution where a high DO content is present, the steel has a high corrosion rate.

One disadvantage of Eq. (7-1) is that it does not consider the formation of corrosion products on the steel surface and its further effect on the oxygen diffusion. Generally, even porous corrosion products can retard oxygen to reach the steel surface and reduce the i_L value. In Eq. (2-16), DO participates in the formation of corrosion products. More DO would favor the formation iron oxides.

7.4.3 Effect of solution pH

In addition to dissolved oxygen, CO_2 is another gas that is commonly found in soils. The generation of CO_2 is associated with the rotten plants and/or microbial metabolism [55]. The CO_2 is able to dissolve in the soil solution through the steps in Eqs. (2-1) ~ (2-

4). As a result, the solution pH is reduced. The amount of CO₂ that can dissolve in water and the resulting solution pH are affected by the CO₂ partial pressure, i.e., a higher CO₂ partial pressure can lead to a lower solution pH.

In this work, the solution pH is between 5.77 and 7.40. It has been suggested [29] that the direct reduction of hydrogen ions mainly occurs when pH < 4. In CO₂ solutions, the direct reduction of H₂CO₃ (Eq. (2-8)) becomes dominant when pH is between 4 and 6. When pH > 5, the reduction of bicarbonate ions (Eq. (2-9)) becomes important. In addition, when pH > 5 and $P_{\text{CO}_2} \ll 1$ bar, the reduction of water (Eq. (2-10)) is also important. When the mixed gases of CO₂ and N₂ are purged into the soil solution, the DO concentration reduces to a value of around 0.4 ppm. The oxygen reduction is no longer important.

By comparing the R_p values determined at three pH conditions, the decrease in solution pH would increase the corrosion rate of the steel.

7.4.4 Effect of Cl⁻ concentration

From Figure 7.5, the presence of Cl⁻ always increases the anodic current density. Moreover, a small R_p value is measured in the soil solutions containing higher Cl⁻ concentrations, indicating that the corrosion rate of X52 steel is large at high Cl⁻ concentration conditions. Similar phenomenon was also observed by other researchers [160-162]. Chloride ions can contribute to the anodic dissolution of steels by: [59]





However, Figure 7.5(a) shows that the cathodic limiting current density under the high Cl^- concentration condition is smaller than that at the low Cl^- concentration. When the Cl^- concentration is increased in the soil solution, the salinity of the solution increasing, which reduces the DO content in the high salinity solution. Moreover, it was reported that chloride ions could reduce the rate of oxygen reduction reaction by inhibiting the adsorption of oxygen [163]. Thus, the oxygen diffusive current density decreases as the Cl^- concentration increases.

7.4.5 Effect of immersion time

The OCP of X52 steel shifts to a more negative value first and becomes relatively stable with time. This is due to the generation and deposit of corrosion products such as iron oxides on the steel surface [61]. Thick and compact corrosion products can shift the OCP because dissolved oxygen is more difficult to be transported to the steel surface from the solution.

As the corrosion products become thicker and more compact when the immersion time increases, the corrosion rate of the steel should reduce. Figure 7.7 shows that the R_p value increases first and becomes relatively stable afterward, which indicates the reduced corrosion rate at first, followed by a relatively stable value.

The SEM images in Figure 7.8 help to explain the fluctuation of R_p values. As mentioned, the corrosion products which mainly contain $\gamma\text{-FeOOH}$ are porous. Moreover, the corrosion products are not uniformly distributed. The product layer can detach locally

when it is too thick, exposing the bare steel to the solution. Corrosion occurs locally and generates new corrosion products. This causes fluctuations of R_p values, which is inversely proportional to the corrosion rate.

Different from corrosion in the base solution, X52 steel in the soil solution containing Cl^- concentrations larger than 5 ppm has a higher corrosion rate after 30 days of immersion, as shown by the lower R_p values. Combine with the optical observations in Figure 7.10, pitting corrosion happens on the steel when a high concentration of Cl^- ions is included. This would increase the corrosion rate of the steel for a long-term immersion condition.

7.5 Summary

Corrosion reactions of X52 steel in the simulated soil solution include the iron oxidation, oxygen reduction and water reduction, depending on the content of dissolved oxygen in the solution. Corrosion products, which are mainly $\gamma\text{-FeOOH}$, reduce the corrosion rate by limiting the oxygen reduction on the steel surface and “passivating” the steel. The corrosion products are porous and not uniformly distributed on the steel.

Reducing the content of dissolved oxygen in the soil solution can decrease the cathodic reaction rate and even change the dominant cathodic reaction, helping to control the steel corrosion.

The CO_2 dissolves in the soil solution and decreases the solution pH, causing the increasing corrosion rate of X52 steel.

Chloride ions are able to increase the corrosion rate of X52 steel by stimulating the anodic reaction rate, and affecting the formation of corrosion products on the steel surface. A high concentration of chloride ions even results in pitting corrosion.

Chapter Eight: Modelling of corrosion of pipelines in soil solution

8.1 Introduction

Once a pipeline is abandoned in place, it will stay in the soil for hundreds of years or even longer. During the abandonment, it is hoped that the pipeline can maintain the structural integrity, and avoid soil subsidence. Corrosion is the primary mechanism reducing the pipe wall thickness and degrading the pipeline integrity. It is thus crucial for industry to predict the long-term corrosion rate, and evaluate the risks associated with the pipeline abandonment.

Experimental testing provides the key methodology to study the corrosion mechanism of the abandoned pipelines in the soil, and obtain the corrosion rates over a limited time period. Tests cannot be conducted as long as the time period for a pipeline in abandonment. Moreover, pipelines usually extend over hundreds or thousands of kilometers, passing different type of soils. It is impossible to conduct corrosion tests under all the environmental conditions. A well-accepted method for corrosion prediction is to develop a mechanistic model, which is combined with numerical computation, enabling determination of the long-term corrosion rate of the pipelines.

Prediction models are not rare for pipeline corrosion. However, the majority of the existing models are empirical or semi-empirical ones [61, 90, 164], which lack theoretical background and have a poor extrapolation performance. Mechanistic models [52, 84, 91, 92, 165-168] were developed to predict pipeline corrosion occurring under disbonded coating with/without CP during normal operation. Obviously, these do not apply for abandoned pipelines where the operation is stopped. To date, there has been no relevant

model available for evaluation and prediction of the long-term corrosion of an abandoned pipeline in soils.

This chapter is the continuation of the research work to study corrosion of abandoned pipelines in soils. Based on the corrosion mechanism of X52 pipeline steel in the simulated soil solution determined in Chapter Seven, a mechanistic model, which combined both mass transfer of corrosive species in the soil solution and electrochemical reactions on the steel surface, was developed. The relevant electrochemical parameters were derived from the polarization curve measurements in Chapter Seven. A computational code was written, enabling calculation of the corrosion kinetic parameters, and determination of contributions from individual reaction to the total corrosion process. The modelling results were validated by experimental data.

8.2 Determination of kinetic parameters

8.2.1 A brief review of corrosion kinetic parameters used in previous modelling work

Corrosion kinetic parameters are important constituents of a mechanistic model, and their values can greatly affect the reliability and accuracy of the modelling results. By reviewing the literature on corrosion models of steels in soils, it was found that most researchers used the corrosion kinetic parameters from others' publications, not from their own experimental data. A summary of these parameters for soil corrosion modelling is shown in Table 8.1.

Table 8.1 A summary of corrosion kinetic parameters used in corrosion modelling in open publications.

		Song et al. [91]	Chang et al. [169]	Chen et al. [168]	Ibrahim et al. [170]
Fe	$i_{0,Fe}$ (A/m ²)	2×10^{-4}	1×10^{-4}	1.225×10^{-4}	7×10^{-5}
oxidation	b_{Fe} (V/dec)	0.04	0.06	0.133	0.3
O ₂	i_{0,O_2} (A/m ²)	4×10^{-9}	7×10^{-3}	-	7.7×10^{-7}
reduction	b_{O_2} (V/dec)	0.12	0.12	-	0.2
H ₂ O	i_{0,H_2O} (A/m ²)	2×10^{-3}	-	-	7×10^{-7}
reduction	b_{H_2O} (V/dec)	0.12	-	-	0.15

Note: “-” means that the values were not given or not used in the papers.

Obviously, the corrosion kinetics parameters as published varied significantly among researchers. It is realized that these models had been validated by either experimental testing or field data under specific conditions. Thus, any model to be developed, including the one for corrosion of abandoned pipelines in soils, must be based on a well-convinced corrosion mechanism under a certain environmental condition.

8.2.2 Determination of the corrosion kinetic parameters by polarization curve measurements

Potentiodynamic polarization curve is a useful electrochemical measurement technique in corrosion study. It can provide essential information on corrosion mechanisms, kinetic parameters, and corrosion rate [171]. It's a common practice to derive the anodic and cathodic Tafel slopes by linearly fitting the Tafel regions of the polarization curve, and further, to obtain the corrosion rate by using the Tafel extrapolation method [172]. However, the challenge to use this method is that the linear

portions of the Tafel regions in the measured polarization curve are supposed to extend at least one decade on the $\log i$ axis [173], ensuring the accuracy of the derived parameters. Moreover, the Tafel extrapolation method is only valid for electrochemical reactions that are completely activation controlled. Under an aerated condition where the oxygen reduction is the primary cathodic reaction, the reaction is usually controlled by mass transfer of dissolved oxygen, making the Tafel region disappear in the polarization curve.

Previous work [60, 161, 174-177] was published to determine the corrosion kinetic parameters with polarization curves, where the Tafel region was not present. A non-linear least square method was used to fit the non-linear polarization curve by minimizing the total sum of squared differences (SSV) between the experimentally measured current density and the predicted one with theoretical models by [60]:

$$SSV = \sum_1^n (i_j^{\text{exp}} - i_j^{\text{theory}})^2 \quad (8-1)$$

where i_j^{exp} is the experimentally measured current density, A/m²; i_j^{theory} is the theoretical predicted current density, A/m²; and n is the total number of data points.

There are two types of theoretical models used to predict the current density included in Eq. (8-1). One theoretical model uses a typical three-parameter equation, as shown in Eq. (8-2), or a four-parameter equation, i.e., Eq. (8-3), in the calculation [174]:

$$i = i_{\text{corr}} \left[\exp\left(\frac{\Delta E}{b_a}\right) - \exp\left(-\frac{\Delta E}{b_c}\right) \right] \quad (8-2)$$

$$i = i_{\text{corr}} \left\{ \exp\left(\frac{\Delta E}{b_a}\right) - \frac{\exp\left(-\frac{\Delta E}{b_c}\right)}{1 - \frac{i_{\text{corr}}}{i_L} \left[1 - \exp\left(-\frac{\Delta E}{b_c}\right)\right]} \right\} \quad (8-3)$$

where i_{corr} is the corrosion current density, A/m²; b_a and b_c are the anodic and cathodic Tafel slopes, respectively, V/dec; i_L is the limiting diffusive current density, A/m²; ΔE is equal to $E - E_{\text{corr}}$ where E is the applied potential, V; and E_{corr} is the corrosion potential, V. Eq. (8-2) mainly applies to anodic and cathodic reactions that are both under activation control, while Eq. (8-3) applies to cathodic reactions that are mixed controlled by including the diffusive limiting current density.

The other theoretical model is based on the mixed potential theory [178]. The total current density is the sum of current density contributions from all reactions. For corrosion of steels in an aerated soil solution, the iron oxidation is the anodic reaction that is under charge-transfer control (i.e., activation controlled). The cathodic reactions include the oxygen reduction and water reduction, where the water reduction is also under charge-transfer control, but the oxygen reduction is usually under both mass-transfer and charge transfer control. Total corrosion current density is the sum of anodic and cathodic components, and can be expressed (counter-part back reactions are neglected [161]) as:

$$i_{\text{Fe}} = i_{0,\text{Fe}} \exp\left(\frac{2.303\eta_{\text{Fe}}}{b_{\text{Fe}}}\right) \quad (8-4)$$

$$i_{O_2} = \frac{i_{0,O_2} \exp\left(-\frac{2.303\eta_{O_2}}{b_{O_2}}\right)}{1 + \frac{i_{0,O_2}}{i_{L,O_2}} \exp\left(-\frac{2.303\eta_{O_2}}{b_{O_2}}\right)} \quad (8-5)$$

$$i_{H_2O} = i_{0,H_2O} \exp\left(\frac{2.303\eta_{H_2O}}{b_{H_2O}}\right) \quad (8-6)$$

$$i = i_{Fe} - i_{O_2} - i_{H_2O} \quad (8-7)$$

where i_{Fe} , i_{O_2} and i_{H_2O} are the current densities for the reaction of Fe oxidation, O₂ reduction and H₂O reduction, respectively, A/m²; b_{Fe} , b_{O_2} and b_{H_2O} are Tafel slopes for the reaction of Fe oxidation, O₂ reduction and H₂O reduction, respectively, V/dec; i_{L,O_2} is the limiting diffusive current density of dissolved O₂, A/m²; and overpotential $\eta = E - E_{rev}$, where E_{rev} is the reversible potential, V.

The first theoretical model is mainly used to fit weak polarization curves [174], which is also called pre-Tafel region of the polarization curves [175], and ΔE is usually smaller than 70 mV. The second theoretical model can fit Tafel region of the polarization curves where $\eta \geq 70$ mV. With a comparison of the two models, the first one is simple, and is able to determine the corrosion rate directly. The second model can determine both corrosion rate and the exchange current density, which will be included in the mechanistic model to be developed in this work.

The superposition model, which is based on the second theoretical model, was first proposed by Wanger and Traud [179], and further developed by Flitt [177] and Caceres [60] to determine the corrosion kinetic parameters. To make the calculation easy, Alfaro

[180] tried to simplify the complex code by using the solver function embedded in Excel to do the curve fitting. Actually, the biggest difference between the available programs used in the parameter fitting is the algorithms to solve Eq. (8-1). In Caceres's work, the Nelder-Mead Simplex algorithm was used [60]. The solver function in Excel [181] includes three algorithms, i.e., generalized reduced gradient (GRG) nonlinear, LP simplex and evolutionary, which can solve different problems. Several other algorithms can also be used in non-linear regression, including the Gauss-Newton, the Marquardt-Levenberg, and the steepest descent methods [182].

Polarization curves of X52 steel in the simulated soil solution are shown in Figure 7.2. To determine the corrosion kinetic parameters, including anodic and cathodic exchange current densities, anodic and cathodic Tafel slopes and, if applicable, diffusive limiting current density, a computational program is written in this work based on the second theoretical model by including Eqs. (8-4) ~ (8-7). Resistance polarization takes effect when a corrosion product film is formed on the steel surface. To correct the ohmic IR drop in order to obtain the true potentials, the following equation is used [177]:

$$E_{\text{true}} = E_w - IR \quad (8-8)$$

where E_w and E_{true} are the determined potential and the "true" potential, respectively, V; I is the current, A; and R is the film resistance, Ω .

To have the best algorithm for the modelling calculation, various algorithms mentioned above are quantified. For some relatively simple algorithms, such as Gauss-

Newton, the Marquardt-Levenberg, etc., codes are written with MATLAB software and used in calculation. For the complex algorithms, Excel and/or MATLAB are used in calculation by embedding them in the software. It is found that not all algorithms can be used for the parameter determination. The reason is that some of them are not able to solve problems with so many unknown parameters, e.g., seven unknown parameters in this work. Moreover, parameters determined by some algorithms possess negative values, which are unacceptable for physical parameters. Constraints are then applied to avoid negative values. Finally, the evolutionary method in Excel and *lsqnonlin* function in MATLAB always give a good performance and are integrated into the computational program in this work. They are used independently or collaboratively in the model to obtain the results with the minimum *SSV* and derive the desired kinetic parameters.

Validation of the developed computational program is conducted by comparing the modelling results with the data in open publications, as shown in Figure 8.1. Both the experimental data and the SYMADEC prediction results are obtained from Flitt et al.'s work [177]. It is shown that the modelled curve almost copies the SYMADEC results, and the modelled curve fits very well with the experimental data. It is noted that anodic branch of the polarization curve in Figure 8.1 exhibits a curvature instead of a straight line, this could be because of the deposition of a non-passivating film on the steel surface [177]. Thus, the recorded anodic potentials are corrected for ohmic *IR* drop, and the *R* is determined as 20 Ω , which is same as the value used in Flitt et al.'s work [177].

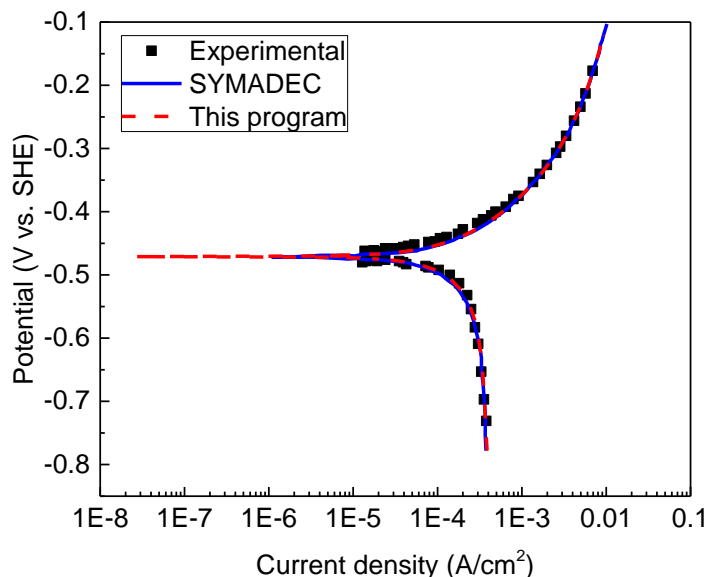


Figure 8.1 Comparison between the modelled polarization curve with experimental data and SYMADEC prediction results included in Flitt et al.'s work [177].

The computational program is then used to fit the corrosion kinetic parameters from the polarization curve measured in Figure 7.2. The R is determined as 200Ω to correct the anodic potentials. The comparison between the experimental data and the modelled curve is shown in Figure 8.2, where a good fitting is found both for the anodic branch and cathodic branches. The SSV is calculated as 4.84×10^{-7} . The determined corrosion kinetic parameters are shown in Table 8.2, and are used in the model development shown as follows.

To quantify contributions from both anodic and cathodic reactions, the total polarization curve as fitting is deconvoluted, as shown in Figure 8.3. For the total polarization curve in Figure 8.3, the ohmic IR drop associated with the film formation on

steel surface is excluded. Thus, the total polarization curve only shows contributions from the combination of anodic and cathodic reactions. It is seen that most of the cathodic reaction current density is mainly contributed by the oxygen reduction, especially when the potential is near the corrosion potential. Contribution from the water reduction is dominant only when the potential is sufficiently negative, i.e., $E \leq -1.0$ V (SCE).

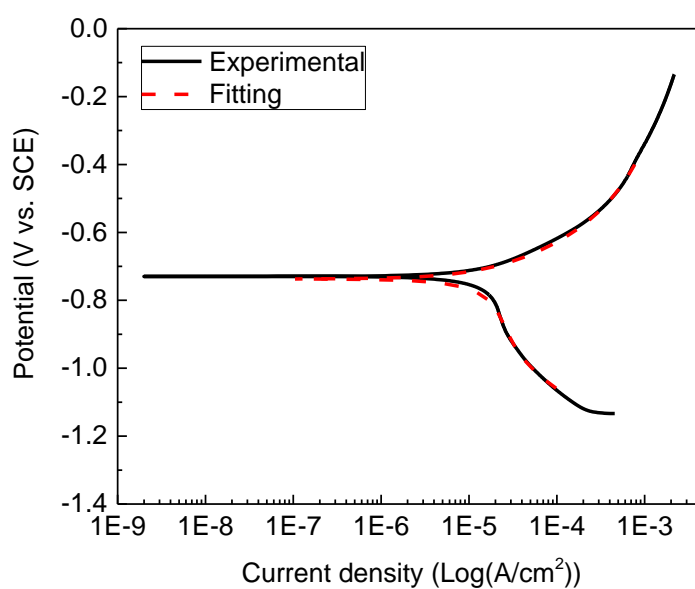


Figure 8.2 Fitting of the modelled curve with the measured polarization curve of X52 steel in the simulated soil solution.

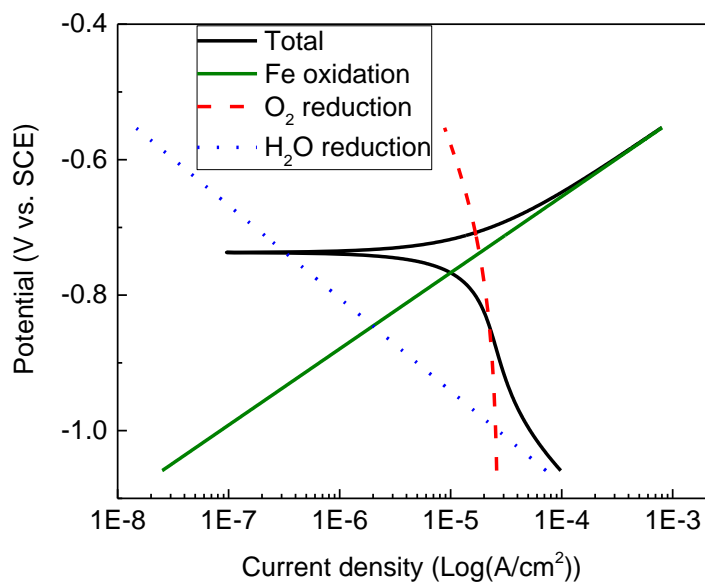


Figure 8.3 Deconvolution of the fitted polarization curve to compare the contributions from individual reactions.

Table 8.2 Corrosion kinetic parameters determined from the polarization curve fitting.

Parameters	Value
$i_{0,\text{Fe}}$ (A/m ²)	1.53×10^{-2}
b_{Fe} (V/dec)	0.112
i_{0,O_2} (A/m ²)	2.40×10^{-5}
b_{O_2} (V/dec)	0.295
i_{L,O_2} (A/m ²)	0.27
$i_{0,\text{H}_2\text{O}}$ (A/m ²)	1.21×10^{-4}
$b_{\text{H}_2\text{O}}$ (V/dec)	0.137

8.3 Model development

8.3.1 Overview of the model

The physical block of the model developed in this work is schematically shown in Figure 8.4. Bare steel is immersed into the simulated soil solution, and the solution is open to air. After O_2 is dissolved in the solution, it transports through the solution and reaches the steel surface. Dissolved O_2 participates in the cathodic reaction and becomes consumed on the steel surface. At the same time, Fe^{2+} is produced due to the anodic dissolution reaction and transports into the solution. H^+ and OH^- in the solution also migrate but maintain at an equilibrium state. When the corrosion scale is formed on the steel surface, it affects both the mass transfer of corrosive species and the anodic dissolution of the steel.

Assumptions are made to facilitate numerical calculations, including:

- The effect of chemical species as listed in Table 7.1 on corrosion is neglected, but these species affect electro-migration happening in the solution;
- Precipitation of $Fe(OH)_2$ is the primary corrosion scale, and its conversion to other chemicals is not considered [183];
- One-dimensional computational domain from the steel surface to the liquid/gas interface is used for modelling purpose.

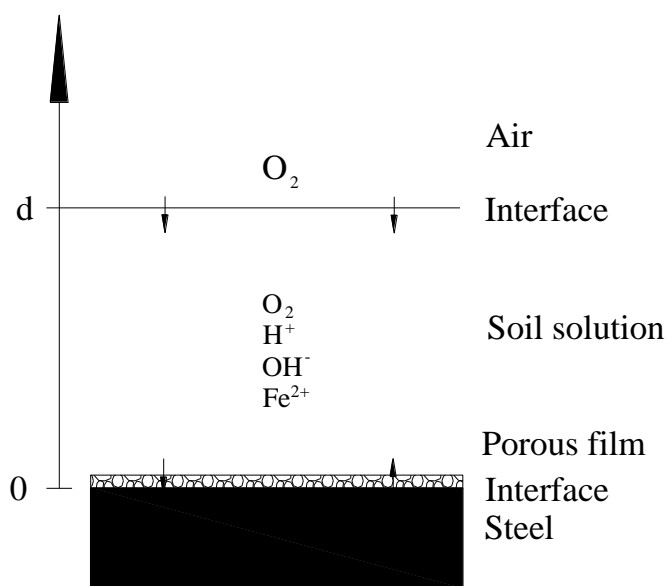


Figure 8.4 Schematic view of the physical block of the developed model.

8.3.2 Electrochemical reactions

For the aerated near-neutral soil solutions used in this work, the DO is measured as around 7.7 ppm. The cathodic reactions in this system include [51] the oxygen reduction (Eq. (2-14)) and the reduction of water (Eq. (2-10)). The iron oxidation (Eq. (2-6)) is the anodic reaction.

The current densities of the iron oxidation and water reduction reactions are expressed as Tafel equations with a porosity ε :

$$i_{Fe} = \varepsilon i_{0,Fe} \times 10^{\frac{E - E_{rev,Fe}}{b_{Fe}}} \quad (8-9)$$

$$i_{H_2O} = \varepsilon i_{0,H_2O} \times 10^{\frac{-E + E_{rev,H_2O}}{b_{H_2O}}} \quad (8-10)$$

The oxygen reduction reaction is under the mixed control, where both active reaction rate and diffusion rate of oxygen to the steel surface decide the total corrosion rate. The current density is calculated as [170]:

$$i_{O_2} = \alpha i_{0,O_2} \frac{C_{O_2,s}}{C_{O_2,ref}} \times 10^{\frac{-E+E_{rev,O_2}}{b_{O_2}}} \quad (8-11)$$

where $C_{O_2,s}$ and $C_{O_2,ref}$ are the oxygen concentrations on the steel surface and at the air/soil solution interface, respectively, mol/m³.

Kinetic parameters listed in Table 8.2 are substituted into the equations mentioned above for calculations.

The reversible potential for each reaction is expressed as:

$$E_{rev,Fe} = -0.44 + \frac{2.303RT}{2F} \log([Fe^{2+}]) \quad (8-12)$$

$$E_{rev,O_2} = 1.229 - \frac{2.303RT}{F} pH + \frac{2.303RT}{4F} \log([O_2]) \quad (8-13)$$

$$E_{rev,H_2O} = -\frac{2.303RT}{F} pH \quad (8-14)$$

where $[Fe^{2+}]$ is the activity of Fe^{2+} ions and is set as 10^{-6} M [170]; and $[O_2]$ is the activity of oxygen gas and is equal to 0.21.

The corrosion potential, E , can be calculated from the charge balance (Eq. (6-38)) on the steel surface. It's found that the corrosion potential is linked to the ratio of the oxygen

concentrations on the steel surface and at the air/soil solution interface, as indicated in Eq. (8-11). When the oxygen concentration on the steel surface decreases, because oxygen is consumed by the cathodic reaction, the determined corrosion potential decreases accordingly. As shown in Figure 7.6, the OCP shifts negatively at first, and then becomes gradually stable at around -758 mV (SCE). This stabilized value adds a minimum limit to the ratio of the oxygen concentrations in Eq. (8-11). The limit is determined and is included in the model calculation.

8.3.3 Controlling equations

Distribution and transportation of corrosive species in the solution follow the mass conservation equation (Eq. (2-26)) and electro-neutrality equation (Eq. (6-40)) [184]. The flux of the species is given by the Nernst-Planck equation (Eq. (2-27)), but the electro-migration and convection components are neglected [77]. The overall conservation equation is rearranged in Eq. (6-43), and used in the model calculation. The diffusion coefficient of O_2 , D_{O_2} , equals to $1.96 \times 10^{-9} \text{ m}^2/\text{s}$ at 25 °C [91].

8.3.4 Formation of corrosion products

The $Fe(OH)_2$ is assumed as the primary corrosion products formed on the steel surface. When the products of the concentrations of Fe^{2+} and OH^- exceed the solubility limit of $Fe(OH)_2$, solid $Fe(OH)_2$ starts to deposit. The $Fe(OH)_2$ can further convert to γ - $FeOOH$ by reacting with O_2 and water through reactions as expressed by Eqs. (2-16) ~ (2-17). However, the formation of $Fe(OH)_3$ from $Fe(OH)_2$ requires sufficient supply of O_2 , but the actual O_2 concentration near the steel surface can be very low because O_2 is

consumed by electrochemical reactions. In addition, when corrosion products are deposited on the steel surface, O₂ diffusion to the inner steel/corrosion product interface will be significantly retarded. The FeOOH is formed due to aging process of Fe(OH)₃ by dehydration, which is also indirectly affected by the O₂ concentration. Thus, the dominant corrosion products near the steel surface is Fe(OH)₂ [183].

The kinetics of the Fe(OH)₂ precipitation is expressed as [185]:

$$R_{\text{Fe(OH)}_2} = -k_{\text{eff}} \left(1 - \frac{IAP}{K_{\text{spFe(OH)}_2}} \right) \quad (8-15)$$

where $R_{\text{Fe(OH)}_2}$ is the precipitation rate of Fe(OH)₂, k_{eff} is an effective rate coefficient (2.5×10^{-11} M/s is estimated based on [183]), IAP is the ion activity product, and $K_{\text{spFe(OH)}_2}$ is the solubility constant for the reaction, which equals 1.82×10^{-15} at 25 °C [186]. The dissolution process of Fe(OH)₂ is not considered, and the precipitation rate is rewritten as:

$$R_{\text{Fe(OH)}_2} = \max(0, R_{\text{Fe(OH)}_2}) \quad (8-16)$$

The variation of the volumetric porosity with time in the system can be expressed as:

$$\frac{\partial \varepsilon}{\partial t} = - \frac{M_{\text{Fe(OH)}_2}}{\rho_{\text{Fe(OH)}_2}} R_{\text{Fe(OH)}_2} \quad (8-17)$$

where $M_{\text{Fe(OH)}_2}$ is the molecular weight of Fe(OH)_2 (89.86 kg/kmol), and $\rho_{\text{Fe(OH)}_2}$ is the density of Fe(OH)_2 (3400 kg/m³).

Precipitation of Fe(OH)_2 scale means both Fe^{2+} and OH^- ions are consumed at a rate proportional to $R_{\text{Fe(OH)}_2}$. Thus, a negative $R_{\text{Fe(OH)}_2}$ is substituted to Eq. (2-26) for the chemical reaction rate of Fe^{2+} ; for OH^- , the chemical reaction rate is expressed as $-2R_{\text{Fe(OH)}_2}$.

8.3.5 Initial and boundary conditions

Initial conditions consider the moment that the steel is not immersed in the soil solution, and corrosion is not yet to happen. The DO is saturated and uniformly distributed in the solution. Details about calculating the DO content in the solution are included in Appendix C. Concentrations of H^+ and OH^- ions are uniformly distributed, and their concentrations can be calculated with the input of solution pH value, which is measured as 7.40.

Two boundaries are considered in this work. One is the air/solution interface, and the other one is the steel surface. At the air/solution interface, the O_2 concentration is constant at a saturated condition, denoting as $C_{\text{O}_2\text{ref}}$. For OH^- and Fe^{2+} ions, a zero-flux boundary condition is applied. On the steel surface, the boundary conditions for species are set as follows:

$$N_{\text{Fe}^{2+}} = \frac{i_{\text{Fe}^{2+}}}{2F} \quad (8-18)$$

$$N_{\text{O}_2} = -\frac{i_{\text{O}_2}}{4F} \quad (8-19)$$

$$N_{\text{OH}^-} = \frac{i_{\text{O}_2}}{F} + \frac{i_{\text{H}_2\text{O}}}{F} \quad (8-20)$$

In addition, H^+ ions are always at an equilibrium state with OH^- ions in the solution.

8.3.6 Methods for solving the numerical equations

The finite difference method is used to solve the transient ordinary and partial differential equations, with non-uniform space interval grids created for the one-dimensional geometry and the central implicit scheme for transient calculation.

8.4 Computational results and modelling validation

8.4.1 Modelling and validation of corrosion rate of the steel

Corrosion rate of the steel in the simulated soil solution can be determined when the current density is obtained with Eq. (6-39), where the current density is calculated as [187]:

$$i_{\text{corr}} = \frac{B}{R_p} \quad (8-21)$$

where B is the Stern-Geary coefficient, and is related to anodic and cathodic Tafel slopes, i.e., b_a and b_c , by [187]:

$$B = \frac{b_a b_c}{2.303(b_a + b_c)} \quad (8-22)$$

As shown in Figure 8.3, the oxygen reduction dominates the cathodic reaction in this system. The Tafel slope for the oxygen reduction is used in Eq. (8-22) to calculate B . With the values in Table 8.2 and the fitted R_p values in Figure 7.7, the corrosion rate as a function of time is calculated and plotted in Figure 8.5 as compared with experimental results.

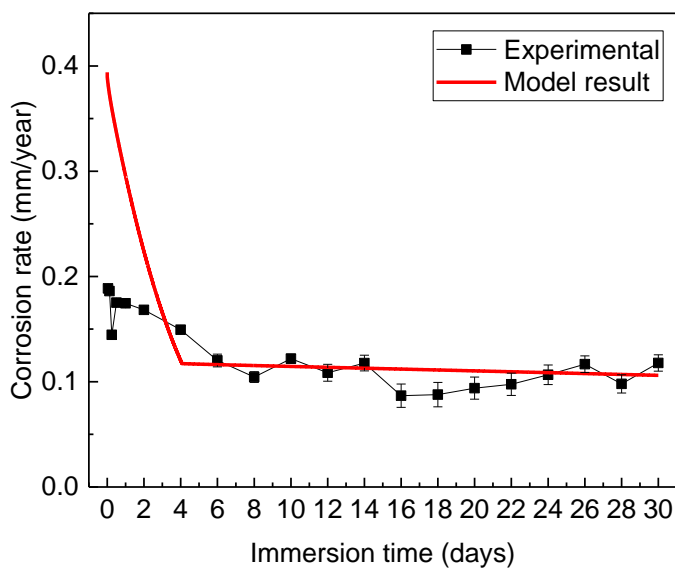


Figure 8.5 Comparison of corrosion rates of the steel in the simulated soil solution determined by experimental testing with the modelling results.

Similar to the experimental results, the predicted corrosion rate has the same trend that the corrosion rate reduces quickly in the first 7 days, and then becomes relative stable

until 30 days. Although the predicted corrosion rates are higher than the experimental results at the beginning, they match each other very well in the long-term period.

Dependence of corrosion potential on time is also obtained with the developed model. The comparison between the experimentally measured results with the modelling results is shown in Figure 8.6. Obviously, the modelling results are well consistent with the experimental measurements, demonstrating the reliability of the developed model in corrosion prediction of X52 pipeline steel in the simulated soil solution.

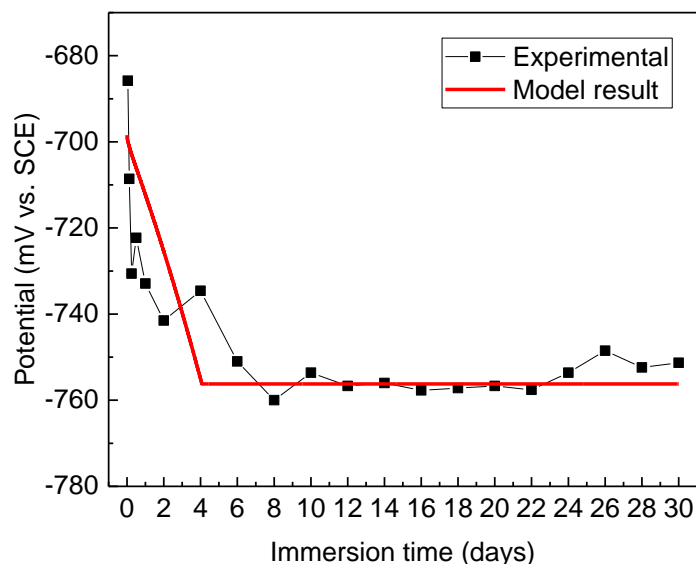


Figure 8.6 Comparison of the corrosion potential of X52 steel in the simulated soil solution determined by experimental measurements with the modelling results.

8.4.2 Time dependence of the porosity of corrosion products

Both experimental testing and modelling results show that the corrosion rate decreases during the long-term immersion of the steel in the simulated soil solution,

which is due to the formation of a protective corrosion product film on the steel surface. Porosity of the film is an important indicator of its protectiveness. Generally, the smaller the porosity, the more protective the film, and thus the smaller the corrosion rate will be. Figure 8.7 shows the modelling results of the porosity of the corrosion product film as a function of time. It is seen that the porosity decreases continuously with time in the test period.

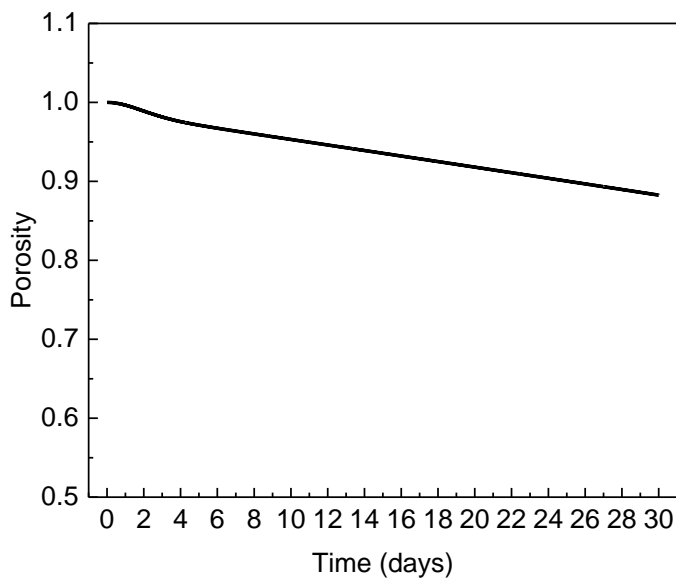


Figure 8.7 Time dependence of the porosity of the corrosion product film.

8.4.3 Distributions of the concentration of corrosive species in the solution

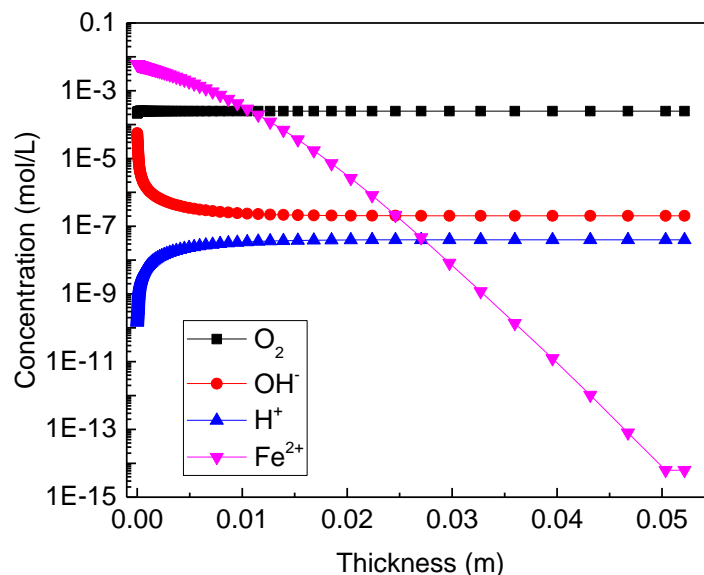


Figure 8.8 Concentration distribution of various species in the solution.

Distributions of concentrations of various species contained in the solution are shown Figure 8.8. One major advantage of a mechanistic model over empirical and semi-empirical ones is that it is able to determine the distribution of various species in the liquid phase. Generally, the distribution of the species can tell important information about the corrosion progress. As shown in Figure 8.8, the oxygen concentration on the steel surface is lower than that at the air/solution interface. This is attributed to the cathodic reaction where the dissolved oxygen is consumed. The high concentration of Fe²⁺ on the steel surface is due to the iron oxidation reaction. The OH⁻ can be generated from both the oxygen reduction and water reduction. The concentration of H⁺ on the steel surface and at the air/solution interface are 1.44×10^{-10} mol/L and 3.98×10^{-8} mol/L,

corresponding to a pH of 9.84 and 7.40, respectively. Obviously, the pH value on the steel surface is much higher than the initial solution pH, i.e., 7.40, due to the cathodic reductive reactions to generate OH^- in the solution.

8.4.4 Effect of dissolved oxygen concentration on corrosion rate of the steel

The mechanistic model is used to study the effect of DO concentration on the steel corrosion rate. Corrosion kinetic parameters for two low DO concentrations, i.e., 3.9 ppm and 0.4 ppm, are determined by fitting the polarization curves shown in Figure 7.3 using the developed computational program. When the DO concentration is 3.9 ppm, the corrosion mechanism is basically the same as that at the base condition (7.7 ppm). After corrosion kinetic parameters and operating conditions, including temperature, solution pH, oxygen concentration or oxygen partial pressure, are input in the model, the corrosion rate can be calculated. However, when the DO concentration is 0.4 ppm, the reduction of water becomes the dominant cathodic reduction. The equations representing oxygen reactions, both in the process of polarization curve fitting and model calculation, are removed. The calculated corrosion rates at various DO concentrations are shown in Figure 8.9. In addition, the experimentally determined corrosion rates of the steel in the soil solutions, which are calculated with the R_p values mentioned in Section 7.3.2 and Eq. (8-21) and (8-22), are also shown. These corrosion rates apply for conditions where the OCP of the steel in the soil solution immediately becomes stable. Although a deviation exists between the experimental result and the modelling result, especially at high DO concentrations, the model exhibits the trend that DO is able to increase the corrosion rate

of the steel. The steel in the base condition (7.7 ppm) experiences the most severe corrosion.

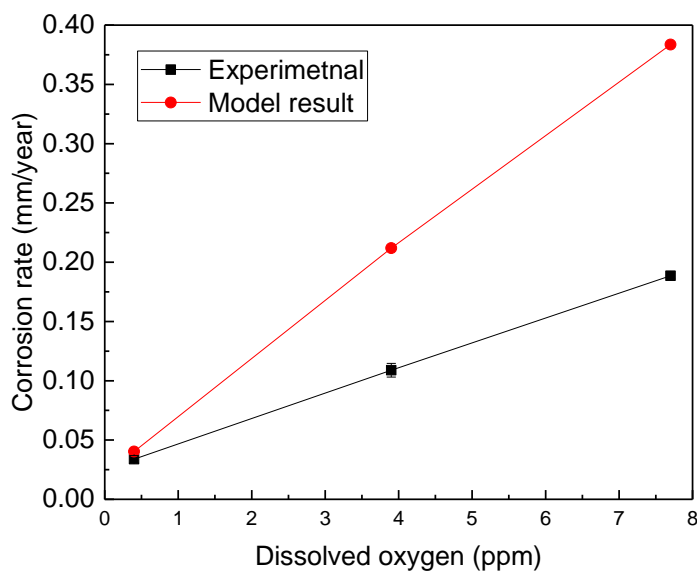


Figure 8.9 Dependence of corrosion rate on the dissolved oxygen concentration in the soil solution.

8.4.5 Long-term corrosion rate prediction

Figure 8.10 shows the predicted corrosion rate and thickness loss of the steel after long-term exposure in the soil solution. The prediction is a continuation of the result shown in Figure 8.5. For long-term corrosion, the corrosion product film is assumed to be porous. There exists a minimum scale porosity at which the corrosion rate keeps constant at a relatively low value during the long-term exposure. The porosity value is determined based on the minimum limit of the ratio of the oxygen concentrations on the steel surface and at the air/soil solution interface.

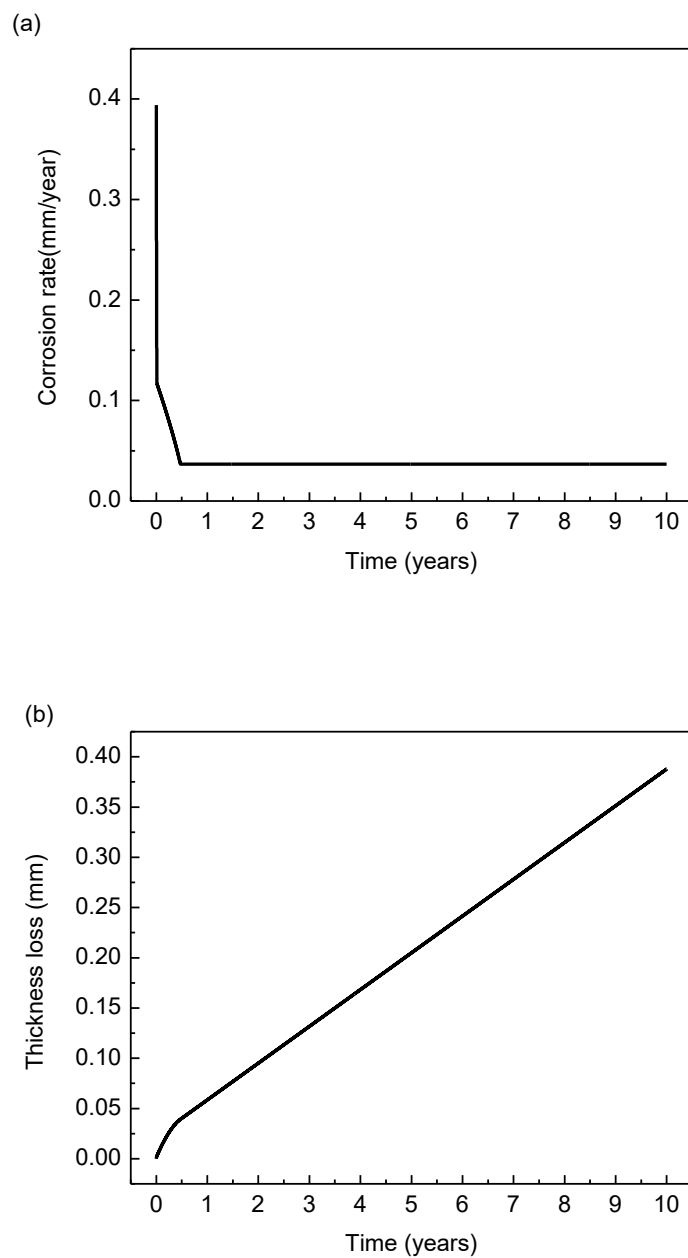


Figure 8.10 Predicted (a) corrosion rate and (b) thickness loss of the steel after a long-term exposure in the soil solution.

Thickness loss rate of the steel is directly related to the corrosion rate, i.e., when the corrosion rate is high, the thickness loss rate is also high, which is true for the beginning. After a long-term exposure, i.e., around a half year, the thickness loss linearly increase with time. The thickness loss rate is so low that the maximum thickness loss after 10 years is only 0.3879 mm. As the thickness loss is calculated based on the uniform corrosion rate, it is thus seen that uniform corrosion shall not be a big threat to the integrity of the abandoned pipelines.

8.5 Summary

A mechanistic model, which combines both mass transfer of corrosive species in the simulated soil solution and electrochemical reactions on the steel surface, is developed, enabling prediction of corrosion rate and relevant parameters for X52 pipeline steel in the solution. Essential parameters used in the mechanistic model are derived from the measured polarization curves with the developed computational program. This program can determine not only the corrosion kinetic parameters, but also the contributions from each electrochemical reaction to the corrosion process. The developed model is validated by comparing the calculated corrosion rate and corrosion potential with the experimental data, with a very good consistence. Dependence of the porosity of the corrosion product film on time, distributions of various corrosive species in the solution, and dependence of the corrosion rate on dissolved oxygen concentration are also determined. The long-term corrosion rate and the thickness loss of the pipeline steel in the soil solution are given, which show that uniform corrosion is not a big threat to the integrity of the abandoned pipelines.

Chapter Nine: Conclusions and recommendations

9.1 Conclusions

Development of mechanistic models and numerical methods to evaluate and predict corrosion occurring in oil industry is the key target of this research. These include CO₂ corrosion of above-ground pipelines, corrosion of downhole tubulars in SAGD/CO₂ co-injection systems, corrosion of tubing in supercritical CO₂ conditions, and corrosion of abandoned pipelines in soils. Primary conclusions are drawn as follows.

A home-designed flow loop system is used to investigate corrosion of X65 steel specimens in a CO₂-saturated single-phase brine. The steel electrodes installed at the top and the bottom of the flow pipe possess different corrosion activities in the CO₂-containing environments. While they experience the identical fluid mechanic condition, the larger corrosion activity of the bottom electrode can be attributed to the higher hydrostatic pressure compared to the top electrode.

For corrosion of X65 pipeline steel in CO₂-saturated fluid flow, which are either oil-free solutions or oil-water emulsions, mass-transfer of corrosive species, such as H⁺ and H₂CO₃, dominates the cathodic reaction during corrosion of the steel. An increase in fluid flow velocity leads to increasing corrosion of the steel by accelerating the mass transfer step. The dominant effect of an elevated temperature on the steel corrosion at low solution pH, such as the pH smaller than 5, is to enhance the corrosion reaction kinetics, rather than the scale formation, thus to increase the corrosion rate. The presence of oil in the CO₂-saturated fluid flow does not affect the corrosion mechanism, but decreases the corrosion rate. This effect is increased with the increasing oil content, which is attributed

to the increased opportunity that the pipe wall becomes oil-wetting. The semi-empirical model developed based on CFD simulation and the derived parameters is reliable to predict the corrosion rate of pipeline steels in CO₂-saturated fluid flow.

A semi-empirical mode is developed to predict the corrosion rate of both injection and production steel tubulars in SAGD/CO₂ co-injection systems. A computational code is written to enable calculation of the pH of CO₂-saturated solutions present on the steel tubulars based on mechanistic analysis and calculation of chemical reactions and their reaction equilibrium constants. In addition to solution pH, the effects of CO₂ partial pressure, scaling factor, and contents of oil and sands on the steel corrosion are quantified. For both the injection and production tubulars, the CO₂ corrosion rates are very small due to formation of a layer of compact scale on the steel surface at the high operating temperature conditions, effectively protecting the steel tubulars from corrosion attack. However, the corrosion rate can increase to high levels, especially for the production tubular, when the scale is broken and the sands induce erosion, in addition to the corrosion, to the tubular.

A mechanistic model is developed to predict the corrosion of steel tubing under the supercritical CO₂ storage conditions. The model integrates a number of sub-models that quantify various interrelated steps contributing to the corrosion processes. The water chemistry sub-model is able to determine the solution pH and the concentrations of involved species. To correct the non-ideal environmental conditions, both gas fugacity coefficient and ion activity coefficient are used to quantify the effect of high pressure and high salinity environmental conditions on corrosion. In the electrochemical corrosion sub-model, both charge-transfer and mass-transfer steps and their effect on corrosion are

quantified. The scale formation is considered due to its effect on the corrosion rate. The modelled corrosion rates are consistent with the testing and literature results, demonstrating the reliability of the model in corrosion prediction for steel tubing in CO₂ storage.

For corrosion of X52 pipeline steel in the simulated Regina clay soil solution, the electrochemical anodic and cathodic reactions include the iron oxidation, oxygen reduction and water reduction, respectively. Corrosion products which are mainly γ -FeOOH help reduce the corrosion rate by inhibiting both the anodic and cathodic reactions. However, the protectiveness is limited because the corrosion products are porous and not uniformly distributed on the steel surface even for a long-term period. Reducing the dissolved oxygen concentration in the soil solution can decrease the cathodic reaction rate and even change the dominant cathodic reaction, thus helping to reduce the corrosion rate of the steel.

A mechanistic model, which combines both mass transfer of corrosive species in the soil solution and electrochemical reactions on the steel surface, is developed to predict the long-term corrosion progression of abandoned pipelines in the soil solution. Essential parameters used in the mechanistic model are derived from the measured polarization curves with the developed computational program. The program can not only determine the corrosion kinetic parameters, but also quantify contributions of individual reactions to the corrosion process. The developed model is validated by comparing both the calculated corrosion rate and corrosion potential with the experimental data, with a very good consistence. Dependence of the porosity of the corrosion product film on time, distributions of various corrosive species in the solution, and dependence of the corrosion

rate on dissolved oxygen concentration were also determined. The long-term corrosion rate and thickness loss of the pipeline steel in the soil solution are given, which show that uniform corrosion is not a big threat for the abandoned pipeline.

9.2 Recommendations

This research advances development of mechanistic models and numerical methods for corrosion prediction in oil industry. Further work is recommended to further optimize the models for a more accurate determination of the corrosion behavior and rate, making it more representative of the reality.

1) Modelling of localized pitting corrosion of steel tubing and pipelines

For in-service tubing and pipelines, localized pitting corrosion represents the vital threat to asset integrity in oil industry. The penetration of corrosion pits can be one or more magnitudes faster than that of uniform corrosion. Difficulties in understanding and quantifying the initiation mechanisms and propagation kinetics of the pits limit the development of reliable models to simulate the pitting corrosion. Effort should be made in this area to contribute to a strong science base and simultaneously, to meet the immediate industry needs.

2) Investigation of corrosion of steel tubulars in SAGD systems

SAGD is a relative new technology in enhanced oil recovery, where the extreme operating conditions result in corrosion unknown to use. To dates, there has been limited work to study the corrosion of steel tubular in SAGD systems. A more thorough understanding of the formation of corrosion products and their composition and structure at the high temperature conditions is crucial to further optimize the prediction model. In

addition, the field corrosion coupons installed in SAGS systems should help provide corrosion data to validate the modelling results.

3) To study the corrosion of abandoned pipeline steel in soils

It has been recognized that the simulated soil solutions are not fully representative of the actual soil conditions that abandoned pipelines encounter in the field. The soil types and their moisture, aeration and conductivity can greatly affect the transport of various species, especially dissolved oxygen and CO₂, to the steel surface, affecting the corrosion mechanism and rate. Further investigation of the steel corrosion in actual soils will provide more realistic inputs to the developed corrosion prediction models.

References

- [1] L. Popoola, A. Grema, G. Latinwo, B. Gutti, A. Balogun, Corrosion problems during oil and gas production and its mitigation, *International Journal of Industrial Chemistry*, 4 (2013) 35.
- [2] G. Koch, J. Varney, N. Thompson, O. Moghissi, M. Gould, J. Payer, International measures of prevention, application, and economics of corrosion technology study, in, NACE International, Houston, 2016.
- [3] D. Brondel, R. Edwards, A. Hayman, D. Hill, S. Mehta, T. Semerad, Corrosion in the oil industry, *Oilfield review*, 6 (1994) 4-18.
- [4] D. Brondel, F. Montrouge, R. Edwards, A. Hayman, D. Hill, S. Mehta, T. Semerad, Corrosion in the oil industry, *Journal of Petroleum Technology*, 39 (1987) 756-762.
- [5] S.-L. Fu, J.G. Garcia, A. Griffin, Corrosion resistance of some downhole tubing materials and inhibitor effectiveness in sweet environments, in, NACE International, Houston, TX (United States), 1996.
- [6] S.S. Prabha, R.J. Rathish, R. Dorothy, G. Brindha, M. Pandiarajan, A. Al-Hashem, S. Rajendran, Corrosion problems in petroleum industry and their solution, *European Chemical Bulletin*, 3 (2014) 300-307.
- [7] M.R. Simons, Oil and gas "Rust": An evil worse than depletion, in: Offshore technology conference, Houston, Texas, 2008.
- [8] Alberta Energy Regulator, Pipeline performance in alberta, 1990–2012. Report 2013-B, Calgary: AER, 2013.
- [9] S. Nešić, Key issues related to modelling of internal corrosion of oil and gas pipelines – A review, *Corrosion Science*, 49 (2007) 4308-4338.
- [10] M.B. Kermani, D. Harrop, The impact of corrosion on oil and gas industry, *SPE Production & Facilities*, 11 (1996) 186-190.
- [11] D.N. Veritas, Final report: Understanding the mechanisms of corrosion and their effects on abandoned pipelines (Report No.: TAOUS813COSC), in, Calgary, Alberta, 2015.
- [12] J. Marsh, T. Teh, Conflicting Views - CO₂ corrosion models and corrosion inhibitor availability philosophies - The influence on subsea systems and pipelines design, in: Offshore Europe 2007, Society of Petroleum Engineers, Aberdeen, Scotland, U.K., 2007.
- [13] K.-M. Yap, S. Srinivasan, Key factors in development of a CO₂/H₂S corrosion prediction model for multiphase oil/gas production systems, in: CORROSION 2010, NACE International, 2010.
- [14] Z. Ahmad, Principles of corrosion engineering and corrosion control, Butterworth-Heinemann, 2006.
- [15] S. Papavinasam, Corrosion control in the oil and gas industry, Elsevier, 2013.
- [16] M.S. High, J. Wagner, S. Natarajan, Mechanistic modeling of mass transfer in the laminar sublayer in downhole systems, in: CORROSION 2000, 2000.
- [17] S.N. Smith, R.S. Pakalapati, Thirty years of downhole corrosion experience at big escambia creek: Corrosion mechanisms and inhibition, in: CORROSION 2004, NACE International, New Orleans, Louisiana, 2004.

- [18] S.-j. Gao, C.-f. Dong, A.-q. Fu, K. Xiao, X.-g. Li, Corrosion behavior of the expandable tubular in formation water, *International Journal of Minerals, Metallurgy, and Materials*, 22 (2015) 149-156.
- [19] T. Benedictus, M.D.C. van der Kuip, R.A. Kronimus, J.N. Huibregtse, F. Yavuz, G. Remmelts, J.C. Stam, Long term integrity of CO₂ storage – Well abandonment, in, Report, 2009.
- [20] M. Amani, D. Hjeij, A comprehensive review of corrosion and its inhibition in the oil and gas industry, in: SPE Kuwait Oil & Gas Show and Conference, Mishref, Kuwait, 2015.
- [21] Q. Liu, J. Whittaker, R. Marsden, Mystery of SAGD casing gas corrosivity and corrosion mitigation strategy, in: CORROSION 2015, NACE International, 2015.
- [22] B. Kermani, J.C. Gonzales, G.L. Turconi, T.E. Perez, C. Morales, In-field corrosion performance of 3% Cr steels in sweet and sour downhole production and water injection, in: CORROSION 2004, 2004.
- [23] B. Metz, O. Davidson, H. De Coninck, M. Loos, L. Meyer, IPCC special report on carbon dioxide capture and storage, in, United States of America by Cambridge University Press, New York, 2005.
- [24] Y.-S. Choi, D. Young, S. Nešić, L.G.S. Gray, Wellbore integrity and corrosion of carbon steel in CO₂ geologic storage environments: A literature review, *International Journal of Greenhouse Gas Control*, 16 (2013) S70-S77.
- [25] National Energy Board, Regulating pipeline abandonment, 2011.
- [26] Alberta Innovates Technology Futures, Cleaning pipeline for abandonment, Final report, 2015.
- [27] M.B. Kermani, A. Morshed, Carbon dioxide corrosion in oil and gas production - A compendium, *Corrosion*, 59 (2003) 659-683.
- [28] E. Eriksrud, T. Sontvedt, Effect of flow on CO₂ corrosion rates in real and synthetic formation waters, Houston, TX: NACE, 1984.
- [29] M. Nordsveen, S. Nešić, R. Nyborg, A. Stangeland, A mechanistic model for carbon dioxide corrosion of mild steel in the presence of protective iron carbonate films—Part 1: Theory and verification, *Corrosion*, 59 (2003) 443-456.
- [30] G.A. Zhang, Y.F. Cheng, Corrosion of X65 steel in CO₂-saturated oilfield formation water in the absence and presence of acetic acid, *Corrosion Science*, 51 (2009) 1589-1595.
- [31] K. George, Electrochemical investigation of carbon dioxide corrosion of mild steel in the presence of acetic acid, in, Ohio University, 2003.
- [32] K.-L. Lee, S. Nestic, EIS Investigation in the electrochemistry of CO₂/H₂S corrosion, in: CORROSION 04, NACE International, New Orleans, Louisiana, 2004.
- [33] M.H. Nazari, S.R. Allahkaram, The effect of acetic acid on the CO₂ corrosion of grade X70 steel, *Materials & Design*, 31 (2010) 4290-4295.
- [34] Q. Li, Y.F. Cheng, Nonuniform corrosion of steel pipe with a fluid flow containing carbon dioxide, *Materials Performance*, 55 (2016) 58-62.
- [35] G.A. Zhang, L. Zeng, H.L. Huang, X.P. Guo, A study of flow accelerated corrosion at elbow of carbon steel pipeline by array electrode and computational fluid dynamics simulation, *Corrosion Science*, 77 (2013) 334-341.

- [36] R.C. Barik, J.A. Wharton, R.J.K. Wood, K.R. Stokes, Electro-mechanical interactions during erosion–corrosion, *Wear*, 267 (2009) 1900-1908.
- [37] Y. Yang, Y.F. Cheng, Parametric effects on the erosion–corrosion rate and mechanism of carbon steel pipes in oil sands slurry, *Wear*, 276-277 (2012) 141-148.
- [38] G.A. Zhang, Y.F. Cheng, Electrochemical characterization and computational fluid dynamics simulation of flow-accelerated corrosion of X65 steel in a CO₂-saturated oilfield formation water, *Corrosion Science*, 52 (2010) 2716-2724.
- [39] G.A. Zhang, Y.F. Cheng, Electrochemical corrosion of X65 pipe steel in oil/water emulsion, *Corrosion Science*, 51 (2009) 901-907.
- [40] H.Q. Becerra, C. Retamoso, D.D. Macdonald, The corrosion of carbon steel in oil-in-water emulsions under controlled hydrodynamic conditions, *Corrosion Science*, 42 (2000) 561-575.
- [41] J.R. Vera, S. Hernandez, Oil characteristics, water/oil wetting and flow influence on the metal loss corrosion-Part I: Effect of oil and flow on CO₂/H₂S corrosion, in: *CORROSION 2006*, NACE International, 2006.
- [42] Y. Zhang, X. Pang, S. Qu, X. Li, K. Gao, Discussion of the CO₂ corrosion mechanism between low partial pressure and supercritical condition, *Corrosion Science*, 59 (2012) 186-197.
- [43] F.M. Song, A comprehensive model for predicting CO₂ corrosion rate in oil and gas production and transportation systems, *Electrochimica Acta*, 55 (2010) 689-700.
- [44] J. Han, J.W. Carey, J. Zhang, A coupled electrochemical–geochemical model of corrosion for mild steel in high-pressure CO₂–saline environments, *International Journal of Greenhouse Gas Control*, 5 (2011) 777-787.
- [45] G. Lin, M. Zheng, Z. Bai, X. Zhao, Effect of temperature and pressure on the morphology of carbon dioxide corrosion scales, *Corrosion*, 62 (2006) 501-507.
- [46] S.L. Wu, Z.D. Cui, G.X. Zhao, M.L. Yan, S.L. Zhu, X.J. Yang, EIS study of the surface film on the surface of carbon steel from supercritical carbon dioxide corrosion, *Applied Surface Science*, 228 (2004) 17-25.
- [47] Q. Liu, J. Whittaker, R. Allende-Garcia, A. McIntyre, J. Magyar, K. Tamminga, Corrosion management and cleaning of SAGD produced gas/H₂S scavenger contactor, in: *CORROSION 2014*, NACE International, 2014.
- [48] T. Tanupabrunsun, Thermodynamics and kinetics of carbon dioxide corrosion of mild steel at elevated temperatures, in, Ohio University, 2013.
- [49] Z. Duan, R. Sun, C. Zhu, I.M. Chou, An improved model for the calculation of CO₂ solubility in aqueous solutions containing Na⁺, K⁺, Ca²⁺, Mg²⁺, Cl⁻, and SO₄²⁻, *Marine Chemistry*, 98 (2006) 131-139.
- [50] I.S. Cole, D. Marney, The science of pipe corrosion: A review of the literature on the corrosion of ferrous metals in soils, *Corrosion Science*, 56 (2012) 5-16.
- [51] L.J.C. López, E. Arce, J. Torres, J. Vazquez-Arenas, J.M. Hallen, R. Cabrera-Sierra, Corrosion process of API X52 carbon steel immersed in an aqueous solution simulating a clay soil, *Corrosion*, 67 (2011) 116001-1160010.
- [52] F.M. Song, D.A. Jones, D.W. Kirk, Predicting corrosion and current flow within a disc crevice on coated steels, *Corrosion*, 61 (2005) 145-154.

- [53] S. Wang, D. Liu, N. Du, Q. Zhao, S. Liu, J. Xiao, Relationship between dissolved oxygen and corrosion characterization of X80 Steel in acidic soil simulated solution, *International Journal of Electrochemical Science*, 10 (2015) 4393-4404.
- [54] H. Tamura, The role of rusts in corrosion and corrosion protection of iron and steel, *Corrosion Science*, 50 (2008) 1872-1883.
- [55] T.R. Jack, K. Krist, B. Erno, R.R. Fessler, Generation of near neutral pH and high pH SCC environments on buried pipelines, in: *CORROSION 2000*, NACE International, 2000.
- [56] S.K. Gupta, B.K. Gupta, The critical soil moisture content in the underground corrosion of mild steel, *Corrosion Science*, 19 (1979) 171-178.
- [57] R.E. Ricker, Analysis of pipeline steel corrosion data from NBS (NIST) studies conducted between 1922–1940 and relevance to pipeline management, *Journal of research of the National Institute of Standards and Technology*, 115 (2010) 20.
- [58] A.S. Ikechukwu, N.H. Ugochukwu, R.A. Ejimofor, E. Obioma, Correlation between soil properties and external corrosion growth rate of carbon Steel, (2014).
- [59] A. Neville, Chloride attack of reinforced concrete: an overview, *Materials and Structures*, 28 (1995) 63-70.
- [60] L. Cáceres, T. Vargas, L. Herrera, Determination of electrochemical parameters and corrosion rate for carbon steel in un-buffered sodium chloride solutions using a superposition model, *Corrosion Science*, 49 (2007) 3168-3184.
- [61] J.R. Rossum, Prediction of pitting rates in ferrous metals from soil parameters, *Journal (American Water Works Association)*, 61 (1969) 305-310.
- [62] C. De Waard, D.E. Milliams, Carbonic acid corrosion of steel, *Corrosion*, 31 (1975) 177-181.
- [63] R. Nyborg, CO₂ corrosion models for oil and gas production systems, in: *CORROSION 2010*, 2010.
- [64] S.E. Hernandez, Z. Zhang, J. Vera, R.C. Woollam, Development and implementation of a new mechanistic CO₂ corrosion model for oil and gas production, in: *CORROSION 2010*, NACE International, 2010.
- [65] S. Norway, M506: CO₂ corrosion rate calculation model, in: *Norway: Norwegian Technological Standards Institute*, 2005, pp. 18.
- [66] S. Kanwar, W. Jepson, A model to predict sweet corrosion of multiphase flow in horizontal pipelines, in: *NACE International, Houston, TX (United States)*, 1994.
- [67] C. de Waard, U. Lotz, D.E. Milliams, Predictive model for CO₂ corrosion engineering in wet natural gas pipelines, *Corrosion*, 47 (1991) 976-985.
- [68] L. Smith, C. de Waard, Corrosion prediction and materials selection for oil and gas producing environments, in: *CORROSION 2005*, NACE International, Houston, Texas, USA, 2005.
- [69] C. De Waard, L. Smith, P. Bartlett, H. Cunningham, Modelling corrosion rates in oil production tubing, in: *Eurocorr 2001*, Riva del Garda, Italy, 2001.
- [70] C. De Waard, U. Lotz, Prediction of CO₂ corrosion of carbon steel, in: *CORROSION 1993*, NACE, 1993.
- [71] C. De Waard, L. Smith, B. Craig, The influence of crude oil on well tubing corrosion rates, in: *CORROSION 2003*, 2003.

- [72] C. De Waard, U. Lotz, A. Dugstad, Influence of liquid flow velocity on CO₂ corrosion: A semi-empirical model, in: Corrosion 95, NACE, 1995.
- [73] S. Nestic, H. Li, J. Huang, D. Sormaz, A free open source mechanistic model for prediction of mild steel corrosion, in: Proceedings of the 17th International Corrosion Congress, 2008.
- [74] L.G. Gray, B.G. Anderson, M.J. Danysh, P. Tremaine, Mechanism of carbon steel corrosion in brines containing dissolved carbon dioxide at pH 4, in: CORROSION 89, 1989.
- [75] L.G. Gray, B.G. Anderson, M.J. Danysh, P.R. Tremaine, Effect of pH and temperature on the mechanism of carbon steel corrosion by aqueous carbon dioxide, in: CORROSION 90, 1990.
- [76] J. Newman, K.E. Thomas-Alyea, Electrochemical systems, John Wiley & Sons, 2004.
- [77] S. Nešić, K.L.J. Lee, A mechanistic model for carbon dioxide corrosion of mild steel in the presence of protective iron carbonate films—Part 3: Film growth model, Corrosion, 59 (2003) 616-628.
- [78] S. Nešić, M. Nordsveen, R. Nyborg, A. Stangeland, A mechanistic model for carbon dioxide corrosion of mild steel in the presence of protective iron carbonate films—Part 2: A numerical experiment, Corrosion, 59 (2003) 489-497.
- [79] S. Nestic, R. Nyborg, A. Stangeland, M. Nordsveen, Mechanistic modeling for CO₂ corrosion with protective iron carbonate films, in: CORROSION 2001, 2001.
- [80] Z. Zhang, D. Hinkson, M. Singer, H. Wang, S. Nešić, A mechanistic model of top-of-the-line corrosion, Corrosion, 63 (2007) 1051-1062.
- [81] J.F. Sánchez, F. Alhama, J.A. Moreno, An efficient and reliable model based on network method to simulate CO₂ corrosion with protective iron carbonate films, Computers & Chemical Engineering, 39 (2012) 57-64.
- [82] M. Sundaram, V. Raman, M.S. High, D.A. Tree, J. Wagner, Deterministic modeling of corrosion in downhole environments, in: CORROSION 96, 1996.
- [83] F.M. Song, D.W. Kirk, J.W. Graydon, D.E. Cormack, Predicting carbon dioxide corrosion of bare steel under an aqueous boundary layer, Corrosion, 60 (2004) 736-748.
- [84] F.M. Song, N. Sridhar, Modeling pipeline crevice corrosion under a disbanded coating with or without cathodic protection under transient and steady state conditions, Corrosion Science, 50 (2008) 70-83.
- [85] S. Nestic, S. Wang, J. Cai, Y. Xiao, Integrated CO₂ corrosion - Multiphase flow model, in: SPE International Symposium on Oilfield Corrosion, Society of Petroleum Engineers, Aberdeen, United Kingdom, 2004.
- [86] L. Xu, F. Cheng, Finite element based modeling of internal CO₂ corrosion of pipelines, in: CORROSION 2015, NACE International, Dallas, TX, USA, 2015.
- [87] Y. Xiang, Z. Wang, M. Xu, Z. Li, W. Ni, A mechanistic model for pipeline steel corrosion in supercritical CO₂-SO₂-O₂-H₂O environments, The Journal of Supercritical Fluids, 82 (2013) 1-12.
- [88] R. Case, S. Mahajanam, J. Dunn, M. Joosten, M. Achour, H. Marchebois, M. Bonis, High temperature corrosion studies in simulated SAGD produced fluids, Corrosion, 71 (2015) 536-545.

- [89] J.C. Velázquez, F. Caleyó, A. Valor, J.M. Hallen, Predictive model for pitting corrosion in buried oil and gas pipelines, *Corrosion*, 65 (2009) 332-342.
- [90] J.L. Alamilla, M.A. Espinosa-Medina, E. Sosa, Modelling steel corrosion damage in soil environment, *Corrosion Science*, 51 (2009) 2628-2638.
- [91] F.M. Song, D.W. Kirk, J.W. Graydon, D.E. Cormack, Steel corrosion under a disbonded coating with a holiday—Part 1: The model and validation, *Corrosion*, 58 (2002) 1015-1024.
- [92] F.M. Song, N. Sridhar, A Two-dimensional model for steel corrosion under a disbonded coating due to oxygen with or without cathodic protection—Part 1: Full numerical solution, *Corrosion*, 62 (2006) 676-686.
- [93] M. Henriquez, N. Pébère, N. Ochoa, A. Vilorio, Electrochemical investigation of the corrosion behavior of API 5L-X65 carbon steel in carbon dioxide medium, *Corrosion*, 69 (2013) 1171-1179.
- [94] F. De Moraes, J.R. Shadley, J. Chen, E.F. Rybicki, Characterization of CO₂ corrosion product scales related to environmental conditions, in: *CORROSION 2000*, NACE International, Orlando, Florida, 2000.
- [95] G.A. Zhang, Y.F. Cheng, On the fundamentals of electrochemical corrosion of X65 steel in CO₂-containing formation water in the presence of acetic acid in petroleum production, *Corrosion Science*, 51 (2009) 87-94.
- [96] K.D. Efird, E.J. Wright, J.A. Boros, T.G. Hailey, Correlation of steel corrosion in pipe flow with jet impingement and rotating cylinder tests, *Corrosion*, 49 (1993) 992-1003.
- [97] S. Nestic, J. Postlethwaite, S. Olsen, An electrochemical model for prediction of corrosion of mild steel in aqueous carbon dioxide solutions, *Corrosion*, 52 (1996) 280-294.
- [98] A.C. Yunus, J.M. Cimbala, *Fluid mechanics: fundamentals and applications*, International Edition, McGraw Hill Publication, (2006) 185-201.
- [99] H.-j. SUN, L. LIU, Y. LI, Corrosion behavior of a high strength low alloy steel under hydrostatic pressure in deep ocean, *Journal of Electrochemistry*, V19 (2013) 418-424.
- [100] A.M. Beccaria, P. Fiordiponti, G. Mattogno, The effect of hydrostatic pressure on the corrosion of nickel in slightly alkaline solutions containing Cl⁻ ions, *Corrosion Science*, 29 (1989) 403-413.
- [101] A.M. Beccaria, G. Poggi, Influence of hydrostatic pressure on pitting of aluminium in sea water, *British Corrosion Journal*, 20 (1985) 183-186.
- [102] V. Srinivasan, Evaluation of flow coupled CO₂ corrosion using CFD: Kinetics & hydrodynamics, in: *CORROSION 2015*, NACE International, 2015.
- [103] W.P. Jepson, S. Bhongale, M. Gopal, Predictive model for sweet corrosion in horizontal multiphase slug flow, in: *Corrosion 96*, 1996.
- [104] Talk about SAGD, in: http://www.energy.alberta.ca/OilSands/pdfs/FS_SAGD.pdf, 2013.
- [105] N. Spycher, K. Pruess, A phase-partitioning model for CO₂-brine mixtures at elevated temperatures and pressures: application to CO₂-enhanced geothermal systems, *Transport in Porous Media*, 82 (2009) 173-196.

- [106] N. Spycher, K. Pruess, J. Ennis-King, CO₂-H₂O mixtures in the geological sequestration of CO₂. I. Assessment and calculation of mutual solubilities from 12 to 100°C and up to 600 bar, *Geochimica et Cosmochimica Acta*, 67 (2003) 3015-3031.
- [107] A.Z. Panagiotopoulos, R.C. Reid, New mixing rule for cubic equations of state for highly polar, asymmetric systems, 300 (1986) 571-582.
- [108] O. Redlich, J.N.S. Kwong, On the thermodynamics of solutions. V. An equation of state. Fugacities of gaseous solutions, *Chemical Reviews*, 44 (1949) 233-244.
- [109] W. Sun, S. Nešić, R.C. Woollam, The effect of temperature and ionic strength on iron carbonate (FeCO₃) solubility limit, *Corrosion Science*, 51 (2009) 1273-1276.
- [110] S. Hernandez, S. Nešić, G. Weckman, V. Ghai, Use of artificial neural networks for predicting crude oil effect on carbon dioxide corrosion of carbon steels, *Corrosion*, 62 (2006) 467-482.
- [111] B. Mishra, S. Al-Hassan, D. Olson, M. Salama, Development of a predictive model for activation-controlled corrosion of steel in solutions containing carbon dioxide, *Corrosion*, 53 (1997) 852-859.
- [112] R. Gupta, S. Singh, V. Sehadri, Prediction of uneven wear in a slurry pipeline on the basis of measurements in a pot tester, *Wear*, 184 (1995) 169-178.
- [113] NIST, Thermophysical properties of fluid systems, in: NIST chemistry webbook, NIST standard reference database number 69, 2015.
- [114] T. Tanupabrungsun, D. Young, B. Brown, S. Nešić, Construction and verification of pourbaix diagrams for CO₂ corrosion of mild steel valid up to 250 °C, in: *CORROSION 2012*, 2012.
- [115] M. Bridle, Treatment of SAGD produced waters without lime softening, in: *SPE International Thermal Operations and Heavy Oil Symposium*, Society of Petroleum Engineers, Calgary, Alberta, Canada, 2005.
- [116] M.M. Salama, An alternative to API 14E erosional velocity limits for sand laden fluids, in: *Offshore Technology Conference*, Offshore Technology Conference, Houston, Texas, 1998.
- [117] <http://econintersect.com/b2evolution/blog1.php/2013/07/16/epa-s-abandoned-wyoming-fracking-study-one-retreat-of-many>.
- [118] R.N. Tuttle, Corrosion in oil and gas production, *Journal of Petroleum Technology*, 39 (1987) 756-762.
- [119] S. Talabani, B. Atlas, M.B. Al-Khatiri, M.R. Islam, An alternate approach to downhole corrosion mitigation, *Journal of Petroleum Science and Engineering*, 26 (2000) 41-48.
- [120] J. Heathman, Critical application cementing—Redefining the issues, in: *SPE Distinguished Lecture*, Houston, 2008.
- [121] D.A. Palmer, R. Van Eldik, The chemistry of metal carbonate and carbon dioxide complexes, *Chemical Reviews*, 83 (1983) 651-731.
- [122] Z. Duan, D. Li, Coupled phase and aqueous species equilibrium of the H₂O–CO₂–NaCl–CaCO₃ system from 0 to 250°C, 1 to 1000bar with NaCl concentrations up to saturation of halite, *Geochimica et Cosmochimica Acta*, 72 (2008) 5128-5145.
- [123] W.L. Marshall, E.U. Franck, Ion product of water substance, 0–1000 °C, 1–10,000 bars new international formulation and its background, *Journal of Physical and Chemical Reference Data*, 10 (1981) 295.

- [124] J.W. Johnson, E.H. Oelkers, H.C. Helgeson, SUPCRT92: A software package for calculating the standard molal thermodynamic properties of minerals, gases, aqueous species, and reactions from 1 to 5000 bar and 0 to 1000 °C, *Computers & Geosciences*, 18 (1992) 899-947.
- [125] Y.-S. Choi, S. Nešić, Determining the corrosive potential of CO₂ transport pipeline in high pCO₂-water environments, *International Journal of Greenhouse Gas Control*, 5 (2011) 788-797.
- [126] K.S. Pitzer, *Activity coefficients in electrolyte solutions* (2nd edn.), CRC Press, Boca Raton, 1991.
- [127] K.S. Pitzer, J.C. Peiper, R.H. Busey, Thermodynamic properties of aqueous sodium chloride solutions, *Journal of Physical and Chemical Reference Data*, 13 (1984) 1.
- [128] D.A. Polya, E.M. Woolley, J.M. Simonson, R.E. Mesmer, The enthalpy of dilution and thermodynamics of Na₂CO_{3(aq)} and NaHCO_{3(aq)} from T= 298 K to T= 523.15 K and pressure of 40 MPa, *The Journal of Chemical Thermodynamics*, 33 (2001) 205-243.
- [129] R.T. Pabalan, K.S. Pitzer, Thermodynamics of NaOH_(aq) in hydrothermal solutions, *Geochimica et Cosmochimica Acta*, 51 (1987) 829-837.
- [130] N. Møller, The prediction of mineral solubilities in natural waters: A chemical equilibrium model for the Na-Ca-Cl-SO₄-H₂O system, to high temperature and concentration, *Geochimica et Cosmochimica Acta*, 52 (1988) 821-837.
- [131] H.F. Holmes, R.H. Busey, J.M. Simonson, R.E. Mesmer, D.G. Archer, R.H. Wood, The enthalpy of dilution of HCl_(aq) to 648 K and 40 MPa thermodynamic properties, *The Journal of Chemical Thermodynamics*, 19 (1987) 863-890.
- [132] F.J. Millero, D. Pierrot, A chemical equilibrium model for natural waters, *Aquatic Geochemistry*, 4 (1998) 153-199.
- [133] C. Christov, N. Møller, A chemical equilibrium model of solution behavior and solubility in the H-Na-K-Ca-OH-Cl-HSO₄-SO₄-H₂O system to high concentration and temperature, *Geochimica et Cosmochimica Acta*, 68 (2004) 3717-3739.
- [134] J. Li, Z. Duan, A thermodynamic model for the prediction of phase equilibria and speciation in the H₂O-CO₂-NaCl-CaCO₃-CaSO₄ system from 0 to 250°C, 1 to 1000 bar with NaCl concentrations up to halite saturation, *Geochimica et Cosmochimica Acta*, 75 (2011) 4351-4376.
- [135] D. Li, Z. Duan, The speciation equilibrium coupling with phase equilibrium in the H₂O-CO₂-NaCl system from 0 to 250 °C, from 0 to 1000 bar, and from 0 to 5 molality of NaCl, *Chemical Geology*, 244 (2007) 730-751.
- [136] S. He, J.W. Morse, The carbonic acid system and calcite solubility in aqueous Na-K-Ca-Mg-Cl-SO₄ solutions from 0 to 90°C, *Geochimica et Cosmochimica Acta*, 57 (1993) 3533-3554.
- [137] C. Christov, N. Møller, Chemical equilibrium model of solution behavior and solubility in the H-Na-K-OH-Cl-HSO₄-SO₄-H₂O system to high concentration and temperature, *Geochimica et Cosmochimica Acta*, 68 (2004) 1309-1331.
- [138] J.C. Peiper, K.S. Pitzer, Thermodynamics of aqueous carbonate solutions including mixtures of sodium carbonate, bicarbonate, and chloride, *The Journal of Chemical Thermodynamics*, 14 (1982) 613-638.
- [139] V. Thurmond, F.J. Millero, Ionization of carbonic acid in sodium chloride solutions at 25 °C, *Journal of Solution Chemistry*, 11 (1982) 447-456.

- [140] C.E. Harvie, N. Moller, J. Weare, The prediction of mineral solubilities in natural waters: The Na-K-Mg-Ca-H-Cl-SO₄-OH-HCO₃-CO₃-CO₂-H₂O system to high ionic strengths at 25 °C, *Geochim. Cosmochim. Acta*, 48 (1984) 723-751.
- [141] D. Pierrot, F.J. Millero, L.N. Roy, R.N. Roy, A. Doneski, J. Niederschmidt, The activity coefficients of HCl in HCl-Na₂SO₄ solutions from 0 to 50 °C and ionic strengths up to 6 molal, *Journal of Solution Chemistry*, 26 (1997) 31-45.
- [142] C.E. Harvie, J.H. Weare, The prediction of mineral solubilities in natural waters-the Na-K-Mg-Ca-Cl-SO₄-H₂O system from zero to high concentration at 25 °C.pdf, *Geochimica et Cosmochimica Acta*, 44 (1980) 981-997.
- [143] A.R. Felmy, J.H. Weare, The prediction of borate mineral equilibria in natural waters: Application to Searles Lake, California, *Geochimica et Cosmochimica Acta*, 50 (1986) 2771-2783.
- [144] Y. Zheng, J. Ning, B. Brown, S. Nešić, Electrochemical model of mild steel corrosion in a mixed H₂S/CO₂ aqueous environment in the absence of protective corrosion product layers, *Corrosion*, 71 (2015) 316-325.
- [145] Y. Zheng, B. Brown, S. Nešić, Electrochemical study and modeling of H₂S corrosion of mild steel, *Corrosion*, 70 (2014) 351-365.
- [146] R. Perry, D. Green, Perry's chemical engineers' handbook, 6th (50th anniversary) edition, in, McGraw Hill, 1984.
- [147] J. Kvarekval, A kinetic model for calculating concentration profiles and fluxes of CO₂-related species across the nernst diffusion layer, in: *CORROSION 97*, 1997.
- [148] F. Song, A model developed to predict the internal corrosion rates of wet and dry gas pipelines, in: *CORROSION 2011*, 2011.
- [149] J.L. Crolet, M.R. Bonis, pH measurements in aqueous CO₂ solutions under high pressure and temperature, *Corrosion*, 39 (1983) 39-46.
- [150] B. Meyssami, M.O. Balaban, A.A. Teixeira, Prediction of pH in model systems pressurized with carbon dioxide, *Biotechnology Progress*, 8 (1992) 149-154.
- [151] G. Hinds, P. Cooling, A. Wain, S. Zhou, A. Turnbull, Technical note: measurements of pH in concentrated brines, *Corrosion*, 65 (2009) 635-702.
- [152] C. Plennevaux, N. Ferrando, J. Kittel, M. Frégonèse, B. Normand, T. Cassagne, F. Ropital, M. Bonis, pH prediction in concentrated aqueous solutions under high pressure of acid gases and high temperature, *Corrosion Science*, 73 (2013) 143-149.
- [153] Z.D. Cui, S.L. Wu, S.L. Zhu, X.J. Yang, Study on corrosion properties of pipelines in simulated produced water saturated with supercritical CO₂, *Applied Surface Science*, 252 (2006) 2368-2374.
- [154] Y.-S. Choi, F. Farelàs, S. Nešić, A.A.O. Magalhães, C. de Azevedo Andrade, Corrosion behavior of deep water oil production tubing material under supercritical CO₂ environment: Part 1—Effect of pressure and temperature, *Corrosion*, 70 (2014) 38-47.
- [155] S. Hassani, T.N. Vu, N.R. Rosli, S.N. Esmaeely, Y.-S. Choi, D. Young, S. Nestic, Wellbore integrity and corrosion of low alloy and stainless steels in high pressure CO₂ geologic storage environments: An experimental study, *International Journal of Greenhouse Gas Control*, 23 (2014) 30-43.
- [156] Y. Hua, R. Barker, A. Neville, Comparison of corrosion behaviour for X65 carbon steel in supercritical CO₂-saturated water and water-saturated/unsaturated supercritical CO₂, *The Journal of Supercritical Fluids*, 97 (2015) 224-237.

- [157] Y. Wang, H.Y. Yu, Y. Cheng, H.T. Shan, L.X. Zhang, D.B. Sun, Corrosion behaviors of X80 pipeline steel in different simulated alkaline soil solution, *Advanced Materials Research*, 189-193 (2011) 4261-4266.
- [158] ASTM G1-03, Standard practice for preparing, cleaning, and evaluating corrosion test specimens, in, ASTM International, West Conshohocken, 2011.
- [159] R.A. Antunes, I. Costa, D.L.A.d. Faria, Characterization of corrosion products formed on steels in the first months of atmospheric exposure, *Materials Research*, 6 (2003) 403-408.
- [160] A. Ismail, N. Adan, Effect of oxygen concentration on corrosion rate of carbon steel in seawater, *American Journal of Engineering Research*, 3 (2014) 64-67.
- [161] L. Cáceres, T. Vargas, M. Parra, Study of the variational patterns for corrosion kinetics of carbon steel as a function of dissolved oxygen and NaCl concentration, *Electrochimica Acta*, 54 (2009) 7435-7443.
- [162] H.E. Desouky, H.A. Aboeldahab, Effect of chloride concentration on the corrosion rate of maraging steel, *Open Journal of Physical Chemistry*, 04 (2014) 147-165.
- [163] Y. Li, J. Wu, D. Zhang, Y. Wang, B. Hou, The electrochemical reduction reaction of dissolved oxygen on Q235 carbon steel in alkaline solution containing chloride ions, *Journal of Solid State Electrochemistry*, 14 (2010) 1667-1673.
- [164] X.X. Zheng, Description of the corrosion rate of 16Mn pipeline steel in soil by using neural network, *Journal of Xi'an Shiyou University*, 19 (2004) 73-76.
- [165] F. Song, Predicting the chemistry and corrosion rates in a coating disbonded region with or without cathodic current penetrating in via the holiday and coating, in: *CORROSION 2011*, 2011.
- [166] F.M. Song, D.W. Kirk, J.W. Graydon, D.E. Cormack, Steel corrosion under a disbonded coating with a holiday—Part 2: Corrosion behavior, *Corrosion*, 59 (2003) 42-49.
- [167] F.M. Song, N. Sridhar, A two-dimensional model for steel corrosion under a disbonded coating due to oxygen with or without cathodic protection—Part 2: Model simplification for practical application, *Corrosion*, 62 (2006) 873-882.
- [168] X. Chen, F. Gao, Y. Wang, C. He, Transient numerical model for crevice corrosion of pipelines under disbonded coating with cathodic protection, *Materials & Design*, 89 (2016) 196-204.
- [169] Y.C. Chang, R. Woollam, M.E. Orazem, Mathematical models for under-deposit corrosion: I. Aerated media, *Journal of the Electrochemical Society*, 161 (2014) C321-C329.
- [170] I.M. Gadala, M. Abdel Wahab, A. Alfantazi, Numerical simulations of soil physicochemistry and aeration influences on the external corrosion and cathodic protection design of buried pipeline steels, *Materials & Design*, 97 (2016) 287-299.
- [171] Potentiodynamic, in: <https://www.corrosionpedia.com/definition/911/potentiodynamic>.
- [172] X.L. Zhang, Z.H. Jiang, Z.P. Yao, Y. Song, Z.D. Wu, Effects of scan rate on the potentiodynamic polarization curve obtained to determine the Tafel slopes and corrosion current density, *Corrosion Science*, 51 (2009) 581-587.

- [173] H.J. Flitt, D.P. Schweinsberg, A guide to polarisation curve interpretation: deconstruction of experimental curves typical of the Fe/H₂O/H⁺/O₂ corrosion system, *Corrosion Science*, 47 (2005) 2125-2156.
- [174] C. Chunan, Estimation of electrochemical kinetic parameters of corrosion processes by weak polarization curve fitting, *Journal of Chinese Society for Corrosion and protection*, 5 (1985) 155-164.
- [175] F. Mansfeld, Tafel slopes and corrosion rates obtained in the pre-Tafel region of polarization curves, *Corrosion Science*, 47 (2005) 3178-3186.
- [176] A.A. El-Feki, G.W. Walter, Corrosion rate measurements under conditions of mixed charge transfer plus diffusion control including the cathodic metal ion deposition partial reaction, *Corrosion Science*, 42 (2000) 1055-1070.
- [177] H.J. Flitt, D.P. Schweinsberg, Evaluation of corrosion rate from polarisation curves not exhibiting a Tafel region, *Corrosion Science*, 47 (2005) 3034-3052.
- [178] E. McCafferty, *Introduction to corrosion science*, Springer Science & Business Media, 2010.
- [179] C. Wagner, W. Traud, On the interpretation of corrosion processes by superimposing of electro chemical potential and the potential formation of mixed electrodes, *Electrochem*, 44 (1938) 391-402.
- [180] M. Alfaro, Modeling of polarization curves not exhibiting a Tafel region using Excel spreadsheets, *Alexandria Engineering Journal*, 53 (2014) 977-983.
- [181] Excel Solver - Algorithms and methods used, in: <http://www.solver.com/excel-solver-algorithms-and-methods-used>.
- [182] M.L. Johnson, Why, when, and how biochemists should use least squares, *Analytical Biochemistry*, 206 (1992) 215-225.
- [183] L. Li, C.H. Benson, E.M. Lawson, Modeling porosity reductions caused by mineral fouling in continuous-wall permeable reactive barriers, *J Contam Hydrol*, 83 (2006) 89-121.
- [184] E.J.F. Dickinson, J.G. Limon-Petersen, R.G. Compton, The electroneutrality approximation in electrochemistry, *Journal of Solid State Electrochemistry*, 15 (2011) 1335-1345.
- [185] K.U. Mayer, D.W. Blowes, E.O. Frind, Reactive transport modeling of an in situ reactive barrier for the treatment of hexavalent chromium and trichloroethylene in groundwater, *Water Resources Research*, 37 (2001) 3091-3103.
- [186] R. Parsons, *Hand book of electrochemical constants*, Butterworths Scientific Publications, London, 1959.
- [187] ASTM G59-97, Standard test method for conducting potentiodynamic polarization resistance measurements, 2014.
- [188] W. Wagner, H.-J. Kretzschmar, *International steam tables-properties of water and steam based on the industrial formulation IAPWS-IF97: Tables, Algorithms, Diagrams, and CD-ROM Electronic Steam Tables-All of the equations of IAPWS-IF97 including a complete set of supplementary backward equations for fast calculations of heat cycles, boilers, and steam turbines*, Springer, 2007.
- [189] D.J. Bradley, K.S. Pitzer, Thermodynamics of electrolytes. 12. Dielectric properties of water and Debye-Hueckel parameters to 350 degree C and 1 kbar, *The Journal of Physical Chemistry*, 83 (1979) 1599-1603.

[190] D. Tromans, Modeling oxygen solubility in water and electrolyte solutions, *Industrial & Engineering Chemistry Research*, 39 (2000) 805-812.

Appendix A: Equilibrium constants for chemical reactions

The equilibrium constant K_{hy} for CO₂ hydration and forward reaction constant $K_{f,hy}$ are as follows [121]:

$$K_{hy} = 2.58 \times 10^{-3} \quad (\text{A-1})$$

$$K_{f,hy} = 10^{\left(\frac{329.85 - 110.54 \times \log T - \frac{17.2654}{T}}{T}\right)} \text{ s}^{-1} \quad (\text{A-2})$$

The backward reaction constant $K_{b,hy}$ can be calculate by $K_{f,hy} / K_{hy}$.

Equilibrium constant K_{ca} for dissociation of bicarbonate is not obtained directly, we have the equilibrium constant K_{hc} [122] which describes the combination of Eq. (2-2) and (2-3), K_{ca} should be further calculated with Eq. (A-4)

$$\begin{aligned} \ln K_{hc} = & 233.5159304 - 11974.38348T^{-1} - 36.50633536 \ln T \\ & + (-45.08004597T^{-1} + 2131.318848T^{-2} + 6.71425629T^{-1} \ln T)(P - P_s) \\ & + (0.008393915212T^{-1} - 0.4015441404T^{-2} - 0.0012401873T^{-1})(P - P_s)^2 \end{aligned} \quad (\text{A-3})$$

$$K_{ca} = K_{hc} / K_{hy} \quad (\text{A-4})$$

Equilibrium constant K_{bi} of bicarbonate dissociation is [122]:

$$\begin{aligned} \ln K_{bi} = & -151.1815202 - 0.088695577T - 1362.259146T^{-1} + 27.79798156 \ln T \\ & - (29.51448102T^{-1} + 1389.015354T^{-2} + 4.419625804T^{-1} \ln T)(P - P_s) \\ & + (0.003219993525T^{-1} - 0.164447126T^{-2} - 0.000473667295T^{-1})(P - P_s)^2 \end{aligned}$$

(A-5)

The equilibrium constant K_{wa} for dissociation of water [123]:

$$\log K_{wa} = -4.098 - 3245.2T^{-1} + 2.2362 \times 10^5 T^{-2} - 3.984 \times 10^7 T^{-3} \\ + (13.957 - 1262.3T^{-1} + 8.5641 \times 10^5 T^{-2}) \log \rho_{H_2O}$$
(A-6)

The equilibrium constants K_{spFeCO_3} for iron carbonate precipitation [109]:

$$K_{spFeCO_3} = 10^{-(59.3498 - 0.041377T - 2.1963/T + 24.5724 \log T + 2.518 I^{0.5} - 0.657 I)}$$
(A-7)

Appendix B: Physical properties of water

Saturation pressure of water

When temperature is above 100 °C, the IAPWS-IF97 [188] functions to calculate saturation pressures of water have the following form:

$$P_s = \left[\frac{2C}{-B + (B^2 - 4AC)^{0.5}} \right]^4 \quad (\text{B-1})$$

$$A = \mathcal{G}^2 + n_1 \mathcal{G} + n_2 \quad (\text{B-2})$$

$$B = n_3 \mathcal{G}^2 + n_4 \mathcal{G} + n_5 \quad (\text{B-3})$$

$$C = n_6 \mathcal{G}^2 + n_7 \mathcal{G} + n_8 \quad (\text{B-4})$$

$$\mathcal{G} = T + n_9 / (T - n_{10}) \quad (\text{B-5})$$

where P_s is saturation pressure of water in bar, T is temperature in K. The parameters, n_1 – n_{10} , are listed in Table B1.

Table B1 Parameters for Eqs. (B-2) ~ (B-5)

n_1	0.11670521452767e+04
n_2	– 0.72421316703206e+06
n_3	– 0.17073846940092e+02
n_4	0.12020824702470e+05
n_5	– 0.32325550322333e+07
n_6	0.14915108613530e+02
n_7	– 0.48232657361591e+04
n_8	0.40511340542057e+06
n_9	– 0.23855557567849e+00
n_{10}	0.65017534844798e+03

Density of water

According to IAPWS-IF97 [188], to calculate the density of water, the specific volume of water, ν (m^3/kg), which has the following form should be calculated:

$$\nu = \pi \gamma_{\pi} \frac{RT}{P} \quad (\text{B-6})$$

$$\gamma_{\pi} = \sum_{i=1}^{34} -n_i I_i (7.1 - \pi)^{I_i - 1} (\tau - 1.222)^{J_i} \quad (\text{B-7})$$

where $\pi = P/P^*$ and $\tau = T^*/T$ with $P^* = 16.53$ MPa and $T^* = 1386$ K; $R = 0.461526$ kJ $\text{kg}^{-1} \text{K}^{-1}$. The coefficients n_i and exponents I_i and J_i of Eq. (B-7) are listed in Table B2.

Table B2 Coefficients and exponents of Eq. (B-7) in its dimensionless form

i	I_i	J_i	n_i	i	I_i	J_i	n_i
1	0	-2	0.14632971213167	18	2	3	-0.44141845330846e-05
2	0	-1	-0.84548187169114	19	2	17	-0.72694996297594e-15
3	0	0	-0.37563603672040e01	20	3	-4	-0.31679644845054e-04
4	0	1	0.33855169168385e01	21	3	0	-0.28270797985312e-05
5	0	2	-0.95791963387872	22	3	6	-0.85205128120103e-09
6	0	3	0.15772038513228	23	4	-5	-0.85205128120103e-05
7	0	4	-0.16616417199501e-01	24	4	-2	-0.65171222895601e-06
8	0	5	0.81214629983568e-03	25	4	10	-0.14341729937924e-12
9	1	-9	0.28319080123804e-03	26	5	-8	-0.40516996860117e-06
10	1	-7	-0.60706301565874e-03	27	8	-11	-0.12734301741641e-08
11	1	-1	-0.18990068218419e-01	28	8	-6	-0.17424871230634e-09
12	1	0	-0.32529748770505e-01	29	21	-29	-0.68762131295531e-18
13	1	1	-0.21841717175414e-01	30	23	-31	0.14478307828521e-19
14	1	3	-0.52838357969930e-04	31	29	-38	0.26335781662795e-22
15	2	-3	-0.47184321073267e-03	32	30	-39	-0.11947622640071e-22
16	2	0	-0.30001780793026e-03	33	31	-40	0.18228094581404e-23
17	2	1	0.47661393906987e-04	34	32	-41	-0.93537087292458e-25

Dielectric constant of water

The dielectric constant of water can be calculated by [189]

$$D = D_{1000} + C \ln((B + P)/(B + 1000)) \quad (\text{B-8})$$

where D_{1000} , C and B are temperature-dependent parameters, which are calculated as follows:

$$D_{1000} = U_1 \exp(U_2 T + U_3 T^2) \quad (\text{B-9})$$

$$C = U_4 + U_5 / (U_6 + T) \quad (\text{B-10})$$

$$B = U_7 + U_8 / T + U_9 T \quad (\text{B-11})$$

Table B3 Values of constants for the dielectric constant of water

U_1	3.4279e+02	U_6	- 1.8289e+02
U_2	- 5.0866e-03	U_7	- 8.0325e+03
U_3	9.4690e-07	U_8	4.2142e+06
U_4	- 2.0525	U_9	2.1417
U_5	3.1159e+03		

Appendix C: Oxygen solubility in electrolyte solutions

To calculate the dissolved oxygen in the soil solution, methodology from Tronmans [190] was used as:

$$C_{\text{aq}} = P_{\text{O}_2} k \phi_{\text{eff}} \quad (\text{C-1})$$

where C_{aq} is the concentration of O_2 in solution, mol/kg of water; k is a function of temperature T , which can be calculated as

$$k = \exp\left[\frac{(0.046T^2 + 203.35T \ln(T/298) - (299.378 + 0.092T) * (T - 298) - 20.591 \times 10^3)}{8.3144T}\right] \quad (\text{C-2})$$

and

$$\phi_{\text{eff}} = \phi_1 \left(\prod_2^n \phi_i \right) \quad (\text{C-3})$$

$$\phi_i = [1 + \kappa m_i^y]^{-h} \quad (\text{C-4})$$

which means there are n types of chemicals, such as NaCl , MgSO_4 , and so on. ϕ factors are arranged as $\phi_1 < \phi_2 < \dots < \phi_n$, κ , y and h are the constants, which can be found in Table C1.

Table C1 Values of coefficients in Eq. (C-4) for multiple chemicals

Chemicals	κ	y	h
NaNO ₃	0.314	1.084	0.883
Ca(NO ₃) ₂	0.021	0.947	21.04
Na ₂ CO ₃	0.34	1.1	3.13
NaCl	0.076	1.01	4.224
NaOH	0.102	1.0	4.309
CuSO ₄	2.232	1.116	0.223
KOH	0.102	1.0	4.309
KCl	0.407	1.116	0.842
Na ₂ SO ₄	0.63	0.912	1.44
K ₂ SO ₄	0.55	0.912	1.44
MgSO ₄	0.12	1.108	5.456
ZnSO ₄	0.233	1.01	2.656
MgCl ₂	0.18	0.985	2.711
CaCl ₂	0.18	0.985	2.711